Searches for new physics involving massive invisible particles

Jonathan Burr

Merton College
University of Oxford

A thesis submitted to the University of Oxford in fulfilment of the requirements for the degree of Doctor of Philosophy

Trinity 2018

Abstract

One of the most obvious problems with the Standard Model is the lack of any explanation for dark matter: a form of matter predicted from astrophysical observations but not compatible with any known subatomic particle. Many theories of new physics predict dark matter candidates which could be produced in 13 TeV collisions at the LHC. The primary experimental signature expected to accompany the production of a dark matter candidate is an imbalance in measurements of transverse momenta, referred to as $E_{\mathrm{T}}^{\mathrm{miss}}$. This thesis first covers the $E_{\mathrm{T}}^{\mathrm{miss}}$ trigger, a system responsible for selecting events with large $E_{\mathrm{T}}^{\mathrm{miss}}$ for later use in analyses and a vital component in many analyses. This signature suffers from very large backgrounds from QCD events with little true $E_{\mathrm{T}}^{\mathrm{miss}}$ and the high thresholds that would be required to control pass rates pose a risk to the efficiencies of analyses. A technique is presented that is shown to be able to reduce the rate by a factor of almost 4 while retaining high efficiencies in analysis signal regions. This thesis then documents a search for new physics using $36.1\,\mathrm{fb}^{-1}$ of data collected by the ATLAS detector. The search targets final states with no leptons and very high jet multiplicities, ranging from ≥ 7 to ≥ 11 in the tightest signal regions, which are characteristic of long decay chains which can be predicted by certain new physics models, especially supersymmetry. By using this signature the analysis is able to use a looser selection on $E_{\mathrm{T}}^{\mathrm{miss}}$, gaining sensitivity to areas of model spaces which may not be accessible to analyses reliant on the $E_{\mathrm{T}}^{\mathrm{miss}}$ trigger. No significant deviation from the Standard Model is observed and the analysis sets strong limits on the masses of supersymmetric particles, excluding gluino masses up to 1.8 TeV at the 95% confidence level.

Searches for new physics involving massive invisible particles

Jonathan Burr

Merton College

University of Oxford

A thesis submitted to the University of Oxford in fulfilment of the requirements for the degree of Doctor of Philosophy

Trinity 2018

Acknowledgements

First and foremost I must thank my supervisor, Alan Barr. Your encouragement, advice and infectious enthusiasm both during my undergraduate degree and DPhil were instrumental in leading me into the field and driving me onward.

I am also hugely grateful to the generations of students in the years above me whose help and support throughout my DPhil have been vital. Mireia Crispín Ortuzar made me feel welcome in the group right from the beginning and, especially in the early days, provided huge amounts of support that made the transition so much easier. Will Fawcett and Will Kalderon have been a wonderful to team to work with, mentoring me through many years of analysis and answering many stupid questions. Even since you have left Oxford you have been a much needed avenue to vent at shared irritations and more.

I have been privileged to work with some fantastic scientists. Teng Jian Khoo and Chris Young seem to always know the answer to any question you ask them. I am greatly indebted to Ben Carlson and Moritz Backes for all of their help and guidance.

While at CERN I was fortunate to have the company of the LTA group; lunches, coffee breaks, drinks and parties made the 15 months I spent there so enjoyable. Abby, Andy, Andy, Laurie, James, Tom, and Tom introduced me to the delight of watching First Dates as well as joint bike rides, holidays and more. With Shane, Ben, Laurie and Harry I shared the joy of (slowly) ascending mountains by bike and, with Abby, Andy, Anita and Tom, descending them increasingly rapidly on skis.

At Oxford Anita, Tom, Will, Lydia, Tim, Mike, Aaron and many others provided welcome distraction, friendship and pub trips. The madness of St. Mary's Road with Nicole, Claire, Eli, Jack, Mathieu and Flora was the perfect antidote to some of the most stressful times of my DPhil, I don't think I have ever come across such a diverse but happy group. James, Richard and Mariyan gave me the ideal environment for writing up and for much shared enjoyment.

Finally I must thank my family, my parents Anna and Alister and my sister Myriam. You have shaped me in so many ways.

There is no way to thank everyone that I must, there are many other people who should appear in this list and even for those who do I can only give the smallest pieces of how you have helped me. To you all, I am supremely grateful.

Preface

The work presented here in this thesis was performed by me as part of the ATLAS collaboration. In a large collaboration such as ATLAS very little can be described as wholly individual work and the work contained within this thesis is no exception. Below I list the major projects on which I have worked during my DPhil with a short summary of my main contributions. In the main body of the text I begin the major chapters with a similar summary, however it is difficult to provide a comprehensive summary in this way given that many important decisions and studies were performed collaboratively. Whenever a diagram, plot or other figure appears which I did not directly produce this is noted in that figure's caption. Some of these figures have been published by the ATLAS collaboration, in which case they are labeled '**ATLAS**' or '**ATLAS** Preliminary'.

Searches for new physics in final states with high jet multiplicities. I have been a member of this analysis team for the duration of my whole DPhil, becoming lead analyser and analysis contact from mid-2017 to mid-2018, overseeing much of the preliminary research and development preparing for the analysis of the full Run 2 dataset. During this time the analysis group has published 2 papers [1] and [2], the second of which is the focus of much of chapter 5. I wrote and maintained a software framework which was responsible for performing the analysis selections and the plotting of many important variables. I also performed studies important for the optimisation of signal selections.

Measuring and characterising the $E_{\mathrm{T}}^{\mathrm{miss}}$ trigger performance. From early 2015 to the present I have been very active in the $E_{\mathrm{T}}^{\mathrm{miss}}$ trigger group. One of my first tasks in this group, and one which I have continued to perform, was to measure and characterise the performance of the trigger in data events. In 2015, part of this task was to compare the performance of several different algorithms. These studies formed part of [3] and I produced most of the figures in the $E_{\mathrm{T}}^{\mathrm{miss}}$ trigger section of that paper; they are covered in first part of chapter 4. The studies were also used to devise the trigger strategy for 2016 and similar studies of subsequent years have also been instrumental in forming future strategies.

Validation and maintenance of the $E_{\mathrm{T}}^{\mathrm{miss}}$ trigger online software. One of my other tasks as a member of the trigger group has been to validate changes in the trigger software. The software is deployed online and any mistakes can lead to a loss of crucial data. I was also responsible for aiding in the software implementation of new algorithms.

Investigations into $E_{\mathrm{T}}^{\mathrm{miss}}$ trigger rate mitigation strategies. During 2016 the full dependence of the $E_{\mathrm{T}}^{\mathrm{miss}}$ trigger rate on pileup became clear. This constituted somewhat of a crisis for the trigger group as the rates of the primary $E_{\mathrm{T}}^{\mathrm{miss}}$ trigger far outstripped its allowable budget. I performed many studies over this period, some alone, some in small groups, to try and diagnose this problem and find potential fixes. The final strategy decided upon was one I developed and is covered in the second part of chapter 4.

Development of a software framework for assessing the performance of the $E_{\mathrm{T}}^{\mathrm{miss}}$ trigger. I developed a complete software framework for $E_{\mathrm{T}}^{\mathrm{miss}}$ trigger performance studies and to be used in developing new algorithms. This framework is able to perform multiple different signal-like event selections, emulate new and current trigger algorithms and produce many of the plots used to assess the trigger's performance.

Abstract

One of the most obvious problems with the Standard Model is the lack of any explanation for dark matter: a form of matter predicted from astrophysical observations but not compatible with any known subatomic particle. Many theories of new physics predict dark matter candidates which could be produced in 13 TeV collisions at the LHC. The primary experimental signature expected to accompany the production of a dark matter candidate is an imbalance in measurements of transverse momenta, referred to as $E_{\mathrm{T}}^{\mathrm{miss}}$. This thesis first covers the $E_{\mathrm{T}}^{\mathrm{miss}}$ trigger, a system responsible for selecting events with large $E_{\mathrm{T}}^{\mathrm{miss}}$ for later use in analyses and a vital component in many analyses. This signature suffers from very large backgrounds from QCD events with little true $E_{\mathrm{T}}^{\mathrm{miss}}$ and the high thresholds that would be required to control pass rates pose a risk to the efficiencies of analyses. A technique is presented that is shown to be able to reduce the rate by a factor of almost 4 while retaining high efficiencies in analysis signal regions. This thesis then documents a search for new physics using $36.1\,\mathrm{fb}^{-1}$ of data collected by the ATLAS detector. The search targets final states with no leptons and very high jet multiplicities, ranging from ≥ 7 to ≥ 11 in the tightest signal regions, which are characteristic of long decay chains which can be predicted by certain new physics models, especially supersymmetry. By using this signature the analysis is able to use a looser selection on $E_{\mathrm{T}}^{\mathrm{miss}}$, gaining sensitivity to areas of model spaces which may not be accessible to analyses reliant on the $E_{\mathrm{T}}^{\mathrm{miss}}$ trigger. No significant deviation from the Standard Model is observed and the analysis sets strong limits on the masses of supersymmetric particles, excluding gluino masses up to 1.8 TeV at the 95% confidence level.

Contents

There is a theory which states that if ever anyone discovers exactly what the Universe is for and why it is here, it will instantly disappear and be replaced by something even more bizarre and inexplicable.

There is another theory which states that this has already happened.

— Douglas Adams *The Restaurant at the End of the Universe*

1 Introduction

The history of scientific endeavour can be traced back thousands of years to some of the earliest human civilisations, though few records from these times survive. Egyptian medical papyri dating back to the 16^{th} century BC show evidence of empiricism in medical practice. Cuneiform records from 1^{st} millennium BC Mesopotamia show early efforts of Babylonian astronomy to apply a mathematical description to observed phenomena, with the Venus tablet of Ammisaduqa recording measurements of the rising and setting of Venus believed to date back to the 17^{th} century BC.

This quest for understanding has been an important aspect of many cultures around the world. The Classical and Hellenistic periods of Greek history, covering most of the first 5 centuries BC, are notable for developments in philosophy and science. Scientific advancements also characterised the Islamic Golden Age, dated between the 8^{th} and 14^{th} centuries. The Enlightenment, beginning in 18^{th} century western Europe, was heavily influenced by the Scientific Revolution.

One of the most fundamental questions of science is to ask what the world around us is made of. Leucippus and Democritus in Greece coined the word 'atom' to describe indivisible building blocks and Kanada in ancient India attempted to explain observations of the world in terms of similar objects called '*anu*'.

The modern study of particle physics seeks to answer the same question and could be seen beginning over two thousand years later, with Thomson, Townsend and Wilson's 1897 discovery of the electron: the first directly observed fundamental particle. The following century saw the rapid expansion of this field, yielding the discovery of more such particles. This was also accompanied by a revolution in theory, leading to the birth of quantum physics. The predictions of these new theories required higher and higher energies to probe, leading to the construction of larger and more complicated machines to test them. This led to the development of the Standard Model of particle physics, culminating in 2012 with the joint announcement from the ATLAS and CMS collaborations of the discovery of the Higgs boson.

However the Standard Model is still not capable of explaining all physical phenomena in the world around us; the fundamental question remains open. One of the issues is the problem of dark matter, revealed by astrophysical observations but incompatible with any known particle. This is the issue with which this thesis is primarily concerned, presenting two complementary approaches for searching for candidate particles.

Chapter 2 provides a theoretical overview of the standard model. It then progresses to talk about some of the problems with the theory and a possible extension to it called supersymmetry (SUSY). Chapter 3 introduces the Large Hadron Collider (LHC) and the ATLAS detector: the experimental apparatus used to collect all of the data in this thesis.

Chapter 4 discusses the trigger: a vital part of the ATLAS detector. In particular this chapter discusses the $E_{\mathrm{T}}^{\mathrm{miss}}$ trigger which is very commonly used in searches for dark matter candidates. The improved performance of the LHC makes the measurement of this quantity at the trigger level much tougher. These effects are discussed in this chapter and a technique to control rates is presented which is likely to remain a significant part of the ATLAS $E_{\mathrm{T}}^{\mathrm{miss}}$ trigger group strategy as the LHC program continues.

Chapter 5 discusses a search for physics beyond the standard model. Certain SUSY theories predict the production of gluinos, the superpartners of the gluon, which decay via a cascade producing a large quantity of hadronic particles in the final state. The measurement of such states is extremely challenging, as is the modelling of the backgrounds, leading to the use of a specialised data-driven background estimation technique. No significant deviations from the Standard Model are observed and limits are set on a variety of new physics models.

The thesis is then summarised in chapter 6.

2

Theory

Contents

2.1 Introduction

This chapter describes the Standard Model of particle physics, the theory that is currently best able to describe the behaviour and interactions of matter with the exclusion of gravity. While this thesis is mostly preoccupied with the experimental side of particle physics an understanding of the fundamentals of the underlying theory remains vital. First an overview of the particle content of the Standard Model will be covered. Then the underlying theory will be summarised, including the predicted phenomenology and some of its problems. Finally, an extension to the Standard Model will be covered, which aims to correct some of these problems.

Much of this chapter was written using the references [4–7].

2.2 Standard Model

2.2.1 Overview

The Standard Model is based on quantum field theory (QFT) in which the universe is modeled as a set of interacting quantum fields. Quantised excitations of these fields from the vacuum state correspond to the waves and particles that were the building blocks of previous theories. These particles can be divided into the fermionic particles which form the basis for all known matter, the gauge bosons which mediate the interactions between them and the Higgs boson which is responsible for providing a mechanism for these particles to acquire mass. The behaviour of these fields is described by the Lagrangian of the theory.

The Lagrangian is an equation which describes the dynamics of a system. In a classical theory the system will obey the principle of least action and evolve following a path which extremises the action, defined as the time integral of the Lagrangian, $S = \int \mathrm{d}t L$. In quantum field theory instead the probability amplitude for the system to evolve between two points in space-time is proportional to the sum over all possible paths between those points weighted by a factor $e^{iS/\hbar}$ [8].

The fermionic particles are divided into two main groups, the leptons and the quarks, each consisting of three generations of increasing mass. The leptons are further grouped into the charged leptons, usually denoted ℓ, and the neutrinos, denoted ν. The three generations of charged leptons are in increasing order of mass the electron (e), the muon (μ) and the tau (τ). Each has an associated flavour of neutrino which carries no electric charge and interacts only weakly.

The quarks come in both 'up-type' and 'down-type' varieties. The three generations of 'up-type' quarks are the 'up' (u), 'charm' (c) and 'top' or 'truth' (t). The 'down-type' quarks are the 'down' (d), 'strange' (s), and 'bottom' or 'beauty' (b). These bind together under the influence of the strong force forming hadrons, for example the protons (p) and neutrons (n) which, with electrons, form all of the matter with which we interact on a day-to-day basis.

The gauge bosons mediate the various interactions in the Standard Model. The photon (γ) mediates the electromagnetic interaction. The $W^{\pm}$ and Z bosons mediate the weak force which is involved in nuclear decays. The gluons (g) mediate the strong interaction, binding quarks together into hadrons.

2.2.2 Scattering theory

2.2.2.1 Fermi's Golden Rule

A key quantity in particle physics is the *cross-section* denoted σ. This corresponds to the ratio between the rate at which events of a particular process occur and the input flux of particles.

$$\sigma_{i\to f} = \frac{\Gamma_{i\to f}}{J}$$

This rate can also be expressed to first order in Fermi's 'Golden Rule' [9]

$$\Gamma_{i\to f} = \frac{2\pi}{\hbar} |\langle f| H_{\text{int}} |i\rangle|^2 \rho$$

where f and i label the final and initial states respectively, H_{int} is the Hamiltonian that describes the interaction and ρ is the density of final states. These two equations can be combined into an expression for the cross-section

$$\sigma_{i\to f} = \frac{2\pi}{\hbar J} |M_{fi}|^2 \rho$$

where J is the flux factor. The normalisations of the initial and final states are chosen to correspond to $\frac{1}{\gamma V}$. The *matrix element* M_{fi} is equivalent of $\langle f| H_{\text{int}} |i\rangle$ but is not restricted to first order information. The cross-section then depends only on two quantities: M_{fi} and ρ. The density of states is not Lorentz invariant however, so it is modified to construct the Lorentz invariant phase space element Φ.

The 2-body phase space element is

$$\Phi_2 \propto \frac{p}{E_{\text{CM}}}$$

where p is the momentum of either particle measured in the centre of mass frame and E_{CM} is the total centre of mass energy. This is maximised in the limit $m \to 0$.

The matrix element $\mathcal{M}_{fi}$ can be calculated using perturbation theory from the Lagrangian of the theory which will be the focus of the rest of this section.

2.2.3 Gauge Symmetries

Much of the Standard Model can be explained in terms of *symmetries*. A symmetry is a transformation under which the predictions of the theory do not change. These symmetries can be divided into continuous symmetries which can be constructed in small increments and discrete symmetries which cannot.

An important impact of symmetries is shown from Noether's first theorem [10, 11]: any continuous symmetry of the Lagrangian generates a conservation law. For instance, invariance under Poincaré group transformations (translations, rotations and Lorentz boosts) produces the conservation of momentum, angular momentum and the position of the centre of mass at time 0.

The most important symmetries in the Standard Model are the gauge symmetries. These can be demonstrated using the Lagrangian for a Dirac spinor ψ.

$$\mathcal{L} = \bar{\psi}(i\partial\!\!\!/ - m)\psi$$

If we consider a global U(1) symmetry $\psi \to e^{iq\alpha}\psi$ it is clear that this Lagrangian is invariant under this transformation. However, if we instead let this symmetry become local, that is we let α become a function of the space-time coordinates $\alpha(x)$

then this invariance is broken by the derivative as $\partial\!\!\!/\psi$ becomes $e^{iq\alpha}(\partial\!\!\!/ + iq\partial\!\!\!/\alpha)\psi$. In order to retain invariance under this transformation we need to convert the derivative ∂_μ to a *gauge covariant derivative* $D_\mu = \partial_\mu - iqA_\mu$ where the new vector field A_μ transforms as $A_\mu \to A_\mu + \partial_\mu\alpha$. With this change we now have a local U(1) invariant Lagrangian and we have also gained an interaction term $q\bar{\psi}A\!\!\!/\psi$ which represents the interaction between a Dirac fermion with charge q and the electromagnetic field (A_μ being the four-vector electromagnetic potential). Note that in order to be a full Lagrangian the kinetic term for the A_μ field must also be added. This will be covered in section 2.2.4. However this must be a massless field as no A_μ mass term can be added to this Lagrangian without breaking the gauge invariance. Similar arguments hold for more complicated groups than U(1), these will be covered in the same section. These local symmetries are commonly called 'gauge' symmetries.

2.2.4 The Standard Model Lagrangian

The full Standard Model Lagrangian excluding the Higgs mechanism (section 2.2.4.1) can be written as [12]

$$\begin{aligned}\mathcal{L} = &-\frac{1}{4}\mathbb{B}_{\mu\nu}\mathbb{B}^{\mu\nu} - \frac{1}{4}\mathrm{Tr}\left[\mathbb{W}_{\mu\nu}\mathbb{W}^{\mu\nu}\right] - \frac{1}{4}\mathrm{Tr}\left[\mathbb{G}_{\mu\nu}\mathbb{G}^{\mu\nu}\right] \\ &+ \bar{L}_j iD\!\!\!\!/ L_j + \bar{\ell}_{R_j} iD\!\!\!\!/ \ell_{R_j} + \bar{Q}_j iD\!\!\!\!/ Q_j + \bar{u}_{R_j} iD\!\!\!\!/ u_{R_j} + \bar{d}_{R_j} iD\!\!\!\!/ d_{R_j}\end{aligned} \tag{2.1}$$

where[1]

- $\mathbb{B}_{\mu\nu} = \partial_\mu B_\nu - \partial_\nu B_\mu$,
- $\mathbb{W}^i_{\mu\nu} = \partial_\mu W^i_\nu - \partial_\nu W^i_\mu + g\epsilon^{ijk}W^j_\mu W^k_\nu$,
- $\mathbb{G}^a_{\mu\nu} = \partial_\mu G^a_\nu - \partial_\nu G^a_\mu + g_s f^{abc}G^b_\mu G^c_\nu$,

are the tensors corresponding to the gauge fields, the traces in the Lagrangian sum over the 3 W fields and the 8 G fields. The fermionic matter fields $L_j, \ell_{R_j}, Q_j, u_{R_j}, d_{R_j}$ are summarised in table 2.1. The left-handed leptons combine into the $\mathrm{SU}(2)_L$ doublets L_j, the left-handed quarks into the Q_j doublets. The right-handed

[1] Recalling that the left/right handed parts of a spinor wave functions are given by $f_{L,R} = \frac{1}{2}(1 \mp \gamma_5)f$, that $\bar{f} = f^\dagger\gamma^0$ and that $A\!\!\!/ = \gamma_\mu A^\mu$

	Generations			Charges			
	1	2	3	Y	I	I_3	Q
L	$\begin{pmatrix}\nu_e\\ e_L\end{pmatrix}$	$\begin{pmatrix}\nu_\mu\\ \mu_L\end{pmatrix}$	$\begin{pmatrix}\nu_\tau\\ \tau_L\end{pmatrix}$	$\begin{pmatrix}-1\\ -1\end{pmatrix}$	$\begin{pmatrix}\frac{1}{2}\\ \frac{1}{2}\end{pmatrix}$	$\begin{pmatrix}+\frac{1}{2}\\ -\frac{1}{2}\end{pmatrix}$	$\begin{pmatrix}0\\ 1\end{pmatrix}$
ℓ_R	e_R	μ_R	τ_R	-2	0	0	-1
Q	$\begin{pmatrix}u\\ d\end{pmatrix}$	$\begin{pmatrix}c\\ s\end{pmatrix}$	$\begin{pmatrix}t\\ b\end{pmatrix}$	$\begin{pmatrix}\frac{1}{3}\\ \frac{1}{3}\end{pmatrix}$	$\begin{pmatrix}\frac{1}{2}\\ \frac{1}{2}\end{pmatrix}$	$\begin{pmatrix}+\frac{1}{2}\\ -\frac{1}{2}\end{pmatrix}$	$\begin{pmatrix}+\frac{2}{3}\\ -\frac{1}{3}\end{pmatrix}$
u_R	u_R	c_R	t_R	$\frac{4}{3}$	0	0	$+\frac{2}{3}$
d_R	d_R	s_R	b_R	$-\frac{2}{3}$	0	0	$-\frac{1}{3}$

Table 2.1: The chiral fermion fields in the Standard Model, organised into the doublets and singlets that form under the $SU(2)_L \times U(1)_Y$ electroweak interaction. Also shown are the charges of fields under the $SU(2)_L \times U(1)_Y$ transformation which are the same for all of the generations. These are the weak hypercharge Y and the total and third components of the weak isospin, I and I_3 respectively. The electric charge can be calculated from these $Q = {}^1\!/_2 Y + I_3$ (equation 2.3).

quarks and charged leptons are singlets under $SU(2)_L$. The j indices run over the three generations.

The gauge covariant derivatives D_μ are

$$D_\mu = \partial_\mu - \frac{1}{2}ig'YB_\mu - igI\tau^i W^i_\mu - \frac{1}{2}ig_s S\lambda^a G^a_\mu \tag{2.2}$$

where

- Y is the hypercharge which can vary between the different fermion states,
- I is the weak isospin of the fermion which is 1/2 for left-handed fermions and 0 for right-handed fermions,
- S is 1 for quarks and 0 for leptons,
- $\frac{1}{2}\tau^i$ are the generators of the $SU(2)_L$ group, τ^i are the Pauli matrices,
- $\frac{1}{2}\lambda^a$ are the generators of the $SU(3)_c$ group, λ^a are the Gell-Mann matrices,
- g, g', and g_s are the coupling constants of the $U(1)_Y$, $SU(2)_L$ and $SU(3)_c$ respectively.

The I and S factors ensure that the gauge covariant derivative only contains the W term when acting on left-handed fermions and the G term when acting on quarks.

A few further comments are necessary. First, we note that the structure constants ϵ^{ijk} for $\mathrm{SU}(2)_L$ and f^{abc} for $\mathrm{SU}(3)_c$ are given by the commutation relations between their generators: $\left[\frac{1}{2}\lambda^a, \frac{1}{2}\lambda^b\right] = \frac{1}{2}if^{abc}\lambda^c$. Second, that there are in truth 3 different sets of quark fields, corresponding to different colour charges. This can have an impact on measurable parameters; for example, W decays are more likely to go to hadronic final states as there are more quark fields than lepton fields.

This Lagrangian is invariant under the combined $\mathrm{SU}(3)_c \times \mathrm{SU}(2)_L \times \mathrm{U}(1)_Y$ symmetry. Under this symmetry the fermionic fields transform as

$$\psi \to \exp\left\{\frac{1}{2}iY\beta(x)\right\}\exp\left\{iI\tau^i\alpha^i(x)\right\}\exp\left\{\frac{1}{2}iS\lambda^a\gamma^a(x)\right\}\psi$$

and the gauge fields transform as

$$\begin{aligned}
B_\mu &\to B_\mu + \frac{1}{g'}\partial_\mu\beta(x), \\
W^i_\mu &\to W^i_\mu + \frac{1}{g}\partial_\mu\alpha^i(x) - \epsilon^{ijk}\alpha^j W^k_\mu, \\
G^a_\mu &\to G^a_\mu + \frac{1}{g_s}\partial_\mu\gamma^a(x) - f^{abc}\gamma^b G^c_\mu.
\end{aligned}$$

The Lagrangian also retains some excess unphysical degrees of freedom which correspond to the free choice of the three gauge symmetries. These can be removed using gauge-fixing and ghost terms but these are not required to build a phenomenological picture of the theory, so are not covered here.

2.2.4.1 Electroweak Symmetry Breaking

There are some obvious issues with the Lagrangian in equation 2.1. We cannot add any mass terms to this Lagrangian without breaking the gauge symmetry. This is obvious for the gauge fields, for the fermion fields it is because the mass term $\bar{\psi}m\psi = \bar{\psi}_R m\psi_L + \bar{\psi}_L m\psi_R$ would mix the left and right-handed components which transform differently. We also note that the W^i and B fields are not exactly the $W^\pm, Z$ and A fields that we observe in experiments.

The technique used here is known as *spontaneous symmetry breaking.* In this model, while the Lagrangian is invariant under the symmetry in question, the vacuum state is not. Therefore when considering the physical fields, which correspond to small excursions from the vacuum, they do not behave in a way which respects the symmetry.

A full derivation can be found in appendix A, what follows here is a brief summary of the key findings. We introduce a new complex $\mathrm{SU}(2)_L \times \mathrm{U}(1)_Y$ scalar doublet which has a non-trivial vacuum expectation value $\langle \Phi^\dagger \Phi \rangle = v$. This vacuum state breaks the $\mathrm{SU}(2)_L \times \mathrm{U}(1)_Y$ symmetry.

When expanding the fields around the vacuum state, it becomes a natural choice to mix the $\mathrm{SU}(2)_L \times \mathrm{U}(1)_Y$ bosons. The charged $W^\pm$ bosons are given by $W^\pm = {}^1\!/\!\sqrt{2}(W^1 \pm iW^2)$ and the A and Z bosons are formed by rotating the B and W^3 bosons through an angle θ_W. Of the four degrees of freedom present in the original scalar doublet, one remains as a new scalar field h, called the Higgs boson; all particles which acquire masses through the Higgs mechanism also acquire couplings to this field. The other three are absorbed by the $W^\pm$ and Z bosons as they acquire mass terms. The masses of the bosons are given by $m_W = \frac{1}{2}vg$ and $m_Z = \frac{1}{2}v\frac{g}{\cos\theta_W}$.

The fermions acquire mass through couplings with the scalar doublet. Expanding around the vacuum state generates the required fermion mass terms $\bar{\psi}_i m_{ij} \psi_j$. In general, the mass matrix m_{ij} does not have to be diagonal, meaning that the 'mass' eigenstates of the theory can differ from the 'weak' eigenstates considered so far. The effects of this are covered in section 2.2.5.

The Lagrangian resulting from this symmetry breaking is still invariant under a $\mathrm{U}(1)_{\mathrm{EM}}$ symmetry. The corresponding massless boson is the photon A_μ so we identify this symmetry with electromagnetism. Substituting the A_μ and Z_μ fields into the expression for the covariant derivative (equation 2.2) yields an expression for the unit electromagnetic charge

$$e = g'\cos\theta_W = g\sin\theta_W$$

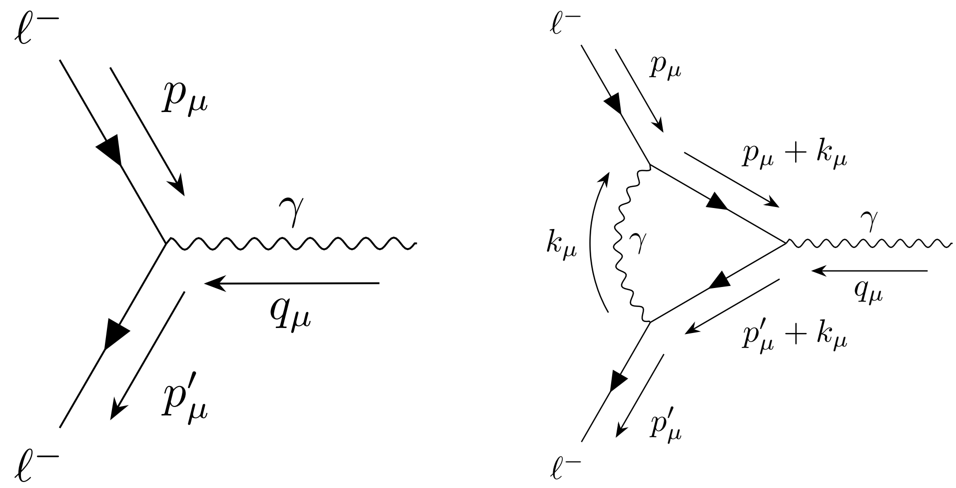

(a) Tree level **(b)** One Loop

Figure 2.1: The three-point vertex showing the interaction between a charged lepton and a photon. The tree-level diagram is shown on the left and the one-loop correction to it on the right. The four-momenta associated to the particles are also indicated with momentum conservation at each vertex implying that $p_\mu + q_\mu = p'_\mu$.

and the charge for a particle

$$Q = \frac{1}{2}Y + I_3. \tag{2.3}$$

2.2.4.2 Renormalisation and Factorisation

When calculating the matrix element for a process all possible diagrams with matching external lines will contribute to the amplitude. This results in an infinite sum which is not calculable. Within perturbation theory we approximate this sum by only considering terms up to a particular order in some vertex factor which should be sufficiently less than unity. However, within the expansion we will also find diagrams like 2.1b providing a correction to the tree level diagram 2.1a. Within this diagram there is a loop with a four-momentum k_μ passing through it; this momentum is unconstrained and so must be integrated over, when this is done it is found that the integral diverges.

This is, perhaps, to be expected. In integrating to arbitrarily high momentum states we access energy scales far beyond any which we have observed in experiments. At these scales the Standard Model is not expected to be accurate as contributions from any new physics will become important. However, we still want a predictive theory at scales currently accessible to experiments so we need a method to remove these divergences. This method is called *renormalisation*.

The divergent terms in the integral can be studied by imposing a renormalisation condition that truncates the integral at some scale Λ. Allowing $\Lambda \to \infty$ the integral can be separated into finite and divergent pieces. The divergent part is removed by inserting an appropriate counter-term in the Lagrangian but the finite term depends on the momentum scale μ being considered and cannot be so simply removed. This has the effect of replacing the 'bare' parameters in the original Lagrangian with physical 'renormalised' parameters which correspond to those measured in experiments. Through this process these renormalised parameters acquire a dependence on the momentum scale present in the experiment. In the case of coupling constants this is known as 'running'.

A similar issue occurs when considering the probability for the emission of a massless particle from one of the participating particles. In the limit of a *soft*, *colinear* emission, i.e. one in which the emitted particle's momentum relative to the parent tends to 0, the amplitude for this process diverges. As with renormalisation, a scale can be introduced which truncates this integral above the divergence which is then canceled through the introduction of counter-terms. This, again, leaves a residual scale-dependence that must be allowed for, usually called the *factorisation* scale. The dependence of predictions on this scale is typically absorbed into the prediction of the initial state (section 2.2.5.5).

It is important to note that the choice of renormalisation and factorisation scales to use is essentially arbitrary, but the prediction obtained is dependent on both of them [2]. In order to retain predictive power this dependence must be small [13]. Typically the chosen renormalisation and factorisation scales are varied (for example from $Q/2$ to $2Q$ for a nominal value of Q) and differences in predictions taken as a systematic uncertainty (section 5.6).

[2] Were it possible to predict to all orders of perturbation theory this dependence would vanish.

Leptons	
m_e	$0.5110\,\text{MeV}$
m_μ	$105.7\,\text{MeV}$
m_τ	$1777\,\text{MeV}$
m_ν	$< 2\,\text{eV}$
Quarks	
m_u	$2.2^{+0.5}_{-0.4}\text{MeV}$
m_d	$4.7^{+0.5}_{-0.3}\text{MeV}$
m_s	95^{+9}_{-3}MeV
m_c	$1.275^{+0.025}_{-0.035}\text{GeV}$
m_b	$4.18^{+0.04}_{-0.03}\text{GeV}$
m_t (from direct measurements)	$173.0 \pm 0.4\text{GeV}$
Bosons	
m_W	$80.379 \pm 0.012\text{GeV}$
m_Z	$91.1876 \pm 0.0021\text{GeV}$
m_h	$125.18 \pm 0.16\text{GeV}$

Table 2.2: The masses of the Standard Model particles. Where uncertainties are not shown they are smaller than the precision stated. Units follow the natural units proscription where $c = \hbar = 1$. Only the 95% confidence level limit on the largest neutrino mass is shown, not the full spectrum.

2.2.5 Phenomenology

As the Standard Model is important primarily in its capacity as a predictive theory we now turn to its predictions. In order to study these we break the Lagrangian into three separate pieces: $\mathcal{L}_{\text{QCD}}$, $\mathcal{L}_{\text{EW}}$ and $\mathcal{L}_{\text{Higgs}}$. These components are not directly summed as some terms, for example the derivatives of the fermion fields, would then appear multiple times. The corresponding interaction vertices generated by this Lagrangian are shown here without annotation to show the vertex factors as these are not necessary for a qualitative understanding of the interactions. All diagrams are drawn in the unitary gauge. A full set of diagrams including ghosts can be found in reference [14].

The masses of the particles are shown in table 2.2 and are taken from [15] which collates the results of many different experiments.

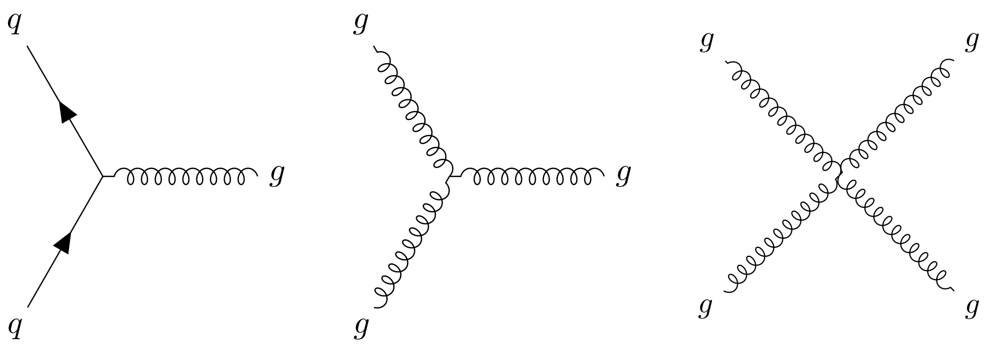

(a) Quark-gluon **(b)** Triple gluon **(c)** Quartic gluon

Figure 2.2: The QCD vertex diagrams showing the interactions between quarks and gluons.

2.2.5.1 Quantum Chromodynamics

The QCD Lagrangian describing quark and gluon interactions is

$$\mathcal{L}_{\mathrm{QCD}} = -\frac{1}{4}\mathrm{Tr}\left[\mathbb{G}_{\mu\nu}\mathbb{G}^{\mu\nu}\right] + \sum_j i\bar{\boldsymbol{\psi}}_j(i\partial\!\!\!/ - m_j - \frac{1}{2}ig_s\lambda^a G\!\!\!/^a)\boldsymbol{\psi}_j$$

where the 3 elements of the $\boldsymbol{\psi}$ vector correspond to the 3 colours and the j index cycles over the 6 different mass eigenstates. The gluons also carry colour charge and therefore also interact with each other, this can be seen from the structure of the field strength tensor $\mathbb{G}^a_{\mu\nu}$. The interaction vertices generated from this Lagrangian are shown in figure 2.2.

The fact that the gluons interact with each other has another important implication. When considering the running of the strong coupling it is found that it decreases with the momentum scale, unlike the electromagnetic coupling which increases. This leads to two very important properties of the strong force: *colour confinement* and *asymptotic freedom*.

Colour confinement refers to the fact that at low momentum scales the strong coupling constant $\alpha_s = g_s^2/4\pi$ approaches unity and perturbation theory can no longer be applied. At these scales the quarks bind into colourless states, either consisting of 3 (anti)quarks with orthogonal colour states or a quark-antiquark pair with opposing colour states. As quarks produced in particle collisions separate[3] the

[3]recalling that large distance scales correspond to low momentum scales

energy contained in the gluon field grows until it is more energetically favourable to produce a new quark-antiquark pair. This continues until the the energy supply is depleted. The directions of the quarks produced by this process are highly correlated with the directions of the original quarks so this produces sprays of highly collimated hadrons called jets [16], the 'original' quark being contained in one of the hadrons.

Asymptotic freedom then occurs at high momentum scales. The strong coupling constant reduces at these scales and the Hamiltonian approaches asymptotically a free Hamiltonian of which the quarks and gluons are eigenstates.

2.2.5.2 Electroweak Phenomenology

The electroweak Lagrangian after electroweak symmetry breaking is

$$\begin{aligned}\mathcal{L}_{\mathrm{EW}} =& -\frac{1}{4}\mathbb{B}_{\mu\nu}\mathrm{B}^{\mu\nu} - \frac{1}{4}\mathrm{Tr}\left[\mathbb{W}_{\mu\nu}\mathbb{W}^{\mu\nu}\right] + m_W^2 W_\mu^+ W^{-\mu} + \frac{1}{2}m_Z^2 Z_\mu Z^\mu \\ &+ \sum_j \bar{\ell}_j(\partial\!\!\!/ - m_{\ell_j})\ell_j + \bar{q}_j(i\partial\!\!\!/ - m_{q_j})q_j \\ &+ \frac{g}{2\sqrt{2}}\left[J_\mu^- W^{+\mu} + J_\mu^+ W^{-\mu}\right] + eJ_\mu^{\mathrm{EM}}A^\mu + \frac{g}{\cos\theta_W}(J_\mu^3 - \sin^2\theta_W J_\mu^{\mathrm{EM}})Z^\mu.\end{aligned}$$

The field strength tensors are left in their unmixed forms for simplicity. The j index cycles over the charged lepton and quark mass eigenstates. The electroweak currents are defined as

$$\begin{aligned}J_\mu^- &= \sum_i \bar{\nu}_{iL}\gamma_\mu \ell_{Li} + \bar{u}_{iL}\gamma_\mu d'_{iL},\ J_\mu^+ = J_\mu^{-\dagger} \\ J_\mu^{\mathrm{EM}} &= \sum_i Q_i \bar{f}_i \gamma_\mu f_i \\ J_\mu^3 &= \sum_i I_{3i}\bar{f}_{iL}\gamma_\mu f_{iL}\end{aligned}$$

where the i index cycles over the lepton and quark flavour eigenstates (represented by the ν, ℓ, u and d' fields).

This Lagrangian generates the vertices shown in figure 2.3. An important subtlety was covered in section 2.2.4.1: there is no requirement for the mass eigenstates of the theory to be the same as the flavour eigenstates. The most general permitted relation between these states is $d' = Vd$ where V is the 3×3 CKM matrix [17]. The CKM matrix consists of 4 physical degrees of freedom: 3 angles and 1 complex

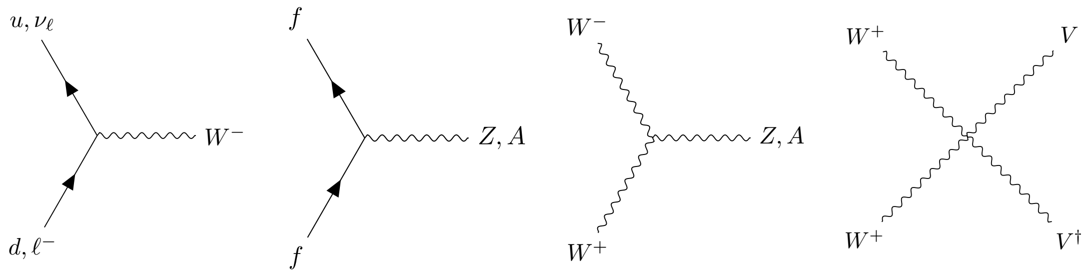

(a) CC **(b)** NC **(c)** Triple **(d)** Quartic

Figure 2.3: The electroweak vertex diagrams. V in 2.3d represents any of the 4 electroweak vector bosons and $V^\dagger$ its antiparticle.

phase. The 3 angles correspond to the mixing between the quark generations, without this the b and s quarks would be stable. The complex phase is currently the only known source of CP violation in the Standard Model.

The values of the inter and intra generational coupling factors (discarding the complex phase) are [15]

$$\begin{pmatrix} |V_{ud}| & |V_{us}| & |V_{ub}| \\ |V_{cd}| & |V_{cs}| & |V_{cb}| \\ |V_{td}| & |V_{ts}| & |V_{tb}| \end{pmatrix} = \begin{pmatrix} 0.97420 \pm 0.00021 & 0.2243 \pm 0.0005 & (3.94 \pm 0.36) \times 10^{-3} \\ 0.218 \pm 0.004 & 0.997 \pm 0.017 & (42.2 \pm 0.8) \times 10^{-3} \\ (8.1 \pm 0.5) \times 10^{-3} & (39.4 \pm 2.3) \times 10^{-3} & 1.019 \pm 0.025 \end{pmatrix}.$$

The phenomenology of the heavy quark decays is worth taking some time to consider. Owing to the enormous volume of phase space (section 2.2.2.1) available to its decay the t quark has an extremely short lifetime of approximately 5×10^{-25}s [18]. This is shorter than the timescale over which hadronisation [19] happens so t quarks do not hadronise.

Hadrons containing b quarks have lifetimes such that they decay a measurable distance away from the interaction point, but not so large that they decay outside of the detector material [20], largely due to the small sizes of $|V_{cb}|$ and $|V_{ub}|$. This, combined with the large mass difference between the b and its decay products, gives them a distinctive signature in the detector which can be used to identify them (section 3.5.2.2).

2.2.5.3 Neutrino Masses

When initially conceived neutrinos were thought to be massless. However, measurements of the fluxes of solar and atmospheric neutrinos (for example [21]) showed that neutrinos produced in one flavour state could 'oscillate' into another as they propagated. This implies that the flavour states are mixtures of different mass states, $\nu_f = U\nu_i$, where the matrix U is the 3×3 PMNS matrix [22]. If it is assumed that neutrinos are represented by Dirac spinors then the PMNS matrix takes the same form as the CKM matrix with 3 mixing angles θ_{ij} and one complex phase δ. However, as the neutrino is uncharged it is also possible that they are Majorana particles that are their own antiparticles, i.e. $\nu = \nu^{\dagger}$. In this case the PMNS matrix contains the same 3 mixing angles but *3* complex phases: δ, α_1 and α_2 though the flavour oscillation probabilities do not depend on the latter two phases [15]. The PMNS matrix is given by 3 rotations, the second of which depends on the complex phase δ and a phase matrix P

$$U = \begin{pmatrix} 1 & 0 & 0 \\ 0 & c_{23} & s_{23} \\ 0 & -s_{23} & c_{23} \end{pmatrix} \begin{pmatrix} c_{13} & 0 & s_{13}e^{-i\delta} \\ 0 & 1 & 0 \\ -s_{13}e^{i\delta} & 0 & c_{13} \end{pmatrix} \begin{pmatrix} c_{12} & s_{12} & 0 \\ -s_{12} & c_{12} & 0 \\ 0 & 0 & 1 \end{pmatrix} P.$$

The shorthand $c_{ij} = \cos\theta_{ij}$, $s_{ij} = \sin\theta_{ij}$ is used. The phase matrix P is the identity matrix in the Dirac case and $\mathrm{diag}(e^{i\alpha_1}, e^{i\alpha_2}, 1)$ in the Majorana case, though this parameterisation is not unique.

For Dirac neutrinos the free particle Lagrangian is the already familiar $\sum_j \bar{\nu}_j(i\partial\!\!\!/ - m_j)\nu_j$. For the Majorana case the corresponding term is $\sum_j i\bar{\nu}_j\partial\!\!\!/\nu_j - 1/2m_j(\bar{\nu}^C_{L_j}\nu_{L_j} + \bar{\nu}_{L_j}\nu^C_{L_j})$ where ν^C represents the charge conjugate of ν. In both cases j cycles over the mass states. In the Dirac case there must be 'sterile' right-handed neutrinos which carry no strong, weak or electromagnetic charge.

It is also possible to have a mass term formed from a mixture of a Majorana mass and a Dirac mass. If the Majorana mass is much greater than the Dirac mass this results in a 'seesaw' mechanism [23] where the sterile neutrinos have extremely high masses and the active neutrinos have the extremely low masses which we observe in experiments.

Experiments measuring neutrino oscillation are sensitive to parameters of the PMSN matrix and the differences between the squared masses of the different mass states. The current best experimental limits are shown in table 2.3. At present there is not sufficient experimental evidence to distinguish between the normal

	Normal order	Inverted order
$\sin^2\theta_{12}$	0.307 ± 0.013	
$\sin^2\theta_{23}$	$0.417^{+0.025}_{-0.028}$	$0.421^{+0.033}_{-0.025}$
$\sin^2\theta_{13}$	$(2.12 \pm 0.08) \times 10^{-2}$	
δ/π	$1.45^{+0.28}_{-0.33}$	$1.54^{+0.22}_{-0.26}$
Δm^2_{21}	$(7.53 \pm 0.18) \times 10^{-5}\mathrm{eV}^2$	
Δm^2_{32}	$(2.51 \pm 0.05) \times 10^{-3}\mathrm{eV}^2$	$(-2.56 \pm 0.04) \times 10^{-3}\mathrm{eV}^2$

Table 2.3: Current best experimental values for neutrino mixing parameters taken mostly from [15] with the values for δ taken from [24]. Values for $\sin^2\theta_{23}$ are shown assuming that θ_{23} lies in the first quadrant (i.e. $\theta_{23} \in [0, \pi/4]$). The squared mass differences are defined as $\Delta m^2_{ji} = m^2_j - m^2_i$.

order $m_1 < m_2 < m_3$ and the inverted order $m_3 < m_1 < m_2$. At the 3σ level the CP violating phase δ is essentially unconstrained. The contribution of CP violation from δ can be expressed in terms of the *Jarlskog invariant*

$$J_{\mathrm{CP}} = \frac{1}{8}\cos\theta_{13}\sin2\theta_{12}\sin2\theta_{13}\sin2\theta_{23}\sin\delta.$$

Its maximal value is $J^{\nu\max}_{\mathrm{CP}} = 0.0329 \pm 0.0007$, which can be compared to the corresponding value from the quark sector $J^{\mathrm{CKM}}_{\mathrm{CP}} = (3.04^{+0.21}_{-0.20}) \times 10^{-5}$, showing that the potential CP violation from the neutrino sector is far greater than that from the quark sector.

2.2.5.4 Higgs Lagrangian

The Lagrangian of the Higgs sector is

$$\begin{aligned}\mathcal{L}_{\mathrm{Higgs}} =& \frac{1}{2}(\partial_\mu h)^2 - \frac{1}{2}m_h^2 h^2 - \frac{m_h^2}{2v}h^3 - \frac{m_h^2}{8v^2}h^4 \\ &+ 2\frac{m_W^2}{v}hW^+_\mu W^{-\mu} + \frac{m_W^2}{v^2}h^2 W^+_\mu W^{-\mu} + \frac{m_Z^2}{v}hZ_\mu Z^\mu + \frac{1}{2}\frac{m_Z^2}{v^2}h^2 Z_\mu Z^\mu \\ &- \sum_j \sqrt{2}\frac{m_j}{v}h\bar{f}_j f_j\end{aligned}$$

where the v is the Higgs vacuum expectation value and the index j cycles over all of the fermions apart from neutrinos. A constant term of $^1/_4 m_h^2 v^2$ has been neglected. This generates the diagrams shown in figure 2.4. Note that the coupling of the Higgs boson to particles is proportional to the masses of those particles, meaning that the strongest coupling of the Higgs is to t quarks. The Higgs vacuum

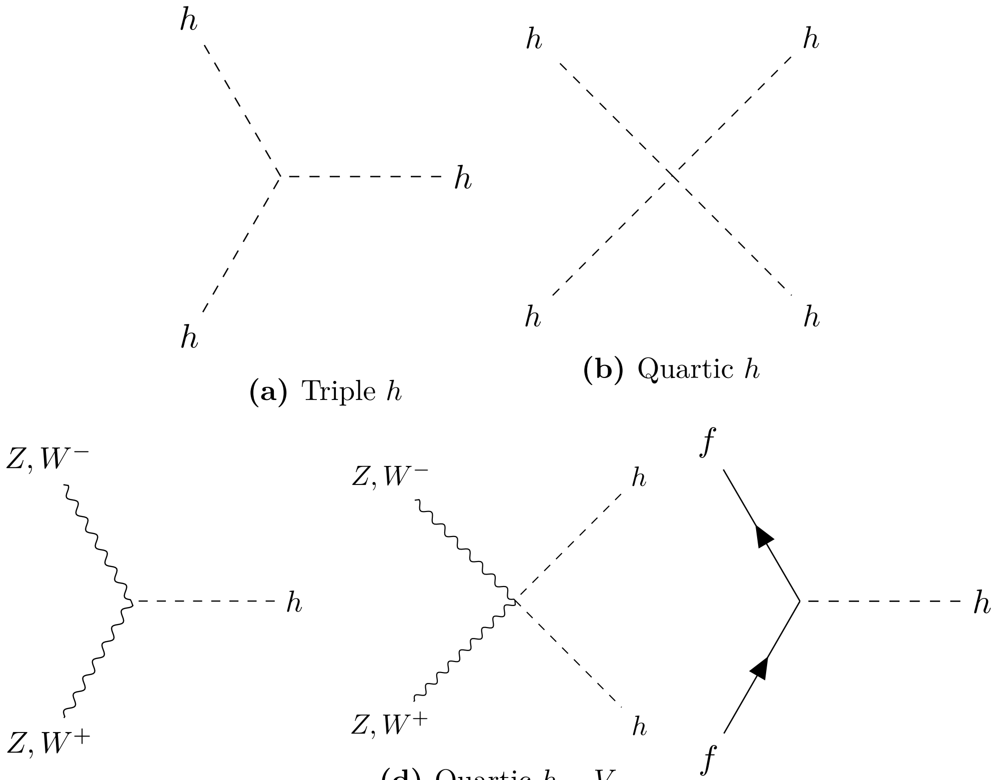

(a) Triple h

(b) Quartic h

(c) Triple $h - V$

(d) Quartic $h - V$

(e) Higgs-fermion

Figure 2.4: The Higgs vertex diagrams. The couplings to vector bosons are proportional to m_V^2, couplings to fermions are proportional to m_f.

expectation value can be calculated from the Fermi coupling and takes a value of [15] $v \approx (\sqrt{2}G_F)^{-1/2} \approx 246\,\mathrm{GeV}$.

2.2.5.5 Proton-Proton physics

One consequence of colliding composite particles like protons is that the initial state of the collision is not known. The observed final state could have resulted from an interaction between any pair of constituents in the incident protons, referred to as ‘partons’. These partons are not just the 3 ‘valence’ quarks which are usually thought of comprising a proton but also comprise a ‘sea’ predominately of gluons and quark-antiquark pairs [25].

This complicates the interpretation of data in two main ways. First, it is not possible to establish the rest frame of the collision; the two partons are not guaranteed to have equal and opposite momenta along the beam axis as measured in the laboratory frame. This motivates the use of 'transverse' quantities (e.g. p_{T}) as these are invariant under boosts along the beam axis.

Second, it is impossible to make accurate predictions about observed events without first knowing how likely it is for two partons of particular types to interact with each other. This information is encoded in parton distribution functions (pdfs), which can be shown to depend only on the momentum fraction x of the interacting parton and the magnitude of the four-momentum exchanged during the interaction Q^2. Crucially these pdfs do not depend on the nature of the interaction or indeed on the identity of the other interacting parton so can be measured in a variety of experiments [26–30].

2.2.5.6 $E_{\mathrm{T}}^{\mathrm{miss}}$

All of the matter particles of the Standard Model carry electric and/or strong charge except for the neutrinos. Particle detectors can measure these particles with high efficiencies (chapter 3) but particles like neutrinos which only interact weakly cannot be reliably detected. Dedicated detectors [31] can be constructed to identify these particles but these tend to include enormous active volumes which are impractical to include in an LHC experiment and even then do not show the high detection efficiencies necessary for LHC physics. Particles like these which only interact weakly are often referred to as 'invisible'.

However, the presence of these particles can still be inferred from measurements of the other particles produced in the collision by applying conservation of momentum. Given that the overall momentum along the beam axis is not known (section 2.2.5.5) this conservation can only be applied in the directions perpendicular to the beam axis. This motivates the use of the $E_{\mathrm{T}}^{\mathrm{miss}}$ observable, defined as the magnitude of the negative vector sum over the transverse momenta all detected particles. More details on the measurement and use of this variable are covered further in chapters 4 and 5.

In events where the only source of $E_{\mathrm{T}}^{\mathrm{miss}}$ comes from the decay of a massive particle into one visible and one invisible particle another useful observable can be constructed. Called the transverse mass, it is given by

$$m_T^2 = 2p_\mathrm{T}E_\mathrm{T}^\mathrm{miss}(1 - \cos\theta), \tag{2.4}$$

where p_T is the transverse momentum of the visible particle and θ is the angle between it and the measured $E_\mathrm{T}^\mathrm{miss}$. This is always less than p_W^2, the four-momentum squared of the massive particle. This means that for on-shell production of the massive particle m_T is bounded from above by the true invariant mass of the massive particle. This was used to measure the W mass at the Tevatron [32] and can also be a useful discriminant (see chapter 5 for example).

2.2.6 Problems with the Standard Model

While extremely successful the Standard Model is not a perfect theory, given that it does not include explanations for many important physical phenomena. Perhaps the most obvious is the lack of any explanation for gravity in the model. This is not too surprising; although gravity is in some respects the strongest force we encounter in everyday life it is extremely weak on the quantum scale, only really becoming relevant at energy scales close to the Planck mass $m_\mathrm{P} \approx 1.22 \times 10^{19}$GeV.

More concerning is the lack of any explanation for the cosmological phenomenon known as dark matter. Dark matter is a theory that explains many experimental discrepancies from measurements of galactic rotation curves [33] through observed patterns of gravitational lensing [34] to measurements of the cosmic microwave background (CMB) power spectrum [35]. Dark matter appears to be a form of matter which interacts gravitationally but not electromagnetically or strongly. Astrophysical observables rule out neutrinos as a source of this effect [36] and instead favour the existence of weakly interacting massive particles or WIMPs, which do not appear in the Standard Model. On a similar note, the Standard Model is unable to account for cosmological measurements of *dark energy* which is evidenced by the accelerating expansion of the universe [37].

As presented here, the Standard Model does not include a mechanism for generating neutrino mass terms which are necessary to explain the measured phenomenon of neutrino oscillation [38]. While these are not difficult to add, there is not yet enough experimental evidence to distinguish between the two leading theories, giving Dirac and Majorana mass terms alternately [39].

The predominance of matter over antimatter in the universe implies a certain amount of CP symmetry breaking. While there is a source of this arising from the CKM matrix 2.2.5.2 this is not sufficient to explain the observed matter-antimatter disparity [40].

There are also more cosmetic reasons to suppose that the Standard Model is not a complete theory. Excluding the neutrino sector there are 19 free parameters in the Standard Model with no real theoretical predictions of their values which must therefore be measured in experiments. In one representation[4] these free parameters are the 6 quark masses and 3 charged lepton masses, 4 CKM angles (3 mixing angles and 1 CP violating phase), the 3 gauge couplings, the Higgs vacuum expectation value and the Higgs mass, and finally the QCD vacuum angle. Including terms for neutrino masses adds at least 7 parameters in the case where neutrino masses are provided solely through a Dirac mechanism. The QCD vacuum angle θ arises from study of the QCD vacuum structure, in which one finds that an additional CP-violating term arises in the action of the system. That this parameter appears to be 0 when, a priori, it could take any value between 0 and 2π is known as the strong CP problem [41].

In a full theory one would hope to be able to derive a mechanism through which these parameters can be generated, just as electroweak symmetry breaking was able to relate the electromagnetic and weak couplings to the masses of the W and Z bosons. In such a theory the $\mathrm{SU}(3)_c \times \mathrm{SU2}_L \times \mathrm{U}(1)_Y$ structure of the Standard Model Lagrangian could be generated by the breaking of some higher order symmetry such as SU(5) [42]. If this were true then the running couplings of the Standard Model could be expected to all meet at some scale, commonly referred to as the *grand unified theory* (GUT) scale. However, in projections from the Standard Model this does not quite happen (figure 2.5).

[4]There is not a unique way to pick a set of free parameters.

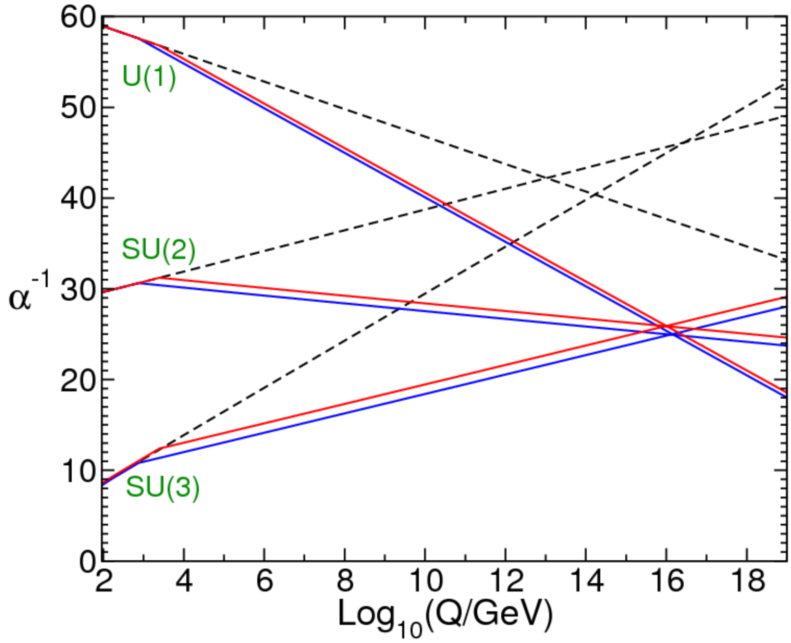

Figure 2.5: The running of the inverse gauge couplings is shown as a function of the mass scale. The Standard Model prediction is shown in the dashed line. The prediction from the MSSM (section 2.3) is shown in the solid lines. The sparticle masses are varied as a common threshold between 750 GeV and 2.5 TeV, and $\alpha_s(m_Z)$ between 0.117 and 0.120. Figure taken from reference [6].

There is also no explanation why exactly 3 generations of fermions are observed, nor why their masses cover such a broad range (table 2.2). The last of these is more generally known as a *hierarchy problem*, where the characteristic parameters of a theory appear at vastly different scales. Of these the most important is between the relative strengths of the weak and gravitational forces, which can be seen as being equivalent to the difference between the Higgs mass and the Planck mass. This will be covered further in the next section.

2.3 Supersymmetry

This section provides an overview of SUSY [43–48], a theoretical framework which extends the Standard Model. This is intended only as a brief introduction to some of the key concepts; a far fuller introduction can be found in reference [6].

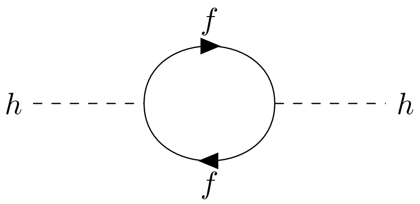

(a) Fermion

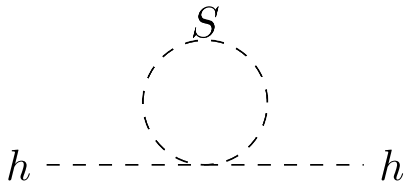

(b) Scalar

Figure 2.6: Feynman diagrams showing the first order loop corrections to the Higgs Mass for loops involving a fermion (2.6a) or a scalar (2.6b).

2.3.1 The hierarchy problem

The most obvious motivation for SUSY comes from the Higgs mass hierarchy problem[5]. Considering the 2-point Higgs function $-\frac{1}{2}m_h^2 h^2$ it is clear that this will receive corrections from diagrams like the one in figure 2.6a which result in a correction to the Higgs mass [6]

$$\delta m_h^2 = -\frac{|\lambda_f|^2}{8\pi^2}\Lambda_{\mathrm{UV}}^2 + O(m_f^2 \ln[\Lambda_{\mathrm{UV}}]) \tag{2.5}$$

where λ_f is the fermion's Yukawa coupling which was shown in appendix A to be proportional to the fermion mass and Λ_{UV} is the cut-off scale discussed in section 2.2.4.2. This cut-off scale should be seen as the scale at which new physics enters into the theory which must be at most the Planck mass, by which point effects from gravity become relevant.

This quadratic divergence is not seen in the corrections to the gauge boson masses as they are protected by a symmetry in the Lagrangian [49]. The natural question therefore is whether a symmetry can be found to similarly protect the Higgs mass; is there a diagram which contributes the opposite correction to the Higgs mass? The diagram in figure 2.6b corresponds to a term $-\lambda_S h^2 S^\dagger S$ in the Lagrangian and contributes a Higgs mass correction

$$\delta m_h^2 = \frac{\lambda_S}{16\pi^2}\Lambda_{\mathrm{UV}}^2 + O(m_S^2 \ln[\Lambda_{\mathrm{UV}}]).$$

[5] often referred to as just *the* hierarchy problem

So it would seem possible to cancel the quadratic divergence in the Higgs mass by introducing two such scalar fields with $\lambda_S = |\lambda_f|^2$ [6]. This requires a very different form of symmetry to any that has been shown so far: a symmetry that relates fermions and bosons.

Interestingly, the original motivation for SUSY was not to solve the hierarchy problem but rather arose from the observation (due to the Coleman-Mandula theorem) that this form of symmetry was the only possible extension of the Poincaré group [50, 51]. This also makes some form of SUSY a requirement for many quantum theories of gravity. This symmetry is the eponymous *supersymmetry* in the SUSY theory. It is formed by requiring that the Lagrangian is invariant under the action of some operator Q which converts fermion states to boson states (and vice versa) and obeys the algebra

$$\begin{aligned}
\{Q_\alpha, Q^\dagger_{\dot\alpha}\} &= -2\sigma^\mu_{\alpha\dot\alpha} P_\mu, \\
\{Q_\alpha, Q_\beta\} &= \{Q^\dagger_{\dot\alpha}, Q^\dagger_{\dot\beta}\} = 0, \\
[Q_\alpha, P_\mu] &= [P_\mu, Q^\dagger_{\dot\alpha}] = 0,
\end{aligned}$$

where P_μ is the momentum operator.

This results in requiring that for each particle degree of freedom in the Standard Model there exists another with the same quantum numbers differing only by a spin of 1/2. We call these extra particles *superpartners*. So, for any fermion f this results in the generation of *two* scalar fields S_L and S_R corresponding to the left and right handed pieces of the fermion. This is exactly what was required to cancel the quadratic divergence in the Higgs mass. Note that it is possible to define N versions of this Q operator but that theories with $N > 1$ are not chiral [52] so cannot correspond to the universe as we observe it.

[6] The change of sign results from the spin-statistic theorem and is a crucial difference between fermion and boson states.

2.3.2 Particle content in SUSY

It is necessary to form new multiplets under the action of Q which provide the full particle content in SUSY. These, excluding the graviton, are divided into *chiral* and *gauge* supermultiplets. The fermionic particles of the Standard Model all fall into chiral supermultiplets, the left and right handed parts being paired with scalar fields. By convention the names of these scalar fields are formed by prepending an s onto the name of the corresponding fermion field. The symbols for these fields are the same as for the fermion, except with a tilde. So the electron field e is paired with two *selectron* fields $\tilde{e}_L$ and $\tilde{e}_R$. Note that the L and R subscripts refer to the handedness of the fermion state; being scalars, the sfermions have no definition of handedness.

The gauge bosons are then associated with spin-1/2 fermions in gauge supermultiplets. As the gauge bosons are massless before electroweak symmetry breaking the initial fields carry only two degrees of freedom and massless spin-1/2 Weyl fermions can act as their superpartners. The names of these fermions are roughly formed by appending the suffix 'ino' to the end of the boson's name (gluon $\rightarrow$ *gluino*). As with the chiral supermultiplets the symbol is formed by adding a tilde ($g \rightarrow \tilde{g}$).

The Higgs field requires a modification to consistently include it in a SUSY theory. A naive implementation would place the Higgs into a chiral supermultiplet and generate fermion superpartners to the complex ϕ^0 and ϕ^+ fields. However, these new fermion fields would cause a *gauge anomaly*, where a loop diagram breaks the gauge symmetry. A sufficient condition to avoid this anomaly is that the sum over the hypercharges of all fermions in the theory is 0 [6]. This means that it is possible to successfully cancel the anomaly by introducing a second Higgs doublet with hypercharge $Y = -1$. In this theory the two separate Higgs doublets (H_u^+, H_u^0) and (H_d^0, H_d^-) give rise to the masses of the up-type and down-type quarks respectively. These complex Higgs scalars are accompanied by fermion superpartners $(\tilde{H}_u^+, \tilde{H}_u^0)$ and $(\tilde{H}_d^0, \tilde{H}_d^-)$ called Higgsinos. During electroweak symmetry breaking both neutral Higgs fields acquire vacuum expectation values which satisfy $v_u^2 + v_d^2 = v^2$. The ratio of these VEVs is denoted $\tan\beta = v_u/v_d$.

Spin	0	1/2	1
Chiral supermultiplets			
squarks, quarks	$(\tilde{u}_L, \tilde{d}_L)$	(u_L, d_L)	
	$\tilde{u_R}$	u_R	
	$\tilde{d_R}$	d_R	
sleptons, leptons	$(\tilde{\nu}, \tilde{\ell}_L)$	(ν, ℓ_L)	
	$\tilde{\ell_R}$	ℓ_R	
Higgs, Higgsinos	(H_u^+, H_u^0)	$(\tilde{H}_u^+, \tilde{H}_u^0)$	
	(H_d^0, H_d^-)	$(\tilde{H}_d^0, \tilde{H}_d^-)$	
Gauge supermultiplets			
gluino, gluon		$\tilde{g}$	g
Wino, W		$\tilde{W}^{\pm}, \tilde{W}^0$	$W^{\pm}, W^0$
Bino, B		$\tilde{B}^0$	B^0

Table 2.4: The particle content of N = 1 SUSY before electroweak symmetry breaking.

This gives the full particle content of $N = 1$ SUSY before electroweak symmetry breaking in table 2.4. After electroweak symmetry breaking 3 of the Higgs degrees of freedom are absorbed into the electroweak bosons as before. The remaining 5 degrees of freedom form fields: 2 scalars called h^0 and H^0, 1 pseudoscalar A^0 and two charged scalars $H^{\pm}$. The lighter scalar field h^0 is identified with the Standard Model Higgs h. The electroweak gauginos can also mix after electroweak symmetry breaking, forming combinations collectively referred to as *charginos* ($\tilde{\chi}_i^{\pm}$) and *neutralinos* ($\tilde{\chi}_i^0$). The mass eigenstates of the sfermions can also mix where there are no conserved quantum numbers to separate them. Most possible mixings would disagree with experimental constraints on flavour changing neutral currents or kaon mixing [53]. However a relatively large mixing $(\tilde{f}_L, \tilde{f}_R) \rightarrow (\tilde{f}_1, \tilde{f}_2)$ cannot yet be ruled out for the third generation objects (t, b and τ).

2.3.3 SUSY breaking

If supersymmetry were a perfect symmetry then we would expect the superpartners to have exactly the same masses as their Standard Model partners. That is, we could quite reasonably have expected to have observed many of the superpartners by now. This implies that some extra physics exists that serves to break the symmetry, boosting the masses of the superpartners to higher mass scales. However, even if one avoids terms that reintroduce the quadratic divergences in equation 2.5 this reintroduces divergences in the Higgs mass corrections that scale approximately as

$$\delta m_h^2 \propto m_{\mathrm{soft}}^2 \left[\ln \frac{\Lambda_{\mathrm{UV}}}{m_{\mathrm{soft}}} + ... \right]$$

where m_{soft} is a new mass scale introduce by the breaking of supersymmetry (analogous to the electroweak scale introduce by electroweak symmetry breaking). This scale describes the mass splittings between the Standard Model particles and their superpartners, implying that the superpartners cannot be 'too' much heavier without imperilling the solution to the hierarchy problem. Most estimates place the acceptable range somewhere on the TeV scale, well in reach of the LHC, though this is a somewhat vague restriction. This mass scale is also similar to the one required to unify the gauge couplings and form a GUT [54–58].

Numerous such possibilities for supersymmetry breaking exist and some are described in references [59–64].

2.3.4 R-parity

In a general SUSY Lagrangian there is nothing to prevent the appearance of terms that violate lepton and baryon number conservation. However such terms could easily lead to the emergence of proton decay through the decay $p \to e^+\pi^0$ and strict experimental limits have been set on this process with a lower bound on the proton lifetime of 10^{34} years [65]. To avoid this an extra symmetry can be imposed on the Lagrangian with a corresponding multiplicative quantum number R-parity [66] given by

$$P_R = (-1)^{3(B-L)+2s}$$

where B, L, and s are baryon number, lepton number and spin respectively. This choice is not entirely without motivation and can be shown to arise quite naturally from breaking higher dimensional symmetry groups found in some grand unified theories [67, 68].

Standard Model particles have $P_R = +1$ and SUSY particles $P_R = -1$. The upshot of this is that any SUSY particle must decay into a state containing a lighter SUSY particle and therefore the lightest supersymmetric particle (LSP) must be stable.

In order for this LSP to not have been observed it cannot carry strong or electric charge, meaning it must be one of the neutralinos, $\tilde{\chi}_1^0$ or a sneutrino $\tilde{\nu}$[7]. This is striking as so long as m_{LSP} falls within reasonable bounds this is exactly the same requirement that was placed on a dark matter candidate in section 2.2.6 [69, 70]. However, in order for the $\tilde{\nu}$ to be compatible with current measurements of dark matter, large amounts of lepton-number violation would also be necessary [71].

However R-parity conservation is not a given within SUSY and R-parity violating (RPV) SUSY models exist, with strict constraints on combinations of couplings that could result in proton decay, resulting in a very long proton lifetime. It is also possible to have RPV terms and no proton decay so long as only *one* of lepton and baryon number conservation is violated.

2.3.5 Theoretical SUSY frameworks

It is possible to write a fairly general low energy effective Lagrangian which does not depend on the breaking mechanism. This is called the minimal supersymmetric Standard Model (MSSM) [72, 73]. The MSSM considers all possible SUSY breaking terms which do not reintroduce the quadratic divergences in the Higgs mass and which keep the theory renormalisable. These terms are

- mass terms for the sfermions,
- mass terms for the gauginos,
- trilinear scalar couplings,
- bilinear scalar couplings.

Of these last two, only a few possible couplings retain Standard Model gauge invariance: the trilinear couplings relating the sfermion and Higgs fields and the bilinear coupling relating the two Higgs fields [7]. However, when combined with

[7]It could alternatively be the gravitino, the spin-3/2 partner to the graviton.

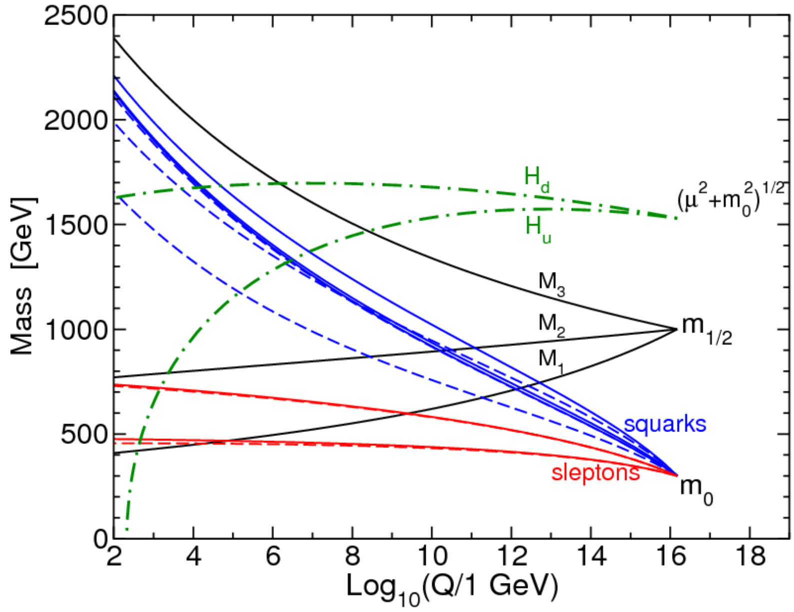

Figure 2.7: The running of the MSSM breaking parameters is shown, with MSUGRA boundary conditions imposed at $Q_0 = 1.5 \times 10^{16}$GeV. The parameter $\mu^2 + m^2_{H_u}$ runs negative, generating electroweak symmetry breaking. Figure taken from reference [6].

all possible terms from unbroken SUSY this results in over 100 free parameters and no longer serves well as a predictive theory.

It is possible to create theories with far fewer free parameters. For example the mSUGRA boundary condition requires that the soft breaking terms should unify at the same scale as the gauge couplings (figure 2.7), greatly reducing the number of free parameters in the theory [74–76].

Another option is to make certain restrictions to the MSSM based on well understood experimental results. These restrictions are [77, 78]

- no additional sources of CP violation,
- no tree-level flavour changing neutral currents[8],
- universality of the first and second generation fermions SUSY breaking parameters,
- the LSP is the lightest neutralino.

[8]These could be generated by non-diagonal sfermion mass matrices for example.

These reduce the number of free parameters down to a more manageable 19 which are summarised in table 2 of reference [79]. This model is referred to as the phenomenological minimal supersymmetric Standard Model (pMSSM).

Frequently the results of direct searches are interpreted in the context of *simplified models* [80–82]. In these only a few SUSY particles are considered as having kinematically accessible masses and many of the decay branching ratios are fixed. While the full predictions of these theories would be excluded by many experimental results, they can approximate the results of large areas of viable parameter space and ease comparisons between many different analyses.

2.3.5.1 SUSY phenomenology

The SUSY and gauge symmetry generators commute, meaning that the gauge couplings between SUSY and Standard Model particles are the same as the corresponding Standard Model couplings. For instance, the coupling strength for a $\tilde{g}\tilde{q}q$ vertex depends on α_s in the same manner as a gqq vertex. For R-parity conserving (RPC) SUSY lepton and baryon number violating couplings are removed so all vertices must respect conservation of these quantum numbers. RPC also implies all vertices must feature an even number of superpartner lines, some of the consequences of which have already been discussed in section 2.3.4.

For most SUSY theories the leading LHC production cross-sections are expected to come from the production of the strongly charged superpartners: the squarks and the gluinos (figure 2.8). This is due to the fact that the strong coupling is the largest of the gauge couplings. The production cross-sections decrease with the mass of the produced particles, but naturalness arguments [83, 84] suggest a mass for the $\tilde{t}$ around the TeV scale, suggesting that this should be within the reach of the LHC.

2.4 Summary

The theory of the Standard Model has been presented and many of its predictions have been discussed. Some of the limitations of this model have also been introduced. SUSY, a beyond the standard model (BSM) theory has been introduced as a possible

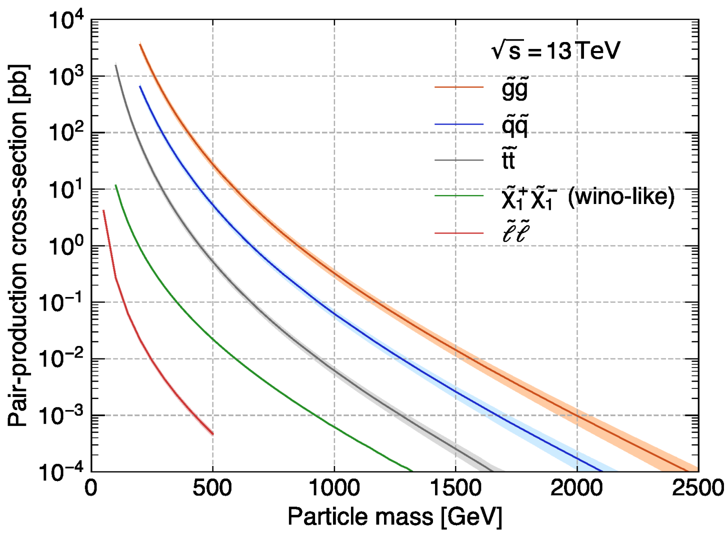

Figure 2.8: Cross-sections for several SUSY production process taken from reference [85]. The gluon cross-section assumes that all quarks are decoupled. The squark cross-section assumes that the gluino and stop are decoupled, leaving all other squarks degenerate in mass. The stop/sbottom cross-section assumes that the gluino and first and second generation quarks are decoupled. The cross-sections were calculated using reference [86].

resolution to many of these problems. Many separate arguments indicate that a SUSY theory with particle masses at the TeV scale is well motivated, and many such theories should be within reach of the LHC.

3

The ATLAS Detector

Contents

3.1 Introduction

The ATLAS detector (A Toroidal LHC ApparatuS) [87] is one of 4 major experiments on the Large Hadron Collider (LHC) [88] ring built underneath the border between France and Switzerland near Geneva. The name is shared by the detector used to collect all of the data used in this thesis and the collaboration of over 3000 scientists who operate the detector and analyse the data which it produces. This chapter first describes the LHC then the ATLAS detector and its subdetectors as well as the algorithms used to convert the raw detector data into a form usable by analysers.

3.2 The Large Hadron Collider

The Large Hadron Collider (LHC) is the most complex scientific experiment and largest machine ever built. It accelerates two counter-rotating proton beams before colliding them at 4 separate interaction points situated around the ring where the 4 detectors are located. In clockwise order around the ring the detectors are ATLAS, A Large Ion Collider Experiment (ALICE) [89], the Compact Muon Solenoid (CMS) [90] and the LHC-beauty experiment (LHCb) [91]. This ring layout is shown in figure 3.1. The ring is approximately circular, consisting of 8 straight sections connected by curved sections and was built in the tunnel which previously contained the Large Electron Positron Collider (LEP) with a total circumference of 27km.

The performance of the collider can be described in terms of its luminosity L, defined as the ratio between the cross section of a process and the expected rate at which events from that process would be expected to be generated in LHC collisions.

$$\frac{dN_{\text{process}}}{dt} = L\sigma_{\text{process}}$$

The luminosity can be calculated from beam parameters to be [93]

$$L = \frac{N_b^2 n_b f}{2\pi\Sigma_x\Sigma_y} F,$$

where N_b is the number of protons per bunch, n_b is the number of bunches in the beam, f is the revolution frequency of the beam, Σ_x and Σ_y describe the overlap

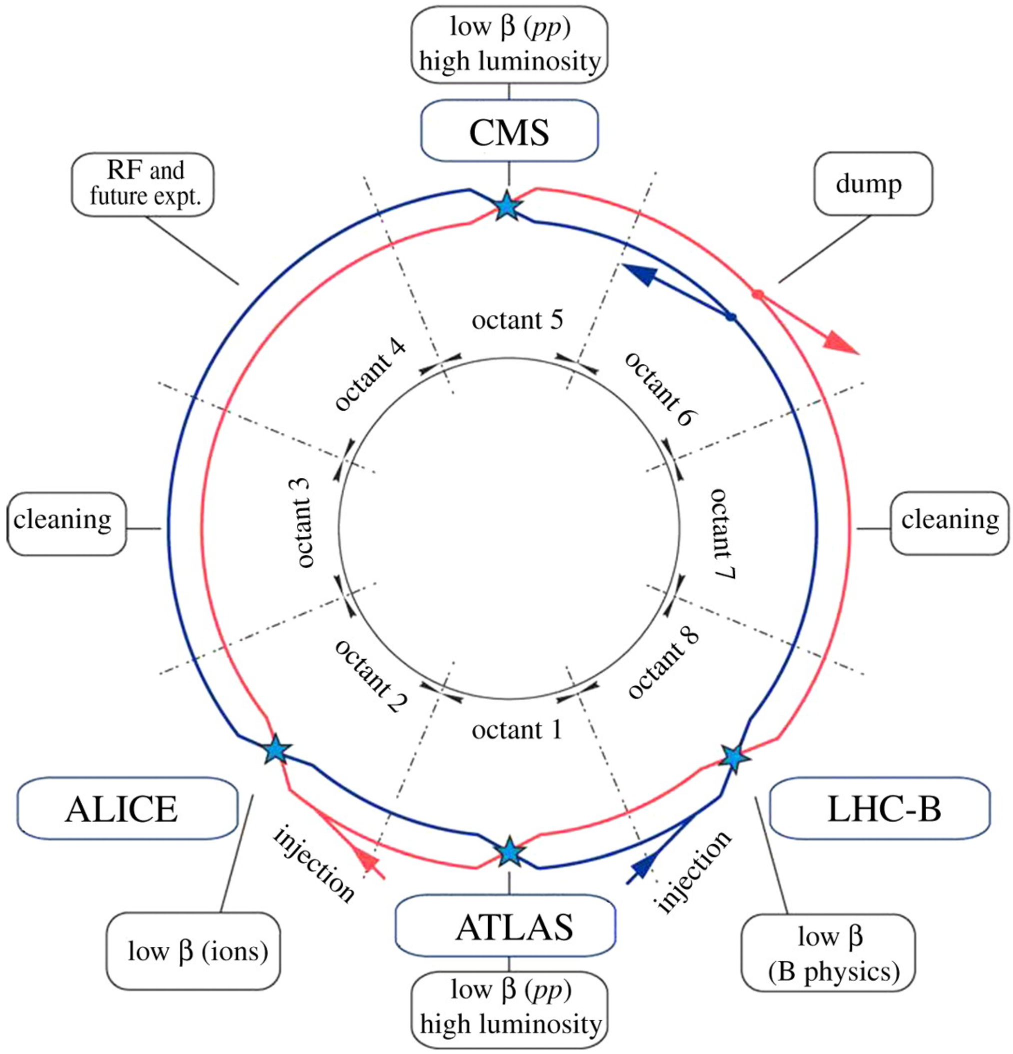

Figure 3.1: Graphic from reference [92] showing the positions of each of the experiments situated on the LHC ring.

of the two beams and F is a factor that describes the reduction in luminosity due to an angle between the colliding beams.

The LHC first achieved stable, colliding beams with energies of 3.5 TeV on the 30$^{\text{th}}$ March 2010 [92]. This marked the beginning of the first phase of LHC operations called Run 1, which ended on the 14$^{\text{th}}$ February 2013. During this time the beam energy was increased to 4 TeV from the beginning of physics running in 2012.

After a shutdown period covering 2 years the collider restarted operations, delivering beams with the higher energy of 6.5 TeV for Run 2. During this time, the peak luminosity of the collider was increased to $2 \times 10^{34}\text{cm}^{-2}\text{s}^{-1}$, twice the design luminosity. This period of running is projected to continue until the end of 2018 when the collider will enter another shutdown period, preparing for Run 3.

The protons used in the LHC beams are produced by ionising hydrogen, producing a plasma. The protons are extracted and then passed through several intermediary accelerators to gradually increase their energies before being inserted into the LHC as two beams with energies of 450 GeV. Note that the beams are not continuous but instead are arranged in trains of bunches. The beams are accelerated until they reach the collision energy of 6.5 TeV and are then allowed to collide at each of the interaction points. These beams continue to be rotated around the ring until containment is lost and the beams are 'dumped' by directing them into the beam dump system. This whole process from injection to dump is called a 'run'.

3.2.1 Pile-up

As shown in figure 3.2 the total cross-section at the LHC is several orders of magnitude higher than the cross-sections for 'interesting' processes. Therefore in order to get an appreciable rate for these interesting processes it is necessary to run with a high bunch luminosity $L_b = {}^{L}/_{n_b}$. We therefore expect to observe a number of interactions per crossing

$$\langle \mu \rangle = \frac{L_b \sigma_{\text{inel}}}{f} \,.$$

Therefore alongside any 'interesting' interaction in any bunch-crossing, we expect to see a number of extra soft QCD interactions. We call these extra interactions 'pile-up'. They tend to have a negative effect on detector performance by contributing to backgrounds. Many of the detector components have long signal pulse shapes [95] so are also sensitive to the impact of pile-up in adjacent bunch crossings. These two effects are often termed 'in-time' and 'out-of-time' pileup.

3.3 The ATLAS detector

The ATLAS detector is a large cylinder centered around the interaction point in segment 1 of the LHC. It is 44m long, 25m high and weighs approximately 7000 tonnes, making it the largest of the LHC detectors. It is designed as a general

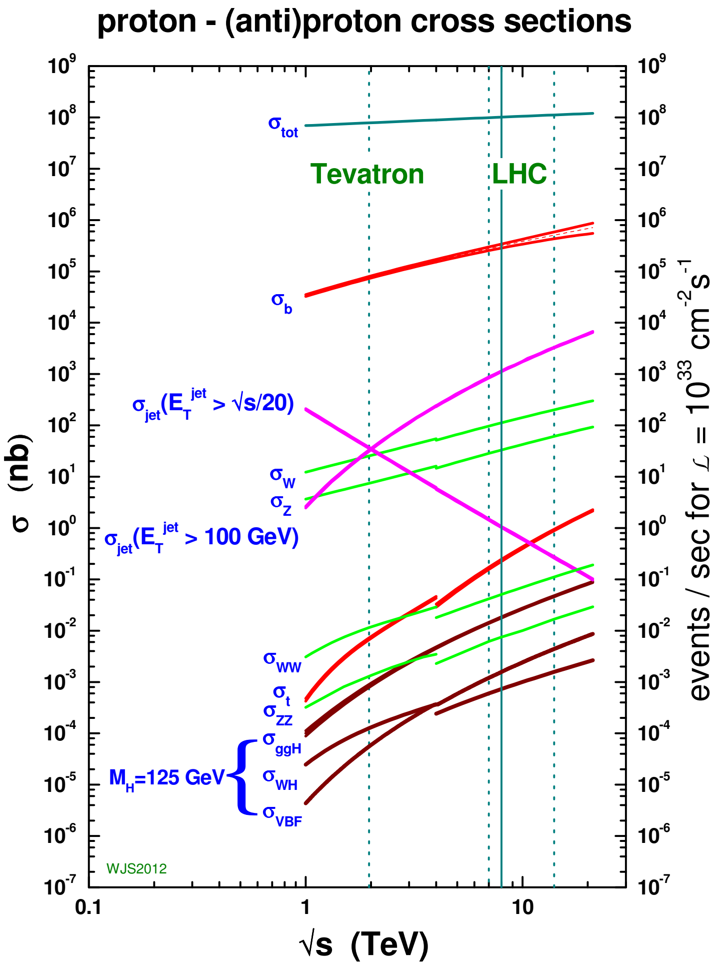

Figure 3.2: The predicted cross-sections for several processes as a function of center of mass energy. A discontinuity is shown at $\sqrt{s} = 4\,\text{TeV}$ where the initial state changes from proton anti-proton collisions to proton proton collisions. σ_{tot} is the total cross-section; the sum of the total elastic and inelastic cross-sections. Image taken from reference [94].

purpose detector, intended to have sensitivity to a wide number of processes both within the standard model and beyond it. Its hermetic design also means that the presence of particles which cannot be directly detected can be inferred (section 3.5.3).

3.3.1 ATLAS coordinate system

ATLAS uses a right-handed coordinate system with its origin at the nominal interaction point in the centre of the detector. The z-axis points down the beam pipe, the x-axis points from the origin to the centre of the LHC ring and the

y-axis points directly upwards towards the surface. The $x - y$ plane is called the transverse plane and is often parameterised by the circular coordinates (r, ϕ) with $\phi = 0$ corresponding to the x-axis. In most cases instead of θ, the angle to the beam axis, a quantity called pseudorapidity is used. Pseudorapidity (η) is defined as $\eta = -\ln\tan(\theta/2)$. This is the same as the rapidity

$$y = \frac{1}{2}\ln\frac{E + p_z}{E - p_z}$$

in the relativistic limit. The rapidity y has the convenient property that the rapidity difference between two particles remains invariant under boosts along the beam axis. In LHC collisions the composite nature of the colliding protons means that the centre-of-mass frame of the collision is rarely the same as the rest frame of the detector so this is a useful property to have. This also motivates the use of transverse quantities such as p_{T}, the momentum in the transverse plane.

3.3.2 Detector layout

ATLAS is divided into three main sections: the barrel which consists of concentric cylindrical sections centred around the beam axis, the endcaps which are the circular faces of the cylinder and the forward regions which lie closest to the beam pipe. In order to provide measurements of particle charges and improve the precision of measurements of particle momenta ATLAS is placed within a high magnetic field. This field is provided by 4 separate superconducting magnet systems: a large central solenoid positioned around the inner detector and 3 toroidal systems. The toroids are arranged into 3 groups of 8 magnets: one in the barrel region around the solenoid and one in each of the endcap regions. Figure 3.3 shows a schematic of this design. The solenoid provides a field of 2T along the beam axis and the barrel and endcap toroids provide toroidal fields of 1T and 0.5T respectively.

The main body of the detector consists of three components. The inner detector (ID) is positioned inside the solenoid and provides precision measurements of tracks and vertices from charged particles which pass through it. The calorimeters sit around the solenoid and inside the toroids and provide measurements of the energy

Detector component	**Target resolution**
Inner detector	$\sigma_{p_\mathrm{T}}/p_\mathrm{T} = 0.05\% p_\mathrm{T} \oplus 1\%$
EM calorimeter	$\sigma_E/E = 10\%/\sqrt{E} \oplus 0.7\%$
Hadronic calorimeter	
barrel and end-cap	$\sigma_E/E = 50\%/\sqrt{E} \oplus 3\%$
forward	$\sigma_E/E = 100\%/\sqrt{E} \oplus 10\%$
Muon spectrometer	$\sigma_{p_\mathrm{T}}/p_\mathrm{T} = 10\%$ at $p_\mathrm{T} = 1\,\mathrm{TeV}$

Table 3.1: The targeted energy and momentum resolutions of the detector subsystems taken from reference [87]. The units for E and p_T are in GeV.

and positions of electrons, photons, taus and hadrons. The muon spectrometer surrounds the whole detector and is used for the detection of muons. Additional detectors LUCID, ZDC and ALFA are positioned in the very forward direction further away from the interaction point. After Run 1 an additional luminosity detector called the Diamond Beam Monitor (DBM) was installed close to the beam pipe approximately 1 m away from the interaction point on either side. These are mainly used for luminosity measurements and detecting very forward particles and are discussed further in section 3.3.4. Figure 3.4 shows a cut-away view of the whole detector, highlighting the positions of the various components.

The targeted resolutions of the detector subsystems are shown in table 3.1. Commissioning tests using test beams, single beams and measurements of cosmic muons were used to demonstrate that these targets are approximately met by the detector [96–98]. Further details of these parameters are given in the following sections.

3.3.3 Subdetectors

3.3.3.1 The inner detector

The inner detector is designed to provide high precision measurements of charged particle tracks (3.5.1.2) and vertices (3.5.1.3). It is made out of three distinct systems: the pixel detector, the Semiconductor Tracker (SCT) and the Transition Radiation Tracker (TRT). A view of the ID showing these three systems is shown in figure 3.5.

The pixel system is the closest part of ATLAS to the interaction point. It consists of 4 separate layers of silicon pixel detectors in the barrel region and 3 disks in each of the endcaps. The outer 3 layers are divided into modules with a

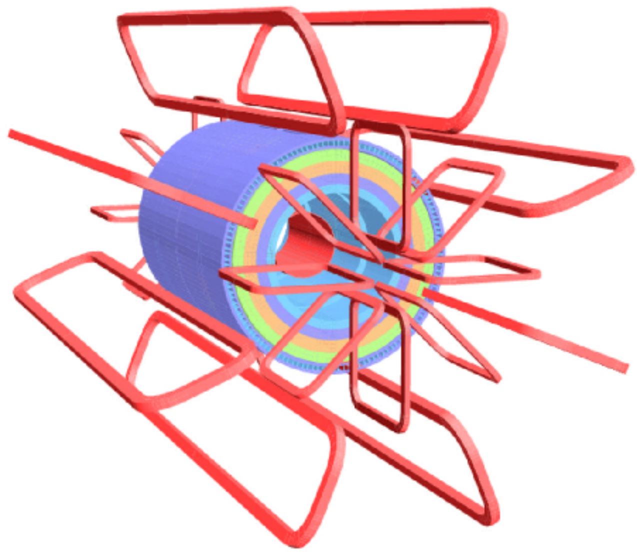

Figure 3.3: Schematic showing the geometry of the ATLAS magnet systems from reference [87]

cross-sectional area of $19 \times 63\text{mm}^2$ each made out of individual pixels, most with an area of $50{\times}400\,\mu\text{m}^2$ and a thickness of $250\,\mu\text{m}$. The innermost layer is called the Insertable B-Layer (IBL) and was added after Run 1 [99], attached directly to the beam pipe. It is formed from 14 staves, each containing 20 modules. It is designed to improve tracking performance by providing an extra measurement point, as well as mitigating the effects of radiation damage in the other layers. The system is designed so that any particle produced within $|\eta| < 2.5$ passes through 4 pixel layers.

The SCT system consists of 4 further layers in the barrel and 9 disks in each endcap, all formed of silicon strip detectors. Each module is double-sided and segmented: providing precise three dimensional space-points for use in track reconstruction. As with the pixel detectors, the SCT geometry is designed so that any particle produced within $|\eta| < 2.5$ passes through 4 SCT layers.

The silicon detectors in the pixel and SCT layers are all reversed bias $p - n$ diodes. The p-side of the detector is doped to have an excess of holes, the n-side to have an excess of electrons. The reverse bias voltage applied means that the cathode is connected to the n-type region and the anode to the p-type region. This causes these holes and electrons to be drawn away from the interface between the two, widening the depletion zone and meaning that little current flows. When a

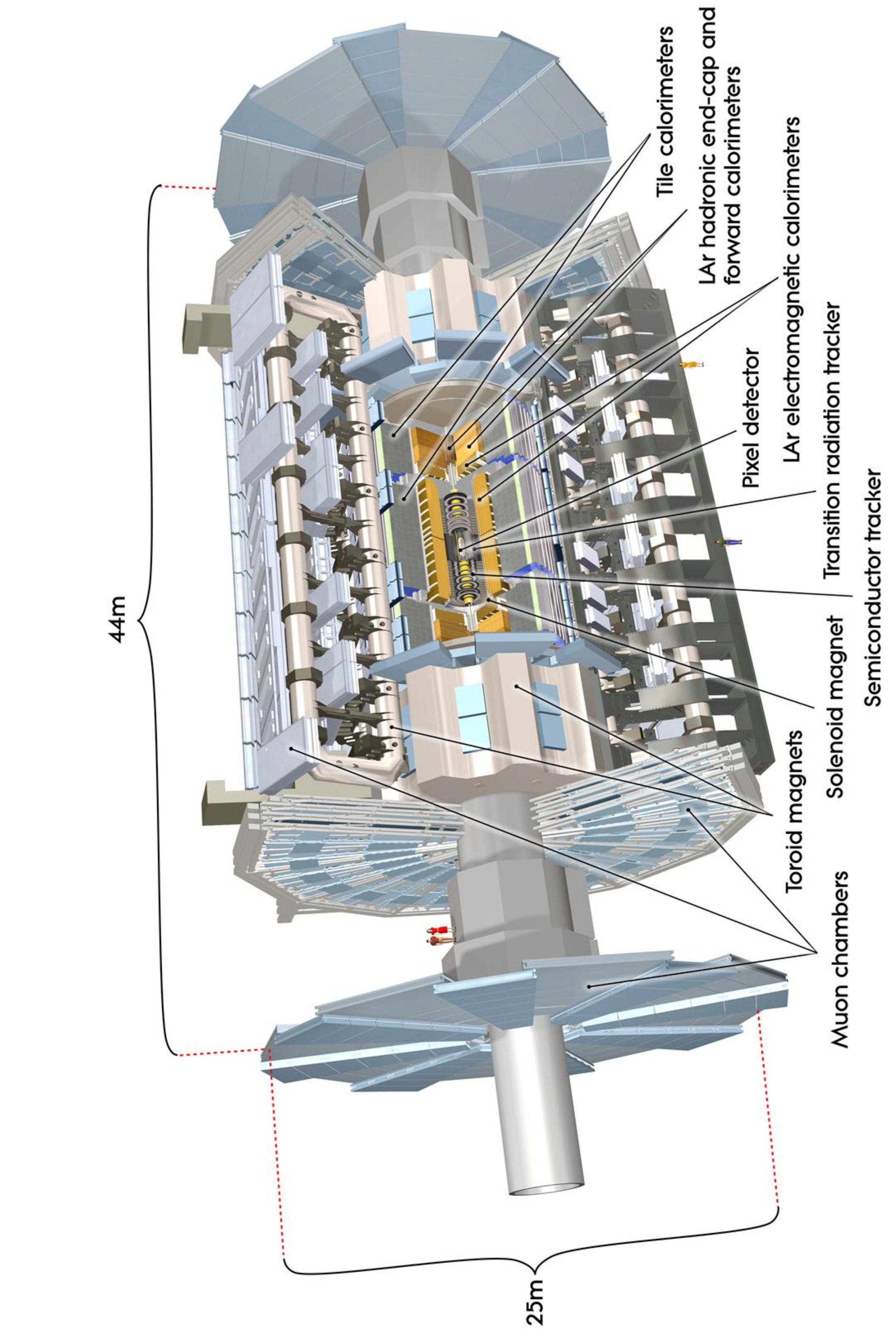

Figure 3.4: A cut-away view of the ATLAS detector from reference [87]

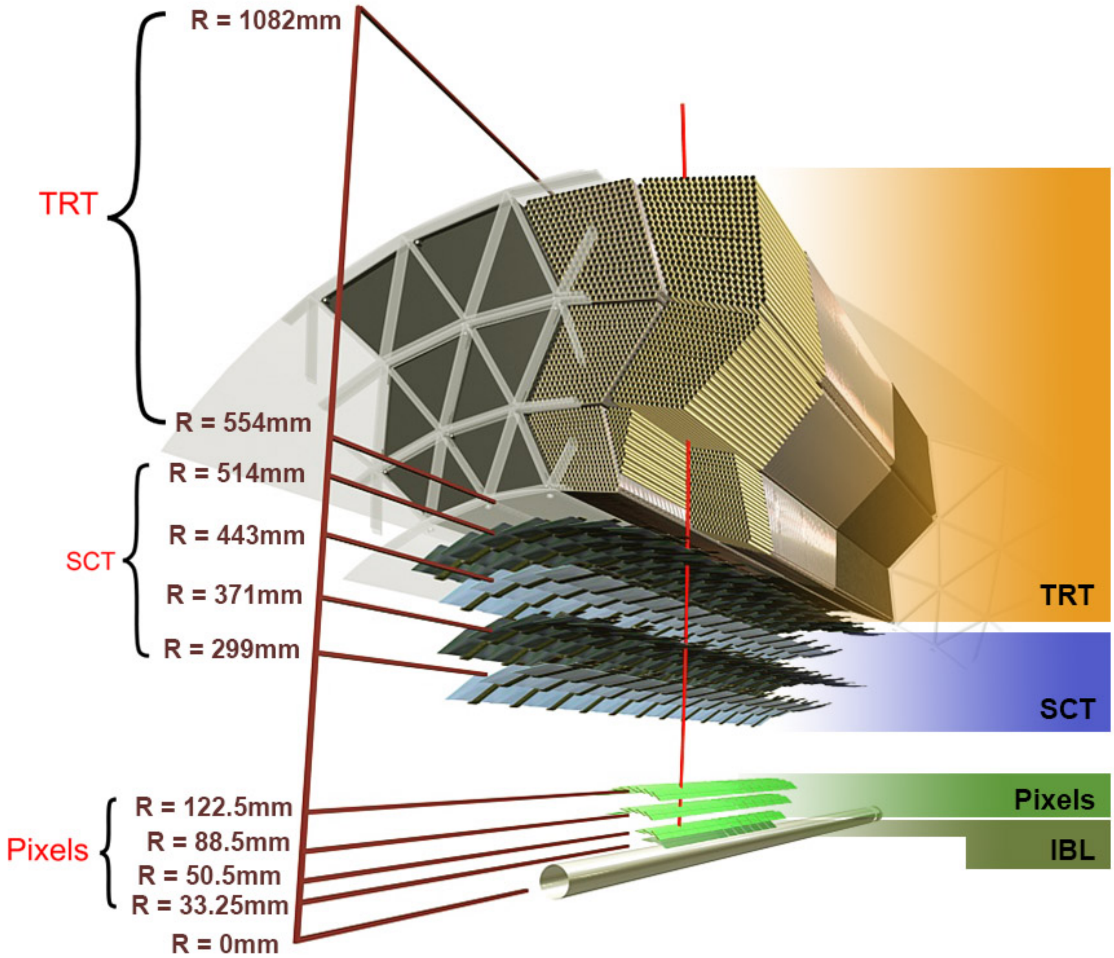

(a) Barrel

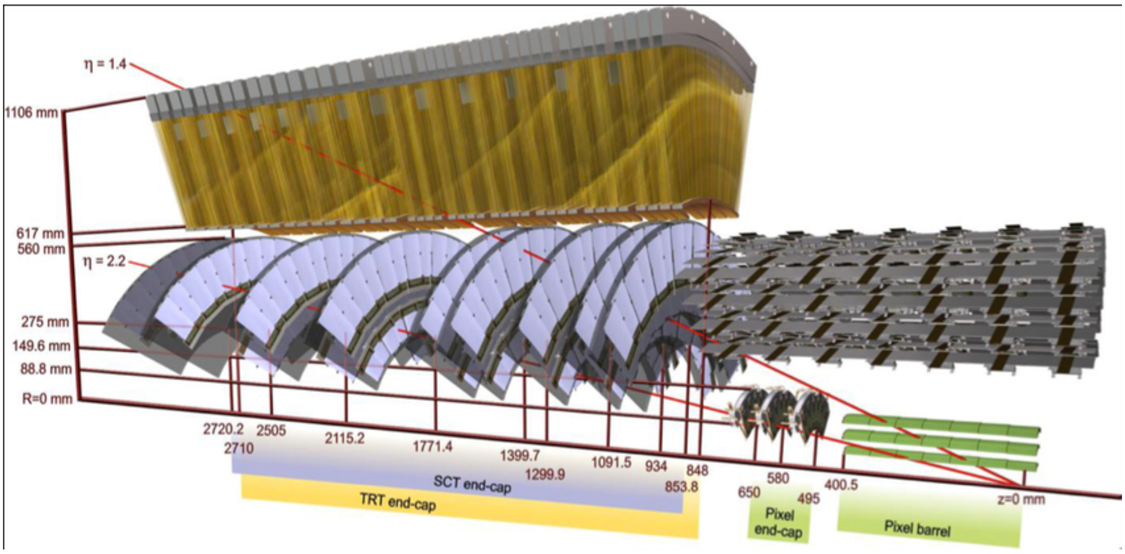

(b) Endcap

Figure 3.5: A graphic showing the ATLAS Inner Detector. The upper graphic (from reference [99]) shows the ID in the barrel region, the lower (from reference [87]) in the endcap region. The three different tracking detectors are shown including the 'Insertable B-Layer' which was added between Runs 1 and 2. Note that the lower graphic does not include the IBL.

charged particle passes through this zone, it excites electron-hole pairs which then drift to the electrodes, creating a current which can be measured.

The TRT forms most of the volume of the ID. It consists of 298 304 small 'straw tubes'. Each tube has a diameter of 4 mm coated with aluminium on the inside to act as a cathode and a 31 µm gold-plated tungsten anode. The tubes are filled with a $Xe/CF_4/CO_2$ gas mixture[1]. As a charged particle crosses the boundary between two media with different dielectric constants it produces soft X-rays in the direction of travel. These X-rays then ionise the gas mixture inside the tubes, causing electrons to be collected on the anode and a current to be measured. In order to maximise the amount of transition radiation produced the volume between the tubes is filled with polypropylene strips or fibres to increase the number of boundaries. The geometry of the TRT ensures that any particle within $|\eta| < 2.0$ will pass through at least 35 individual tubes.

Given that the band gaps in semiconductors and the ionisation energies of the gas mixture are typically measured in eV and the ID is designed to measure particles with energies upwards of 0.1 GeV these tracking detectors can be considered non destructive in that they do not greatly affect the particles they are measuring.

The detector performance was measured using data from cosmic rays [96]. The intrinsic efficiencies, defined as the probability of registering a hit when a charged particle passes through an operational detector element, are measured to be $99.974 \pm 0.004(\text{stat.}) \pm 0.003(\text{syst.})\%$ for the pixel detector and $99.78 \pm 0.01(\text{stat.}) \pm 0.01(\text{syst.})\%$ for the SCT. For tracks passing within 1mm of the wire the intrinsic efficiency of the TRT tubes is measured as $97.2 \pm 0.5\%$. The impact parameter resolutions for high-momentum tracks are measured as 22.1 ± 0.9µm for the transverse direction and 112 ± 4µm for the longitudinal direction. The inclusion of the IBL improved these resolutions by 40% for tracks with $p_{\mathrm{T}} < 1\,\mathrm{GeV}$ [100]. The asymptotic relative momentum resolution was measured to be $\sigma_{p_{\mathrm{T}}}/p_{\mathrm{T}} = (4.83 \pm 0.16) \times 10^{-4}\mathrm{GeV}^{-1} \times p_{\mathrm{T}}$.

[1]During Run 1 some of these straws were found to have leaks. Given that Xe is expensive it was replaced by Ar in these leaky channels. This only affects the electron ID efficiency, not the tracking.

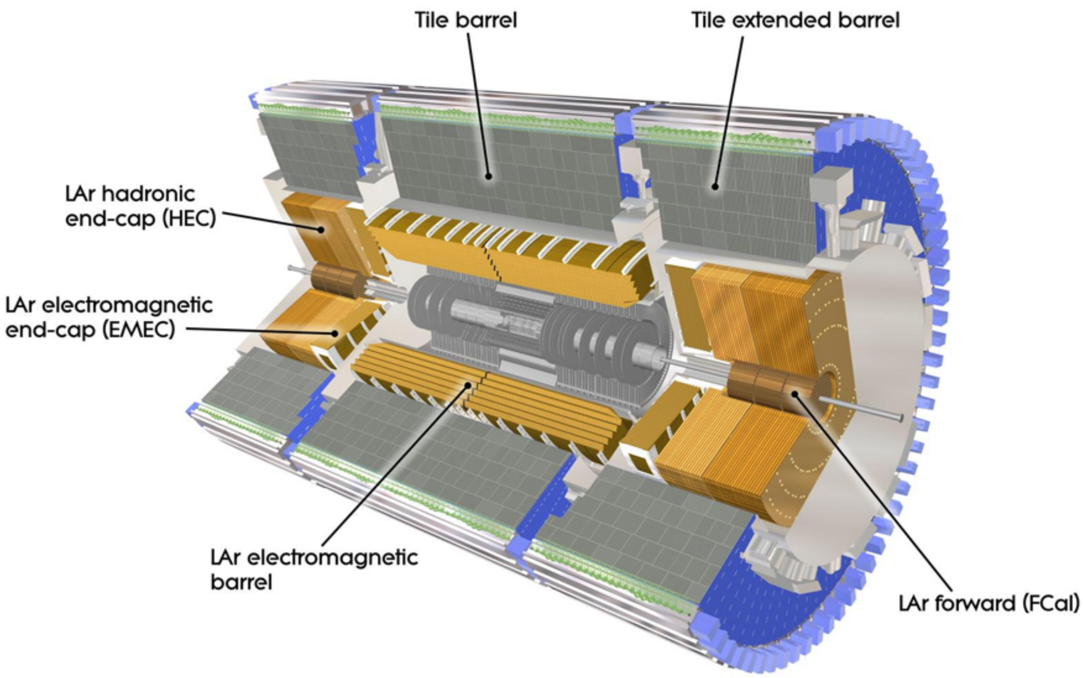

Figure 3.6: A cutaway view of the ATLAS calorimeters taken from reference [87]

3.3.3.2 Calorimeters

The calorimeters are designed to provide accurate measurements of particle energies with near-hermetic coverage. They are also designed to limit punch-through into the muon systems[2]. The ATLAS calorimeters are divided into two separate systems: the LAr and Tile calorimeters. A cutaway image of the ATLAS calorimeters is shown in figure 3.6.

Both ATLAS calorimeters are 'sampling calorimeters' [101], meaning that they consist of alternate layers of 'passive' and 'active' materials. The passive material is usually very dense and designed to provoke a lot of interactions between itself and the particle which passes through it. The choice of this material will vary depending on whether the calorimeter is designed to detect electromagnetic particles (e.g. electrons and photons) or hadronic particles. For electromagnetic calorimeters materials with high atomic number such as lead are appropriate, for hadronic

[2]Punch-through is when a hadronic jet is not fully absorbed by the calorimeters and therefore enters the muon systems, providing a background to measurements there.

calorimeters metallic absorbers are typically used. Particles passing through this region will interact, forming a shower of high energy particles.

This shower then enters the 'active' layer. This layer is made of a material that reacts to the particles passing through it. Examples include noble liquids that can become ionised causing a current to flow or a scintillating material which emits light which is then measured by a photodetector. By constructing alternating layers of these materials the shower can be measured and the energy of the original particle can be inferred from the number of particles produced in its shower. This showering process is Poisson distributed, meaning that the error $\sigma(N) \propto \sqrt{N}$, i.e. $\sigma(E) \propto \sqrt{E}$. The calorimeters absorb the particles which they are measuring, making them destructive detectors.

Calorimeter depth is typically described in terms of radiation length (X_0) for electromagnetic calorimeters and interaction length (λ_I) for hadronic calorimeters. The radiation length is defined as the distance over which a high energy electron's energy drops to $^1/_e$ of its original value due to Bremsstrahlung or equivalently $^7/_9$ of the mean free path for pair-production of a high energy photon. The nuclear interaction length is the mean free path for nuclear interaction of a high energy hadronic particle. Short distances are ideal for each of these as they decrease the amount of calorimeter material necessary to contain particle showers.

The thickness of the ATLAS calorimeters depends on the rapidity. The EM calorimeters are at least $22X_0$ in the barrel, increasing to at least $24X_0$ in the endcaps. The hadronic calorimeters provide 9.7λ in the barrel and 10λ in the endcaps. Including the outer support the total thickness at $\eta = 0$ is 11λ. This reduces the incidence of punch-through below the rate of production of muons from prompt sources and in-flight decays.

The LAr calorimeter is split into four pieces: the EM barrel, the EM endcap (EMEC), the hadronic endcap (HEC) and the forward calorimeter (FCal). All of these four pieces use liquid argon (LAr) as the active material.

The EM calorimeter (barrel and EMEC) uses lead slabs with stainless steel supports as the passive material. The calorimeter uses an accordion geometry to ensure a continuous ϕ coverage. Within the precision region $|\eta| < 2.5$ it has 3 layers with varying granularities typically around $\Delta\eta \times \Delta\phi = 0.025 \times 0.1$. In the more forward region $2.5 < |\eta| < 3.2$ this drops to 2 layers with a granularity of 0.1×0.1. The full granularities are summarised in table 3.2. The high granularity is necessary to distinguish between prompt photons and those produced through the process $\pi_0 \to \gamma\gamma$. An extra 'presampler' layer of active material is placed in the region $|\eta| < 1.8$ to recover some of the energy lost through interactions with the detector material upstream of the calorimeters. There is a calorimeter 'crack' between the barrel and endcap portions between $1.37 < |\eta| < 1.52$ which contains detector services. As the calorimeter performance is degraded and hard to model in this region it is usually excluded when reconstructing electrons.

The HEC uses copper plates as the passive material and has four layers with a granularity of 0.1×0.1 within $1.5 < |\eta| < 2.5$ rising to 0.2×0.2 up to an $|\eta|$ of 3.2. The FCal has 3 modules in each endcap. The first, using copper as the passive medium is optimised for EM measurements. The second two use tungsten as the passive medium and are optimised for hadronic measurements. The FCal is not segmented in the projective η-ϕ geometry but in Δx-Δy.

The Tile calorimeter uses steel as the passive medium and scintillating tiles as the active medium. It is formed of three layers; the first two have a granularity of 0.1×0.1 which rises to 0.2×0.1 in the final layer.

The calorimeter energy resolution can be parameterised as

$$\frac{\sigma(E)}{E} = \frac{a}{E} \oplus \frac{b}{\sqrt{E}} \oplus c,$$

where a, b and c are η-dependent parameters. The a term is the 'noise' term, describing effects which do not depend on energy such as electronic or pile-up noise. The b term is the 'stochastic' term, describing the effect of the Poisson process that takes place in the sampling calorimeters. The c term is the 'constant' term which includes effects such as energy lost in interactions with upstream detector material e.g. the cryostat or the solenoid.

The main parameters and measured resolutions are shown in table 3.2.

	Barrel		Endcap	
EM calorimeter				
Number of layers and $\|\eta\|$ coverage				
Presampler	1	$\|\eta\| < 1.52$	1	$1.5 < \|\eta\| < 1.8$
Calorimeter	3	$\|\eta\| < 1.35$	2	$1.375 < \|\eta\| < 1.5$
	2	$1.35 < \|\eta\| < 1.475$	3	$2.5 < \|\eta\| < 3.2$
			2	$2.5 < \|\eta\| < 3.2$
Granularity $\Delta\eta \times \Delta\phi$ versus $\|\eta\|$				
Presampler	0.025×0.1	$\|\eta\| < 1.52$	0.025×0.1	$1.5 < \|\eta\| < 1.8$
Calorimeter 1st layer	$0.025/8 \times 0.1$	$\|\eta\| < 1.40$	0.050×0.1	$1.375 < \|\eta\| < 1.425$
	0.025×0.025	$1.40 < \|\eta\| < 1.475$	0.025×0.1	$1.425 < \|\eta\| < 1.5$
			$0.025/8 \times 0.1$	$1.5 < \|\eta\| < 1.8$
			$0.025/6 \times 0.1$	$1.8 < \|\eta\| < 2.0$
			$0.025/4 \times 0.1$	$2.0 < \|\eta\| < 2.4$
			0.025×0.1	$2.4 < \|\eta\| < 2.5$
			0.1×0.1	$2.5 < \|\eta\| < 3.2$
Calorimeter 2nd layer	0.025×0.025	$\|\eta\| < 1.40$	0.050×0.025	$1.375 < \|\eta\| < 1.425$
	0.075×0.025	$1.40 < \|\eta\| < 1.475$	0.025×0.025	$1.425 < \|\eta\| < 2.5$
			0.1×0.1	$2.5 < \|\eta\| < 3.2$
Calorimeter 3rd layer	0.050×0.025	$\|\eta\| < 1.35$	0.050×0.025	$1.5 < \|\eta\| < 2.5$
Number of readout channels				
Presampler	7808		1536 (both sides)	
Calorimeter	101760		62208 (both sides)	
Measured resolution				
σ_E/E	$10.1 \pm 0.4\%/\sqrt{E} \oplus 0.2 \pm 0.2\%$		$(10$ - $12.5)\%/\sqrt{E} \oplus 0.6\%$	
LAr hadronic endcap (HEC)				
$\|\eta\|$ coverage			$1.5 < \|\eta\| < 3.2$	
Number of layers			4	
Granularity $\Delta\eta \times \Delta\phi$			0.1×0.1	$1.5 < \|\eta\| < 2.5$
			0.2×0.2	$2.5 < \|\eta\| < 3.2$
Readout channels			5632 (both sides)	
σ_E/E (electrons)			$21.4 \pm 0.1\%/\sqrt{E} \oplus 0$	
σ_E/E (pions)			$70.6 \pm 1.5\%/\sqrt{E} \oplus 5.8 \pm 0.2\%$	
LAr forward calorimeter (FCal)				
$\|\eta\|$ coverage			$3.1 < \|\eta\| < 4.9$	
Number of layers			3	
Granularity $\Delta x \times \Delta y$ (cm)			FCal1: 3.0×2.6	$3.15 < \|\eta\| < 4.30$
			FCal1: four times finer	$3.10 < \|\eta\| < 3.15$, $4.30 < \|\eta\| < 4.83$
			FCal2: 3.3×4.2	$3.24 < \|\eta\| < 4.50$
			FCal2: four times finer	$3.20 < \|\eta\| < 3.24$, $4.50 < \|\eta\| < 4.81$
			FCal3: 5.4×4.7	$3.32 < \|\eta\| < 4.60$
			FCal3: four times finer	$3.29 < \|\eta\| < 3.32$, $4.60 < \|\eta\| < 4.75$
Readout channels			3524 (both sides)	
σ_E/E (electrons)			$28.5 \pm 1.0\%/\sqrt{E} \oplus 3.5 \pm 0.1\%$	
σ_E/E (pions)			$70\%/\sqrt{E} \oplus 3.0\%$	
Tile calorimeter				
	Barrel		Extended barrel	
$\|\eta\|$ coverage	$\|\eta\| < 1.0$		$0.8 < \|\eta\| < 1.7$	
Number of layers	3		3	
Granularity $\Delta\eta \times \Delta\phi$	0.1×0.1		0.1×0.1	
Last layer	0.2×0.1		0.2×0.1	
Readout channels	5760		4092 (both sides)	
σ_E/E (pions)			$1.6 \pm 0.1\%/E \oplus 21.0 \pm 1.0\%/\sqrt{E} \oplus 3.0 \pm 0.1\%$	

Table 3.2: The main parameters of the ATLAS calorimeter system, modified from table 1.3 in [87]. Measurements of resolution are provided assuming E is measured in GeV, where a term is not included it is because it is negligible.. The range of measurements shown for the EM endcap calorimeter allow for changes across the full η range and come from [102]. The measurement of the tile calorimeter is shown as measured in a setup where they were combined with LAr barrel calorimeter modules.

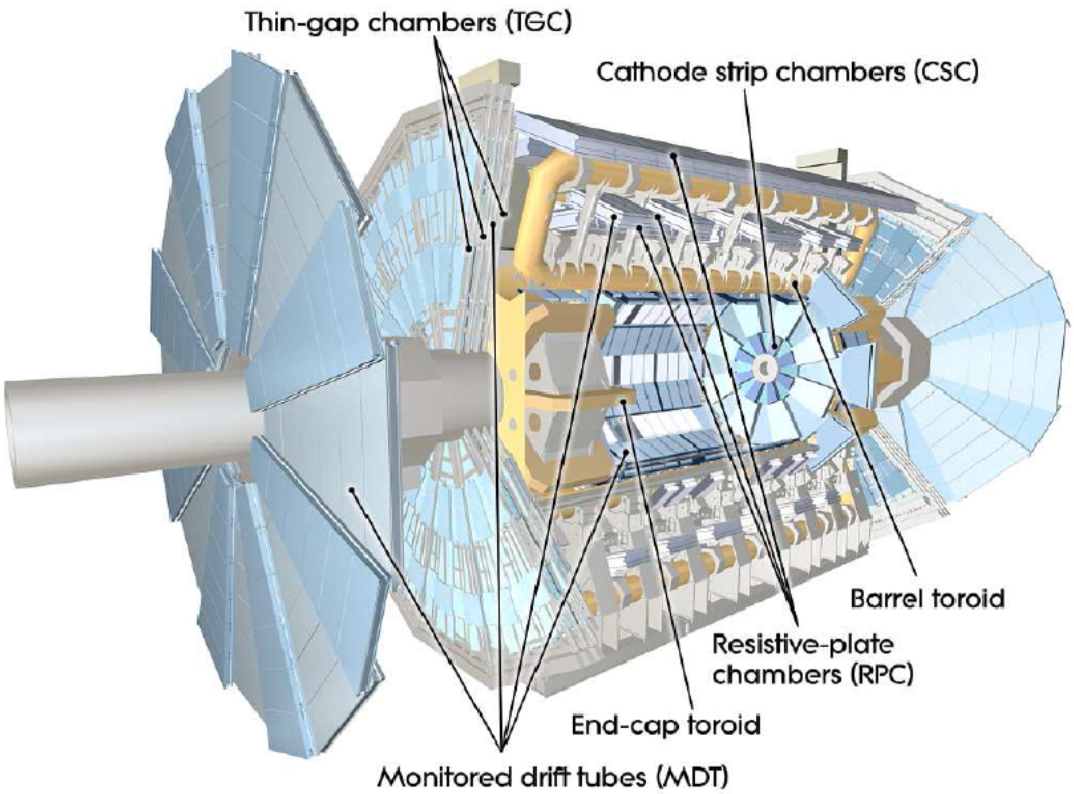

Figure 3.7: A cutaway view of the ATLAS muon spectrometer taken from reference [87].

3.3.3.3 Muon spectrometer

The muon spectrometer is the outermost part of the detector. This is because muons pass through most of the detector interacting only minimally (see section 4.2.1.1). It covers the range $|\eta| < 2.7$ and sits in the, on average, 0.5T (1.0T) magnetic field generated by the toroidal magnets in the barrel (endcaps) which allows for a momentum measurement from the curvature of the measured tracks (section 3.5.1.2). It consists of four different detector technologies: monitored drift tubes (MDT) and cathode strip chambers (CSC) which are precise but have long readout times and resistive plate chambers (RPC) and thin gap chambers (TGC) which are less precise but have faster readout times suitable for triggering (section 3.4). Figure 3.7 shows a cutaway view of the muon spectrometer.

Most of the precision measurements come from the monitored drift tubes supplemented by the cathode strip chambers within the range $2.0 < |\eta| < 2.7$

which are able to deal with the larger particle flux in these areas. Monitored drift tubes contain a pressurised Ar/CO_2 gas mixture surrounding a central wire. When a high energy muon passes through this gas mixture it causes ionisation, leading to a detectable current. The disadvantage of this technology is its long response time of up to 700 ns which corresponds to the maximum drift time from the wall of the chamber to the wire. Due to this long response time it is necessary to impose dead time on the detector readout system after the first detection of charge. The tubes are directed along the ϕ direction and though the numbers of tubes per layer and segmentation vary across the detector a typical muon will cross 20 tubes as it passes through the detector. For $|\eta| < 2.0$, 3 layers of MDTs are present, decreasing to 2 in the range $2.0 < |\eta| < 2.7$.

The cathode strip chambers are multiwire proportional chambers providing additional coverage in the range $2.0 < |\eta| < 2.7$. Each chamber holds 4 planes of wires positioned perpendicularly to each other which act as anodes. The cathodes are segmented into strips, allowing the measurement of position information. The chambers are filled by an Ar/CO_2 gas mixture. The signal is provided by measuring the *relative* induced charges on adjacent strips, protecting against effects from changes in the conditions of a particular muon chamber.

The resistive plate chambers consist of two opposite charged plates held at a distance of 2 mm filled with a $C_2H_2F_4$/Iso-C_4H_{10}/SF_6 gas mixture. A muon passing through causes avalanches of electrons which get drawn to the anode and give rise to a signal. The RPCs are installed in 3 layers with two sets of chambers in each layer. There are two close together inner layers and one outer layer which is further away. The large lever arm between the inner and outer layers provides a high $(9-35\text{GeV})$ p_T trigger. The low $(3-9\text{GeV})$ p_T trigger is measured using the inner layers. RPCs are used in the barrel region. Between Run 1 and Run 2 a fourth layer of RPCs were brought online to cover holes in trigger acceptance.

The thin gap chambers are used to provide triggering in the endcap regions as well as a second azimuthal coordinate to complement the MTDs. They are similar to the CSCs in that they are multiwire proportional chambers. However they are characterised by the fact that the distance between two wires is larger than the distance between the cathode strips and the wires. The short distance between the strips and the wires gives a shorter read-out time than the CSCs.

3.3.4 Luminosity measurement

ATLAS has multiple systems which can be used to measure the luminosity in the detector [93]. The LUminosity Cherenkov Integrating Detector (LUCID) consists of two sets of 20 photomultiplier tubes (PMT) positioned 17 m away from the interaction point in both directions. As particles enter the quartz windows of the PMTs they produce Cherenkov radiation which is measured by the PMTs. If the energy measured in the PMT exceeds a threshold then that is recorded as a 'hit'. The number of hits is proportional to the luminosity. Alternatively the total integrated PMT charge can also be used.

The Diamond Beam Monitor supplements the older Beam Condition Monitor and provides an extra method to measure bunch-by-bunch luminosities. Both systems contain multiple diamond pixel detectors positioned either side of the interaction point close to the beam pipe. The DBM is at $z = \pm 1$ m and the BCM at $z = \pm 1.74$ m. As with LUCID when a signal is measured above threshold it is recorded as a 'hit'.

Both of these methods need to be calibrated. For this purpose periodic Van de Meer scans [103] are used, where the beams are moved in the transverse direction relative to each other, artificially reducing the interaction cross-section of the beams.

In order to reduce the impact of statistical uncertainties in the instantaneous luminosity measurement the luminosity is measured and then averaged over a 'luminosity block', a period of time usually lasting around one minute.

3.4 Trigger

The storage size of ATLAS datasets is approximately 1.3 MB per event. At an input LHC collision rate of 40 MHz this would correspond to a total output rate of over 50 TB/s which would quickly overwhelm ATLAS's data storage capabilities. Additionally as shown in figure 3.2 the cross-sections for 'interesting' physics processes are orders of magnitude lower than the total proton-proton cross-section so the majority of the recorded data would be soft-QCD which is not a target of the ATLAS physics program.. Beyond this there is a hard limit O(100 kHz) on the maximum read-out rate of many of the detector subcomponents. Therefore it is necessary to limit the number of bunch-crossings which the detector reads out. This is controlled by the ATLAS trigger system [3].

The ATLAS trigger is separated into two separate systems: the hardware based Level 1 (L1) trigger and the software based High Level Trigger (HLT). The L1 trigger receives the full 40 MHz input rate and reduces it to an output rate of 100 kHz limited primarily by the read-out of the individual detector components. The HLT trigger is run on the output of the L1 trigger and further reduces the output rate to a more manageable rate of approximately 1 kHz. Dedicated trigger strategies are designed for each type of trigger signature: electrons, photons, muons, taus, jets and $E_{\mathrm{T}}^{\mathrm{miss}}$, with specialised triggers also designed to select events containing b-quarks.

3.4.1 L1

The L1 trigger is split into two main systems: the calorimeter trigger (L1Calo) [104] and the muon trigger. Signals from these two systems, as well as from several other systems such as the Minimum Bias Trigger Scintillators, LUCID and the Zero Degree Calorimeter (ZDC) are combined in the Central Trigger Processor (CTP) which is responsible for making the final L1 trigger decision. The CTP is also responsible for applying *dead-time*, preventing two L1 accepts from firing too soon after each other such that the detector read-outs would overlap. It also applies *complex* dead-time, restricting the number of L1 accepts allowed in a given period of time which prevents the front-end buffer system into the HLT from overflowing.

3.4.1.1 L1Calo

The L1 calorimeter trigger receives information from the whole calorimeter, divided into ‘trigger towers’. These towers combine the signals from wedges of the calorimeters cells in $\Delta\eta \times \Delta\phi$ blocks, considering the EM and hadronic calorimeters separately. In the barrel these towers measure 0.1×0.1 up to $|\eta| < 2.5$. For $2.5 < |\eta| < 3.1$ the towers measure 0.2×0.2 and between $3.1 < |\eta| < 3.2$ they measure 0.1×0.2. In the FCal the towers are not formed in the projective geometry. Instead each side of the FCal is divided into 64 towers.

The signals are passed through an FPGA preprocessor system responsible for digitising and calibrating the signals. This differs from the system in Run 1 in that it uses a dynamic bunch-by-bunch pedestal subtraction to correct for the impact of different conditions throughout each bunch train. Noise filters are also applied which mean that a tower's E_{T} is only considered if it falls above an η dependent threshold. These filters greatly reduce the impact of pile-up on the trigger rates.

Electron and photon candidates are formed using a sliding window algorithm using a 2×2 window. The energy sums in each of the four possible 1×2 or 2×1 rectangles are considered and compared to a chosen threshold. As well as this primary threshold two isolation thresholds are used. To reduce the background from hadronic activity the shower is required not to extend into the hadronic calorimeter by ensuring that the total E_{T} in the 2×2 hadronic trigger towers behind the chosen window is below a hadronic isolation threshold. Next, the sum over the measured E_{T} in the 12 EM trigger towers surrounding the window is required to be below an EM isolation threshold. These hadronic and isolation thresholds can be set differently depending on η to correct for differences in the detector response.

Tau candidates are formed similarly, however in this case the hadronic isolation is not considered. Instead the energy in 2×2 hadronic trigger towers behind the window is included in the sums in the EM calorimeter.

The jet/$E_{\mathrm{T}}^{\mathrm{miss}}$ component of L1Calo uses more granular information considering only 'jet elements' that are the sums of 2×2 trigger towers in both the EM and hadronic calorimeters. Again, the sliding window algorithm is used to form jet candidates looking for local maxima inside 2×2 jet element windows (corresponding to $\Delta\eta \times \Delta\phi = 0.4 \times 0.4$). The E_{T} in the 2×2, 3×3 or 4×4 windows around this 2×2 core are compared to a threshold. For the 3×3 window there are 4 possible arrangements so the one with the maximum summed E_{T} is used. The choice of window size depends on the multiplicity of the trigger: small windows work best for higher multiplicity triggers to aid in resolving multiple jets.

To form a L1 $E_{\mathrm{T}}^{\mathrm{miss}}$ value the E_{T} values in the jet elements are multiplied by the appropriate geometric constants to convert them into the correct E_x, E_y values. These values are then summed across the whole detector and the calculation $E_{\mathrm{T}}^{\mathrm{miss}} = \sqrt{E_x^2 + E_y^2}$ is performed using a lookup table (LUT) to perform the square root.

3.4.1.2 L1 Muon

The trigger decision for muons within $|\eta| < 1.05$ is provided by the RPCs in the barrel. In the range $1.05 < |\eta| < 2.4$ the decision is provided by the TGCs in the endcaps. In the barrel a low p_{T} trigger is provided by requiring coincident hits in at least 3 of the 4 layers of the inner two planes. A high p_{T} trigger then requires both the low p_{T} trigger and then looks for coincident hits in the third plane. A similar logic applies for the endcaps, however there the low p_{T} trigger is provided by the outer planes and the high p_{T} confirmation comes from the inner layer. In Run 2 an additional TGC hit was required in the range $1.3 < |\eta| < 1.9$ to reduce the background from particles that did not originate from the interaction point.

3.4.2 HLT

Where the L1 trigger is only able to consider the detector in sections the HLT detector is able to view the whole detector at once. However, CPU intensive algorithms such as track reconstruction are still often only executed within regions of interest (RoIs) defined by the L1 trigger objects. HLT objects are usually designed to be as close to their offline counterparts (section 3.5.2) as possible with differences typically only where large restrictions from available resources apply. For example, jet triggers do not usually use tracking information for calibration or pile-up suppression. The $E_{\mathrm{T}}^{\mathrm{miss}}$ trigger is a signature which shows considerable differences between online and offline reconstruction and is covered in depth in chapter 4.

3.5 Physics object reconstruction

The data that is output directly by the detector components is not produced in a form which is easily accessible for analysis uses. Therefore specialised algorithms are run to *reconstruct* the particles which originally caused the signals in the detector. The reconstruction proceeds in several steps. First, the outputs of the various subdetectors are interpreted as low level objects: clusters, tracks and vertices. Next, these are combined to form candidates for the various categories of physics objects. Finally, these candidates are evaluated against a variety of quality criteria to minimise the contributions from backgrounds.

3.5.1 Low level objects

3.5.1.1 Clusters

Clusters are formed from measurements of the individual calorimeter cell energies. Two types of cluster are used in ATLAS: ‘egamma’ clusters formed using a sliding window algorithm and ‘topoclusters’ formed using a topological clustering algorithm. The egamma clusters are formed using data only from the EM calorimeters whereas the topoclusters use data from both EM and hadronic calorimeters. Another important distinction is that the sliding window forms only a two-dimensional space of clusters, whereas topoclusters form in three dimensions. The algorithms for forming both of these are described in more detail in [105].

The sliding window algorithm considers fixed windows in $\Delta\eta \times \Delta\phi$. All possible windows that contain a total E_{T} above a threshold are considered as seeds, if two seeds overlap then the one with the higher E_{T} is chosen. The final clusters are then formed around the barycentres of those seeds.

The topocluster algorithm groups together nearby cells into clusters and proceeds in three main steps, each with an associated threshold. The thresholds are expressed in terms of a ratio to the cell’s expected noise value, σ. First, all cells with $|E| > t_{\mathrm{seed}} = 4\sigma$ are labelled as proto-clusters. Next, cells with $|E| > t_{\mathrm{neighbour}} = 2\sigma$ which are next to a proto-cluster are added to that proto-cluster, expanding it. If the cell is adjacent to two proto-clusters then they are merged. This continues until there are such cells adjacent to any proto-clusters. Finally, all cells surrounding proto-clusters with $|E| > t_{\text{cell}} = 0$ are added to their neighbouring proto-clusters and the clusters are formed. In order to prevent loss of sensitivity to close-by particles these clusters can be split by breaking apart clusters which contain multiple significant local maxima.

For topoclusters there is a further, optional, calibration called the local cluster weighting (LCW) [106]. This is designed to address three main effects: the non-compensating nature of the ATLAS calorimeters, energy lost where shower energy is deposited outside of the cluster and energy losses from inactive parts of the detector. Clusters not using this calibration are described as being measured at the EM scale and clusters with it at the hadronic scale[3].

3.5.1.2 Tracks

Tracks are built from hits in the pixel, SCT and TRT detectors and, for muon tracks, the muon spectrometer. Raw measurements from the tracking detectors are clustered to form three dimensional 'space-points'. The algorithms used for tracking typically work by building seeds from coincident hits in nearby layers and then extending these tracks based on the hypothesis that the track was produced by either a pion or an electron. The hypothesis is used to allow for different energy losses due to interactions with the detector material.

Forming a candidate from a collection of three coincident space-points allows for an initial momentum hypothesis. Then, points from the other layers of the pixel or SCT that are compatible with the candidate's trajectory, allowing for the effect of the magnetic field, are considered and absorbed into the candidate. Multiple such points might exist, in which case multiple separate candidates will be formed.

Track candidates are then fit using a χ^2 procedure. Inner detector tracks are built using the pion hypothesis by default. If the fit fails or if the track falls within an egamma cluster the electron hypothesis will also be tested. The track candidates are compared against each other to resolve ambiguities where multiple candidates

[3] This is, perhaps, a misnomer as the calibration is designed to correct hadronic deposits while retaining EM scale calibrations for EM deposits.

share clusters[4]. Each candidate is scored based on the clusters associated to it, the numbers of holes[5], the output of the χ^2 fit and its momentum. Low scoring tracks are then removed, using restrictions on the numbers of tracks which can share a cluster and the number of shared clusters a track can contain.

The tracks are then extended into the TRT, extrapolating the trajectory of the track from the silicon detectors and including hits in the TRT if they are compatible. A second, 'outside-in' track building process is also run where pattern recognition is used to group TRT hits that are not already associated to silicon tracks into seeds. These seeds are then extrapolated inwards. This recovers tracks lost during the ambiguity resolving process and those which originate from secondary vertices. This process of building candidates and fitting them to hypotheses is CPU intensive, which restricts the amount of tracking information available at the trigger level.

In the muon spectrometer hits in the muon chambers are collected to form 'segments' in each layer of the detector. Segments are then used as seeds to build candidate tracks combining multiple compatible tracks. As with inner detector tracks multiple track candidates can be formed and so a similar overlap procedure must be performed.

3.5.1.3 Vertices

Vertices are constructed as the place where multiple tracks passing certain quality requirements [107] intersect. Vertices are classified as either primary or secondary vertices. Primary vertices are those compatible with being on the beam axis, whereas secondary vertices are those which lie further away. Secondary vertices are typically due to the decay of long-lived particles such as B mesons or due to effects like photon conversion where a photon interacts with the detector material to produce an electron-positron pair. The primary vertex with the highest $\sum p_T^2$ over its associated tracks is designated as the hard-scatter vertex. This is often

[4]Note that it is expected for *some* clusters to be shared as multiple charged particles can pass through the same detector area.

[5]A hole is place where the track intersects a section of active tracking material but does not have an associated space-point there.

just referred to as *the* primary vertex. Most physics analyses will only select events in which such a vertex has been identified.

3.5.2 Particle reconstruction

The low level objects described above in 3.5.1 are then used to form candidates for final state particles: photons and e, μ and τ leptons[6]. Due to the effects of hadronic showering 2.2.5.1, individual quarks and gluons are not identified, instead all final state hadronic particles are reconstructed as jets. Some of these jets may then later be *tagged* as being due to a b quark. As reconstructed τ leptons are not used in this thesis the details of their reconstruction will not be covered here.

3.5.2.1 Jets

Jets in ATLAS are formed by running clustering algorithms using the topoclusters as inputs[7]. Jets are designed to try and recapture as much of the kinematics of the original quark or gluon whose shower they capture. The non-perturbative nature of QCD means that it isn't possible to perfectly predict hadronisation. In particular, soft and colinear splittings are not described by the theory. Therefore, modern jet algorithms are required to satisfy two constraints, *infrared* and *colinear* safety, which require that neither the addition of a soft particle or a colinear emission is able to change which jets are formed in the event. Modern jet algorithms now belong to a class of algorithms called sequential recombination algorithms which obey this property [108].

Sequential recombination algorithms begin by considering all input objects as protojets. Two types of distance are defined: the distance between two protojets d_{ij} and a second often called the 'beam distance' d_{iB}. These distances are calculated for each of the protojets and the shortest one selected. If this is a distance between two protojets they are combined and the distances to the new protojet recalculated.

[6]The same identification techniques tend to be applied to anti-particles as to their corresponding particles.

[7]Other jet collections are sometimes used formed from other objects such as tracks or trigger towers, but these are beyond the scope of this thesis.

If it is a beam distance then the protojet is labeled a jet and no longer participates in the algorithm. This process continues until no protojets remain.

The major three jet algorithms used at ATLAS fall into this class. They use the distance measures

$$d_{ij} = min(k_{ti}^{2p}, k_{tj}^{2p})\frac{\Delta R_{ij}^2}{R^2}, \qquad d_{iB} = k_{ti}^{2p},$$

where $\Delta R_{ij}^2 = (y_i - y_j)^2 + (\phi_i - \phi_j)^2$ and k_t, y and ϕ are the transverse momentum, rapidity and azimuthal angle respectively. The three algorithms differ only in the sign of p: $p = 1$ is called the k_t algorithm, $p = 0$ is the Cambridge-Aachen algorithm and $p = -1$ is the anti-k_t algorithm. The k_t algorithm tends to cluster soft particles first, the Cambridge-Aachen algorithm is blind to the momenta of its inputs and the anti-k_t algorithm clusters the hardest inputs first. This means that the jets that it builds tend to be stable whereas the jets produced by the other algorithms tend to 'walk' around the detector, producing jets which cover large areas. These are then hard to predict theoretically and also are far more sensitive to pileup. In the anti-k_t algorithm most jets will form circles in $y - \phi$ space.

In ATLAS the main jet collection is produced with a radius parameter of $R = 0.4$ and produced using the EM scale topoclusters as inputs. These jets are then calibrated in order to correct for differences between the measured and true jet energies as determined in simulation. Certain aspects of this calibration are not available at the trigger level as they depend on quantities such as the track multiplicity.

Jets from pile-up vertices are identified by using tracking information [109]. Tracks are ghost-associated [110] to jets and two separate variables are calculated. The *jet vertex fraction* (JVF) is the ratio of the sum over the p_{T} of tracks associated to the jet from the primary vertex to the sum over the p_{T} of all tracks associated to the jet. A correction is then applied to ensure that the efficiency of this method is flat with changes to the number of primary vertices yielding a quantity called corrJVF. The ratio between the sum over the p_{T} of tracks associated to the jet and primary vertex to the measured p_{T} of the jet is called R_{p_T}. A k nearest neighbours

($k = 100$) algorithm trained on Monte Carlo simulation is used to construct a single discriminant from these R_{p_T} and corrJVF variables called JVT. Jets with p_{T} between 20 and 50 GeV[8] have an additional selection on JVT to remove contributions from pile-up jets. Normally a *medium* working point is chosen which marks jets as pile-up if they have JVT < 0.59, over the p_{T} range to which it is applied this selection has an average efficiency of 92%.. This quantity can only be calculated for jets which lie within tracking acceptance $|\eta| < 2.4$.

3.5.2.2 Heavy flavour tagging

Hadrons containing heavy quarks such as b and, to a lesser extent, c quarks have longer lifetimes and decay a short distance away from the primary vertex. This produces several experimental signatures which can be used to distinguish these objects from jets produced by light objects (u, d and s quarks and gluons). In ATLAS three separate algorithms are used to identify these features: one which identifies large impact parameters between the tracks in the jet and the primary vertex, one which identifies secondary vertices within the jet and another which attempts to reconstruct a full b hadron decay chain inside the jet. The results of these algorithms are then combined using a *boosted decision tree* (BDT) [111] to produce a single discriminant to identify jets initiated by b quarks. The standard working point used in ATLAS identifies b-jets with a 77% efficiency with rejection factors of 6 and 134 on c and light jets respectively.

3.5.2.3 Reclustered jets

The $R = 0.4$ radius chosen for the main jet collection is designed to capture the full hadronic shower from a light quark or gluon initiated jet. However, heavier particles such as gauge bosons or t quarks have wider decay angles and, depending on their p_{T}, require a wider jet to capture them. 'Large-R' jets with $R = 1.0$ are produced with derived calibrations, however these are very sensitive to pile-up and $R = 1.0$ may not be ideal for many analyses. Instead, the existing $R = 0.4$ jets can be 'reclustered'. A second iteration of the anti-k_t algorithm is run with a large

[8]The upper end of this range was extended to 60 GeV in 2017.

radius parameter (e.g. $R = 1.0$) using the existing calibrated $R = 0.4$ jets as inputs. The produced reclustered jets inherit the calibrations of their $R = 0.4$ constituents and therefore do not need further calibration. The radius of the reclustered jets can then be chosen by individual analysis groups.

3.5.2.4 Electrons

Electron candidates [112] are formed by the coincidence of an egamma cluster and a track.

Electron identification is then performed using a multivariate likelihood technique. Various discriminating variables are constructed, including measured shower widths and ratios between energy deposits in different areas of the calorimeter as well as track quality criteria. The probability density functions for these are calculated from Monte Carlo for signal and backgrounds such as converted photons and jets. Then, for any given electron candidate these variables are measured and the discriminant $d_{\mathcal{L}}$ is constructed as

$$d_{\mathcal{L}} = \frac{\mathcal{L}_S}{\mathcal{L}_S + \mathcal{L}_B}, \qquad \mathcal{L}_{S(B)}(\vec{\boldsymbol{x}}) = \Pi_{i=0}^{n} P_{S(B),i}(x_i),$$

where $\vec{\boldsymbol{x}}$ is the vector of discriminating variables and $P_{S(B),i}$ are the probability density functions for them as measured on signal (background). Three operating points are supported: *Loose*, *Medium* and *Tight* which differ only in the threshold placed on this discriminant with a fourth *LooseBLayer* only differing in the addition of an extra selection on the number of track hits in the innermost pixel layer. The efficiencies of the working points vary with $|\eta|$ and p_{T}. Averaging over $|\eta|$ the efficiency of the Loose, Medium and Tight working points for a 25 GeV electron are 93%, 89% and 80% respectively. The corresponding efficiencies for the dijet background are 0.24%, 0.4% and 0.58%.

Usually analyses will also require the track to be consistent with coming from the primary vertex. The track's impact parameter d_0 is measured and its uncertainty σ_{d_0} estimated and the requirement ${}^{d_0}/_{\sigma_{d_0}} < 5$ is made. The track is also required to satisfy $\Delta z_0 \sin\theta < 0.5$mm where Δz_0 is the difference between the z coordinates of the primary vertex and the point of closest approach between it and the track and θ is the polar angle of the track. This reduces the impact of electrons from pile-up vertices and in-flight decays.

3.5.2.5 Photons

Photon identification [113] is performed through a series of selections on calorimeter based variables, similar to those used in the electron identification. The variables are designed to characterise the lateral and longitudinal shower development in the EM calorimeter and the fraction of the energy which leaks into the hadronic calorimeter. Additional variables are added to remove backgrounds from the decay $\pi^0 \to \gamma\gamma$. Two levels of identification are defined: *Loose* and *Tight*. The loose ID only uses measurements of the shower shape in the second layer of the EM calorimeter and energy deposited in the hadronic calorimeter. It has an efficiency of 99% for $E_{\mathrm{T}}^{\gamma} = 40\,\mathrm{GeV}$. The corresponding rejection factor is 1000 for jets with $p_{\mathrm{T}} > 40\,\mathrm{GeV}$. Only the tight ID is recommended for analysis use, which uses the full calorimeter information and also excludes any photons which fall in the calorimeter transition region at $1.37 < |\eta| < 1.52$. This working point has an efficiency of 85% for $E_{\mathrm{T}}^{\gamma} = 40\,\mathrm{GeV}$ and a corresponding rejection factor of 5000. Photons can also interact with the detector via the matter interaction $X + \gamma \to X + e^+e^-$. Various constraints are applied to distinguish between these *converted* photons and electrons.

3.5.2.6 Muons

Muon candidates [114] are formed by associating together segments found in the track-finding stage. Segments are selected based on the number of hits and the quality of the fit used to create them. At least two segments from the muon spectrometer are required to be consistent in order to form a track except in the transition region between the barrel and endcap where a single segment can be used if it is of a high enough quality. For $|\eta| < 2.5$ the candidate track is projected back to the inner detector, using the simulation of the geometry of the magnetic field to calculated the trajectory of a particle passing through it. An inner detector track is required to match this projection and a global refit is performed, including allowing for the removal or addition of hits from the muon spectrometer. This 'outside-in' approach can then be complemented by an 'inside-out' approach where tracks in the inner detector are extrapolated out to the spectrometer. The inner detector does not cover the region $2.5 < |\eta| < 2.7$ so here a more stringent requirement is made on the candidate formed from muon spectrometer track segments and the track is extrapolated back to the center of the detector to ensure it is consistent with being from the interaction point.

Muons selected for analysis purposes are typically required to pass *Medium* identification criteria. The variables selected on for this are the significance of the differences in measurement in the charge to momentum ratio and the p_{T} measurements from the tracks in the inner detector and muon spectrometer, as well as the χ^2 of the track fit. The inner detector tracks used are also required to pass selection criteria based on the numbers of measured hits. The muon spectrometer tracks are required to have at least 3 hits in at least 2 layers of the MDTs, except for $|\eta| < 0.1$ where there is hole for detector services. Muons in this region are required to have hits in only 1 layer of MDTs but are vetoed if there is more than 1 hole in the MDTs. For muons with $20 < p_{\mathrm{T}} < 100\,\mathrm{GeV}$ this working point has an efficiency of 96.1%. The efficiency for muons resulting from in-flight decays of hadrons (a background) is 0.17%.

3.5.2.7 Isolation

In analyses it is usually only desirable to select 'prompt' objects which are produced directly in the signal process as opposed to those produced by other decay products as they pass through the detector. Non-prompt objects can also include fakes, for example muon candidates produced by 'punch-through' where a hadronic shower is not completely absorbed by the calorimeter.

Isolation requirements [115] are selections made on the measured energy in either tracks or calorimeter deposits immediately surrounding the identified particle. For the calorimeter isolation variables the energies of all topoclusters within a cone of fixed width ($R = 0.2$, 0.3 or 0.4) are measured. For electrons and photons the energies from cells contained in a fixed window around the particle's direction are subtracted from this variable, along with an extra 'leakage' correction derived from Monte Carlo simulation which allows for energy that falls outside this region. For muons the track is extrapolated through the calorimeter and the energies of any topoclusters within ΔR of it are subtracted. For each of these particles an additional correction is applied to remove contributions from pile-up.

For the track isolation variables the transverse momenta of tracks passing quality requirements which fall within a cone of variable radius $R = \min({}^{10\,\text{GeV}}/p_{\text{T}}, R_{\text{max}})$ where R_{max} is either 0.2, 0.3 or 0.4 are summed. For muons the p_{T} of the muon track is subtracted. For electrons and converted photons the p_{T}s of all tracks within $\Delta\eta = 0.05 \times \Delta\phi = 0.1$ of the particle are subtracted to ensure that particles produced from bremsstrahlung are not included in the isolation energy figure.

Isolation working points are formed from selections in bins of p_{T} and η designed to achieve a flat efficiency across all bins. Alternatively 'Gradient' points can be used which target an efficiency which increases linearly with p_{T}, taking advantage of the fact that backgrounds tend to reduce at higher energies. Aside from the loosest working point all working points use both track and calorimeter isolation variables. For calorimeter isolation $R = 0.2$ is used for all particles. For track isolation the muon selections uses $R = 0.3$ and electron and photon selections use $R = 0.2$.

The two working points usesd in thesis are *Gradient* and *GradientLoose*. These have efficiencies of 90% and 95% respectively for objects with $p_{\text{T}} = 25\,\text{GeV}$, the efficiencies for both rise to 99% by $p_{\text{T}} = 60\,\text{GeV}$.

3.5.2.8 Overlap removal

The reconstruction algorithms are run separately from each other so it is possible for the same set of energy deposits to be interpreted as being from two different particles. For example, an electron being absorbed by the EM calorimeter is very likely to also be reconstructed as a jet candidate. In order to avoid double-counting or misidentification, objects that are very close together or share tracks are compared and one removed. This also helps to remove backgrounds such as

Kept Particle	Removed Particle	Overlap Criteria
electron	electron	shared track (higher p_T particle is kept)
muon	electron	shared inner detector track
electron	photon	$\Delta R < 0.4$
muon	photon	$\Delta R < 0.4$
electron	jet	$\Delta R < 0.2$*
jet	electron	$\Delta R < 0.4$
muon	jet	$n_{\text{trk}}(\text{jet}) < 3$ and either $\Delta R < 0.2$ or the muon is ghost-associated to the jet*
jet	muon	$\Delta R < 0.4$
jet	photon	$\Delta R < 0.4$

Figure 3.8: Table showing the criteria for overlap removal. Each row shows a step in the overlap removal process. If two particles of the types in the first two columns satisfy the criteria in the third the first is kept and the second removed and will not participate in subsequent steps. An alternative working point for heavy-flavour based analyses can also be used. In this working point the criteria in the starred rows are only used to remove jets which are not tagged as b-jets. This procedure can be expanded to include τ leptons but this is not done in this thesis.

photons produced by bremsstrahlung or leptons produced during hadronic decays. The priorities for these are shown in table 3.8.

3.5.3 $E_{\mathrm{T}}^{\mathrm{miss}}$

The $\vec{\boldsymbol{p}}_{\mathrm{T}}^{\mathrm{miss}}$ [116] is calculated as

$$\vec{\boldsymbol{p}}_{\mathrm{T}}^{\mathrm{miss}} = -\sum_{e} \vec{\boldsymbol{p}}_{\mathbf{T}} - \sum_{\gamma} \vec{\boldsymbol{p}}_{\mathbf{T}} - \sum_{\mu} \vec{\boldsymbol{p}}_{\mathbf{T}} - \sum_{\tau} \vec{\boldsymbol{p}}_{\mathbf{T}} - \sum_{\text{jets}} \vec{\boldsymbol{p}}_{\mathbf{T}} - \sum_{\text{soft tracks}} \vec{\boldsymbol{p}}_{\mathbf{T}}$$

where the first four terms are summed over the electrons, photons, muons and taus as defined by the analysis selections. The jet term is summed over all jet candidates passing selections designed to reduce the impact of pile-up. Jets in the central region of the detector ($|\eta| < 2.4$) are required to pass the JVT selection described in section 3.5.2.1. In the forward region jets are required to have $p_{\mathrm{T}} > 20$ GeV, though as pile-up increased into the later parts of 2016 this threshold was raised to 30 GeV.

The input objects to the $E_{\mathrm{T}}^{\mathrm{miss}}$ reconstruction are from before overlap removal as the reconstruction performs its own overlap removal; where calorimeter deposits are associated to multiple objects they are assigned in the following order: electrons, photons, hadronically decaying taus, jets, then muons.

After this, contributions from soft objects in the event are used to provide a further correction called the soft term. Clusters or tracks can be used to form this, however the calorimeter cluster variant is extremely sensitive to pile-up and is not typically used. Instead the tracks are used to build the *track soft term* (TST). Tracks passing quality criteria which do not point into any object already used in the reconstruction are added into the soft term.

4

The $E_{\mathrm{T}}^{\mathrm{miss}}$ trigger

Contents

4.1 Statement of original work

The work presented in this chapter is largely my own, though parts were done in collaboration with other members of the ATLAS $E_{\mathrm{T}}^{\mathrm{miss}}$ trigger group. In particular the algorithms discussed in this chapter were developed before the start of Run 2 and before I joined the experiment. Where I have not directly produced a figure this has been noted in that figure's caption.

4.2 Introduction

4.2.1 The $E_{\mathrm{T}}^{\mathrm{miss}}$ trigger

The general concept of triggers in ATLAS is covered in section 3.4. Not all particles can be measured by the ATLAS detector. Particles that do not carry either electromagnetic or strong charge, e.g. neutrinos, will not interact with the calorimeter or tracking systems and therefore the detector will not 'see' them. Particles of this sort are typically called *invisible*. However, we can still usually deduce their presence by applying conservation of momentum in the transverse plane[1]. We define $\vec{\boldsymbol{p}}_{\mathrm{T}}^{\mathrm{miss}} = -\sum_i \vec{\boldsymbol{p}_{\boldsymbol{T}}}_i$, the negative vector sum over all measured particles' transverse momenta, to be the missing transverse momentum vector. In a perfect detector this would correspond to the sum of the transverse momenta of all the invisible particles in the event. We then define $E_{\mathrm{T}}^{\mathrm{miss}} = |\vec{\boldsymbol{p}}_{\mathrm{T}}^{\mathrm{miss}}|$[2].

Sources of true $E_{\mathrm{T}}^{\mathrm{miss}}$ are rare in the Standard Model as the only invisible particle is the neutrino. Many BSM theories predict processes which can produce large quantities of $E_{\mathrm{T}}^{\mathrm{miss}}$. Studies of astrophysical data reveal inconsistencies between measured galactic rotation curves and the predicted curves based on observed materials. Similarly, gravitational lensing is observed in areas of space with no other observed matter. The leading theory to explain these inconstencies is a new theoretical particle called a WIMP (Weakly Interacting Massive Particle),

[1]We are unable to apply this constraint along the z (beam) axis as a) the interacting partons can hold varying momentum fractions of the incident protons so we do not know the initial value of p_z and b) we cannot place detector material over the beam pipe itself so material with a high p_z can escape.

[2]Technically this variable should be called missing transverse *momentum*

commonly referred to as dark matter. These particles would have to carry no electromagnetic or strong charge and therefore if produced in an LHC collision would appear in ATLAS as $E_{\mathrm{T}}^{\mathrm{miss}}$.

4.2.1.1 Muons in the $E_{\mathrm{T}}^{\mathrm{miss}}$ trigger

Typically the $E_{\mathrm{T}}^{\mathrm{miss}}$ trigger uses solely calorimeter information. High energy particle energy loss in a calorimeter comes largely from two sources [117]; the 'electronic stopping power' described by the Bethe-Bloch formula [101] and radiative processes such as bremsstrahlung and particle pair production. The energy loss from radiative processes is far greater than loss from the electronic stopping power.

The loss from bremsstrahlung (which dominates the radiative energy loss) scales roughly as E/m^2, where E and m are the energy and mass of the particle. Energy loss is therefore only significant for particles above some critical energy E_c (which depends on the material of the calorimeter). The relationship between the electron and muon critical energies is therefore approximately $E_{\mu,c}/E_c \approx (m_\mu/m_e)^2 \approx 4 \times 10^4$. This typically leads to values of $E_{\mu,c}$ on the order of several 100 GeV - 1 TeV. This means that muons below this energy experience only relatively small losses when passing through the electromagnetic calorimeter.

Hadronic calorimeters are designed for the detection of hadrons. Given that muons do not carry strong charge they also interact very weakly with this calorimeter.

Together these effects mean that the majority of the energy of a muon is not detected by the calorimeter and therefore muons appear effectively as invisible particles in the $E_{\mathrm{T}}^{\mathrm{miss}}$ trigger.

This is exploited by some analysis groups who use the trigger to select events with high energy muons (the dedicated ATLAS muon trigger does not reach 100% efficiency but can select much lower energies than the $E_{\mathrm{T}}^{\mathrm{miss}}$ trigger). This does not adversely affect trigger rate as a) high energy muons are rare and b) most of these events will also pass a muon trigger so do not contribute to the signature's *unique* rate (Section 4.5.2).

4.2.2 Theoretical treatment of background

Due to the scarcity of SM processes that produce true $E_{\mathrm{T}}^{\mathrm{miss}}$ the events passing the $E_{\mathrm{T}}^{\mathrm{miss}}$ trigger are dominated by object mismeasurement. An event with no true $E_{\mathrm{T}}^{\mathrm{miss}}$ can gain a measured $E_{\mathrm{T}}^{\mathrm{miss}}$ through the coincidental alignments of the mismeasurements of the individual objects in it. A simple model of this effect can be derived as follows. A more complete derivation can be found in Ref. [118]. We assume that we can model the probability density function (pdf) for the mismeasurement $\delta_x = p_x^{\mathrm{true}} - p_x^{\mathrm{measured}}$ of an object as a Gaussian distribution

$$f_i(\delta_{x,i}|\sigma_i) = \frac{1}{\sigma_i\sqrt{2\pi}} e^{-\frac{1}{2}\frac{\delta_{x,i}^2}{\sigma_i^2}} . \tag{4.1}$$

The mismeasurement of the x component of the sum over all the objects $\delta_x = \sum_i \delta_{x,i}$ is then also described by equation 4.1 ($f(\delta_x|\sigma)$) where $\sigma^2 = \sum_i \sigma_i^2$ [3]. We can therefore calculate the pdf for the $E_{\mathrm{T}}^{\mathrm{miss}}$ from mismeasurement[4],

$$f(x,y|\sigma)\mathrm{d}x\mathrm{d}y = f(x|\sigma)f(y|\sigma)\mathrm{d}x\mathrm{d}y = \frac{1}{2\pi\sigma^2} e^{-\frac{1}{2}\frac{x^2+y^2}{\sigma^2}} \mathrm{d}x\mathrm{d}y \,.$$

Performing a change of variables

$$x = z\cos\theta \qquad\qquad y = z\sin\theta\,,$$

using the Jacobian

$$\left|\frac{\partial(x,y)}{\partial(,\theta)}\right| = z$$

and then integrating over θ yields

$$\begin{aligned} f(z|\sigma)\mathrm{d}z &= \int_0^{2\pi} \mathrm{d}z\mathrm{d}\theta \frac{z}{2\pi\sigma^2} e^{-\frac{1}{2}\frac{z^2}{\sigma^2}} \\ &= \frac{z}{\sigma^2} e^{-\frac{1}{2}\frac{z^2}{\sigma^2}} \end{aligned} \tag{4.2}$$

[3] This is a general result for the sum of uncorrelated Gaussian distributed variables

[4] Note we assume that the σ for mismeasurement is the same for the x and y components (which is generally true). We also assume that the mismeasurement is uncorrelated between x and y. This is not actually true but it's a good approximation when there are sufficiently many objects in the sum

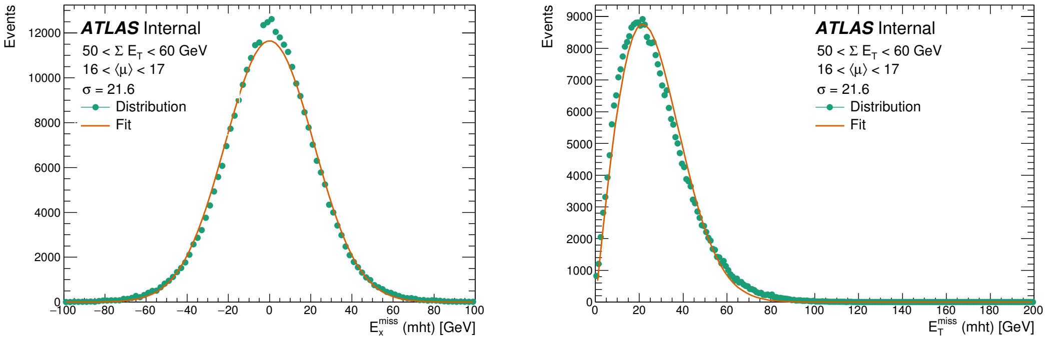

Figure 4.1: The $E_{\mathrm{T}}^{\mathrm{miss}}$ (left) and the E_x^{miss} (right) distributions in ZeroBias events measured using the `mht` algorithm. The theoretical prediction derived in section 4.2.2 is also shown with the same value of σ used in both plots. The fits are imperfect because the events in the plots are sampled from a narrow range of σ values.

which is the Rayleigh distribution. Therefore the probability for an event with no true $E_{\mathrm{T}}^{\mathrm{miss}}$ and a given σ to pass a $E_{\mathrm{T}}^{\mathrm{miss}}$ trigger with threshold t is given by

$$\begin{aligned} P(z > t|\sigma) &= \int_t^\infty \mathrm{d}z \frac{z}{\sigma^2} e^{-\frac{1}{2}\frac{z^2}{\sigma^2}} \\ &= e^{-\frac{1}{2}\frac{t^2}{\sigma^2}} \end{aligned} \tag{4.3}$$

which is proportional to the rate from this source. The resolution parameter σ is well described by a function of the pile-up and ΣE_{T}

$$\sigma = a + b\sqrt{\Sigma E_{\mathrm{T}}} + c\mu\,. \tag{4.4}$$

Note that this formula is empirical. Figure 4.1 shows the $E_{\mathrm{T}}^{\mathrm{miss}}$ and E_x^{miss} distributions for ZeroBias ATLAS data and a fit to the Rayleigh and Gaussian distributions (using the same value of σ).

4.3 Datasets used in this section

Given that the trigger system is responsible for choosing which events enter the output datasets, some care must be applied in selecting which events are used when analysing its performance. For instance, attempting to measure the efficiency of a trigger in a dataset which includes events *only* selected by that trigger introduces an obvious bias into that measurement. A variety of datasets are used in the studies presented in this chapter. The most important ones are presented here.

`physics_Main`: the dataset collected by the logical OR of all the 'physics' triggers. Almost every ATLAS analysis will use a subset of this dataset (selecting only events passing certain triggers). In general this is not a suitable dataset to be used in trigger studies as it is biased.

Signal selections: a variety of signal selections are defined (detailed in section 4.5.1.1). These each define a subset of `physics_Main` designed to be unbiased to the $E_{\mathrm{T}}^{\mathrm{miss}}$ trigger as each includes a selection on a non-$E_{\mathrm{T}}^{\mathrm{miss}}$ trigger. These samples are primarily used to measure $E_{\mathrm{T}}^{\mathrm{miss}}$ trigger efficiencies.

`HLT_noalg`: a set of triggers are defined that require that an L1 $E_{\mathrm{T}}^{\mathrm{miss}}$ trigger is passed and make no requirement on the HLT. Very high prescales[5] are set on these triggers to keep their rates down and they consequently have a very low pass rate. This means that they do not typically collect enough data in a single run to be useful, however looking at the data they collect over a longer period of time is very useful as they represent an unbiased subset of the events on which the HLT $E_{\mathrm{T}}^{\mathrm{miss}}$ triggers operate. This makes them very useful for evaluating background rejection though they usually do not collect enough 'signal-like' events to allow efficiency to be studied.

`ZeroBias`: is collected by the logical OR of a random trigger `HLT_noalg_zb_L1ZB` and a random trigger purposefully biased towards higher p_T events `HLT_j40_L1ZB`. This, especially the subset of events collected only by the first trigger, is a useful sample for studying the events on which the L1 triggers operate as well as providing an almost unbiased sample for studying the properties of basic QCD events.

[5] A prescaled trigger randomly rejects a certain fraction of events before the physics-based decision is applied. For example, a trigger with a prescale of 200 would only calculate the physics decision on 1 in every 200 events

Year	2015	2016
ATLAS Good Luminosity [pb^{-1}]	3219.56	32884.6
Events in `physics_Main`	1209497446	5119135614

Sample	2015			2016		
	All	`L1_XE50`	`mht90`	All	`L1_XE50`	`mht90`
$Z \to \mu\mu$	832711	19051	15255	7.65×10^{6}	191460	150010
$Z \to ee$	768508	20760	1041	7.57×10^{6}	225351	14947
$W \to \mu\nu$	1.02×10^{7}	185576	144971	9.93×10^{7}	1.97×10^{6}	1.49×10^{6}
$W \to e\nu$	908088	362923	39584	1.01×10^{8}	6.60×10^{6}	1.22×10^{6}
$H \to e\,\mathrm{Inv}$	338	101	25	6333	1779	553
$H \to \mu\,\mathrm{Inv}$	489	272	237	5488	2906	2377
$t\bar{t} \to b\bar{b}e\nu jj$	17882	8136	2440	378913	147484	57395
$t\bar{t} \to b\bar{b}\mu\nu jj$	31724	13634	10863	327987	144175	114149
$t\bar{t} \to b\bar{b}e\nu\mu\nu$	3822	2104	1421	41663	22572	15330
`HLT_noalg`	88643	88643	5564	3443197	3443197	295324
`ZeroBias`	10749889	9285	600	19538064	11988	1095

Table 4.1: The numbers of events in each dataset, along with the number of events passing certain relevant triggers. `mht90` here is used as shorthand for the trigger `HLT_xe90_mht_L1XE50` and this trigger decision is emulated.

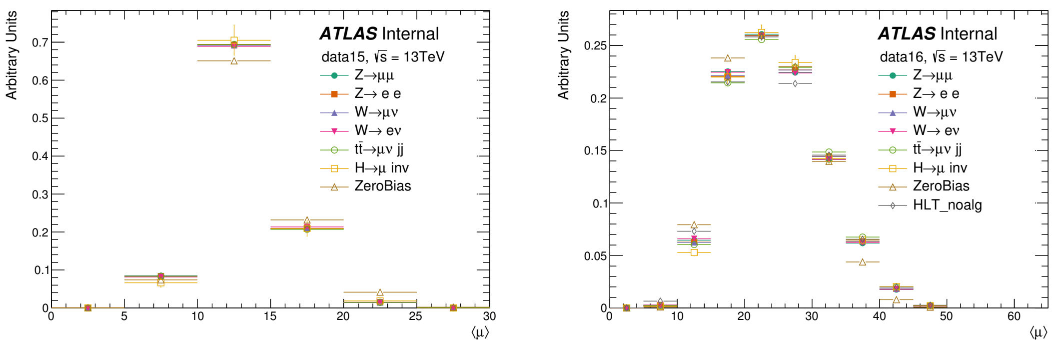

Figure 4.2: The (normalised) pile-up distributions for each dataset used in this section. Distributions are shown for 2015 (left) and 2016 (right). Within each year the pile-up profiles match, showing that the effect of pile-up should be the same across samples.

`EnhancedBias`: is collected by the logical or of a specially selected set of triggers [119] designed to measure HLT trigger rates. The EnhancedBias menu consists of a wide variety of prescaled L1 triggers, covering all signature types and relevant combinations of them as well as different p_{T} ranges. This menu is designed to be invertible, i.e. that a single per-event weight can be calculated and applied to restore an effect ZeroBias spectrum. The menu is only run on special runs that are taken a few times a year.

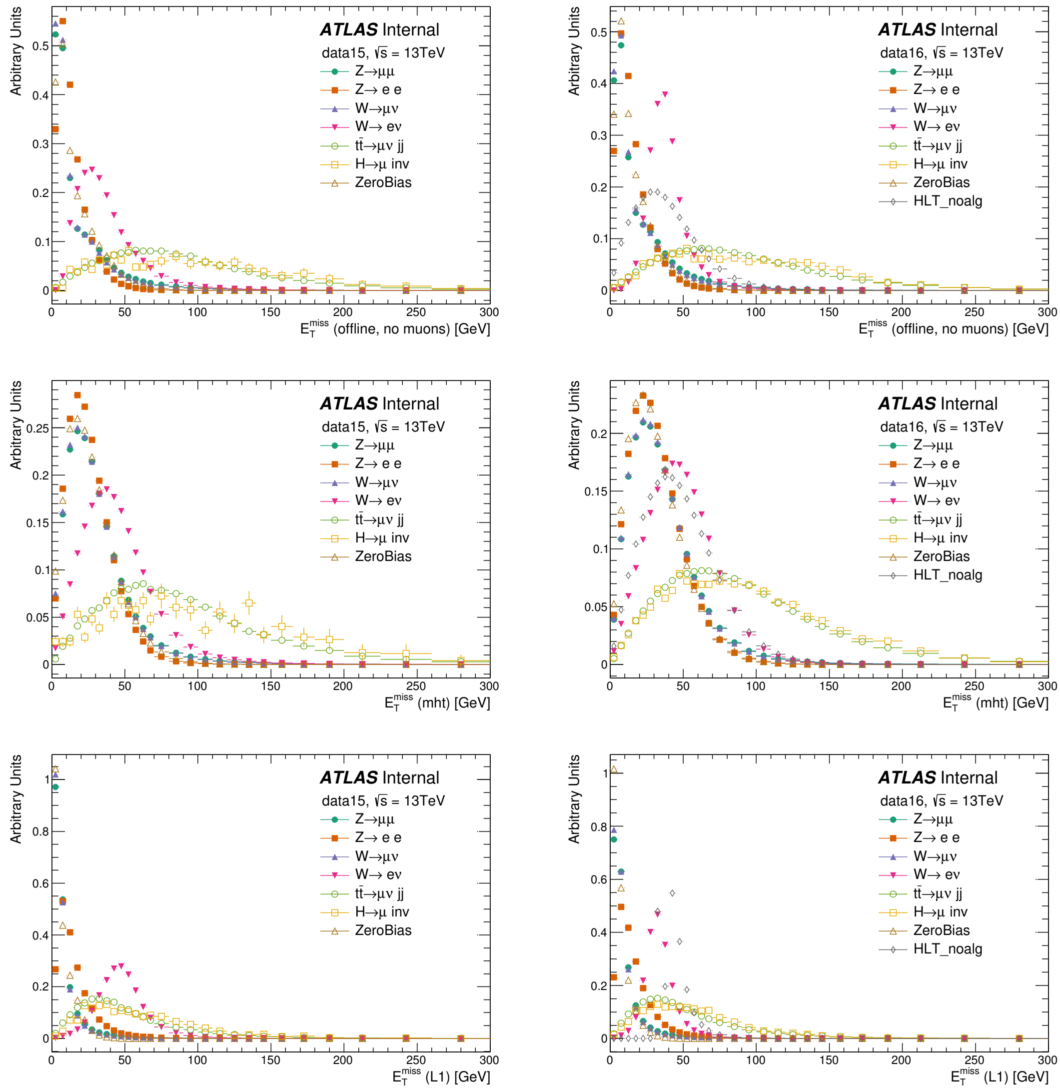

Figure 4.3: The (normalised) $E_{\mathrm{T}}^{\mathrm{miss}}$ distributions for each dataset used in this section. Distributions are shown for 2015 (left) and 2016 (right). The distributions are shown for the $E_{\mathrm{T}}^{\mathrm{miss}}$ value calculated offline, with muons subtracted (top), calculated using the `mht` algorithm (middle) and the value calculated by the `L1` hardware (bottom).

Figure 4.2 shows the pile-up distributions in each dataset. To a large extent the pile-up profiles of these datasets are consistent which means that the effects of pile-up should be the same across them and studies do not have to account for differences. As discussed in section 4.2.2 pile-up degrades the resolution of most calculations of $E_{\mathrm{T}}^{\mathrm{miss}}$ as it increases the number of objects in the sum and therefore increases the resolution parameter σ. Pile-up can also affect σ through effects from previous bunch crossings as the detector read-out electronics' response times are

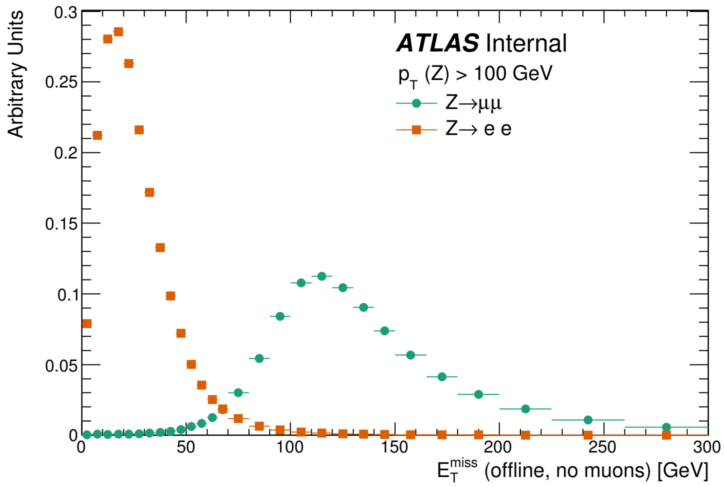

Figure 4.4: The (normalised) $E_{\mathrm{T}}^{\mathrm{miss}}$ distributions for the $Z \to \mu\mu$ and $Z \to ee$ datasets used in this section. Data from 2015 and 2016 are combined. The identified Z boson candidate is required to have p_{T} of at least 100 GeV. After this selection the $Z \to \mu\mu$ candidate events have significant measured $E_{\mathrm{T}}^{\mathrm{miss}}$ but the $Z \to ee$ events do not show the same effect.

substantially longer than the 25ns between bunch crossings. This further degrades the resolution. Ensuring the pile-up distributions match between two datasets is therefore important when trying to compare those datasets to ensure any observed differences do not come from differences in pile-up.

Figure 4.3 shows the $E_{\mathrm{T}}^{\mathrm{miss}}$ distributions for three different $E_{\mathrm{T}}^{\mathrm{miss}}$ definitions in these various datasets. Many of the signal samples shown (described in section 4.5.1.1) show low $E_{\mathrm{T}}^{\mathrm{miss}}$ values in these plots as the cross-sections tend to be dominated by low p_T processes. For example, although the production of Z bosons which then decay to muons is associated with the production of true $E_{\mathrm{T}}^{\mathrm{miss}}$ as measured by the trigger this process is dominated by the production of Z bosons at rest which leads to the $E_{\mathrm{T}}^{\mathrm{miss}}$ distributions in this dataset peaking strongly at 0. This is especially clear in the comparison between the ZeroBias, $Z \to \mu\mu$ and $Z \to ee$ datasets. In the bulk of the distribution these are very similar with the $Z \to \mu\mu$ line only diverging towards higher $E_{\mathrm{T}}^{\mathrm{miss}}$ values where the effects of higher p_{T} Z boson production become more apparent. This is shown in figure 4.4 where an explicit selection on the p_{T} of the Z is made.

4.4 Algorithms

Several different algorithms are defined for calculating the $E_{\mathrm{T}}^{\mathrm{miss}}$ at the trigger level. All work by calculating the $\vec{\boldsymbol{p}}_{\mathrm{T}}^{\mathrm{miss}}$ vector as the sum over the transverse momenta of several input components. They differ by how those components are calculated. The `pufit` algorithm was modified over the course of 2015/2016 running and only really became relevant in late 2016/2017 so this algorithm will not be extensively covered here.

`L1`: The inputs to the sum are the L1 calorimeter trigger towers (Section 3.4.1.1). Note that the sqrt in the calculation of the magnitude of $\vec{\boldsymbol{p}}_{\mathrm{T}}^{\mathrm{miss}}$ is performed using a hardware based look up table. The `L1` $E_{\mathrm{T}}^{\mathrm{miss}}$ trigger is automatically passed if any individual tower overflows regardless of threshold.

`cell`: The inputs to the sum are the individual calorimeter cells (Section 3.3.3.2). A two sided noise suppression is applied so that cells are only included if they pass $|E_i| > 2\sigma,\ E_i > -5\sigma$.

`tc_lcw`: The inputs to the sum are the calorimeter topoclusters (Section 3.5.1.1) with the lcw (local cluster weighting) applied.

`mht`: The inputs to the sum are the trigger level jets built using the anti-k$_t$ algorithm with radius parameter $R = 0.4$ which themselves use the LCW topoclusters as inputs. The jets are calibrated and have an area-based pile-up subtraction applied[120].

`pueta`: This is a modified version of `tc_lcw` with an η based pile-up subtraction performed.

`pufit`: This is a modified version of `tc_lcw` with an event-by-event fit applied to reduce the impact of pileup.

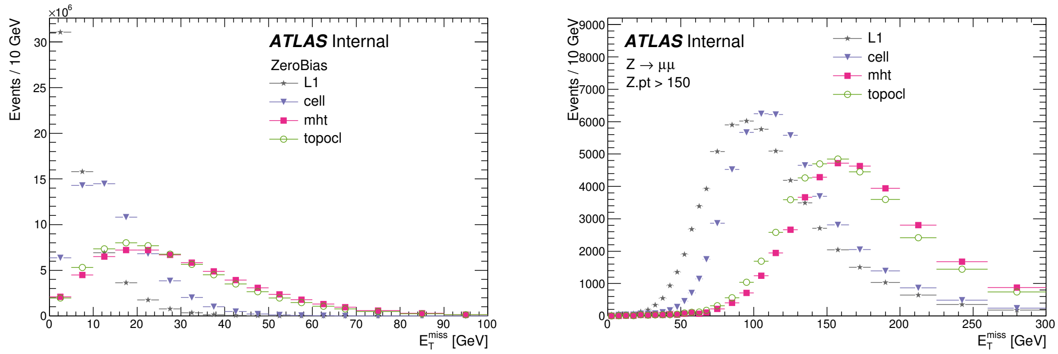

Figure 4.5: The $E_{\mathrm{T}}^{\mathrm{miss}}$ distributions measured using the various algorithms. The distributions are shown for ZeroBias events (left) and $Z \rightarrow \mu\mu$ selected events (right).

4.4.1 $E_{\mathrm{T}}^{\mathrm{miss}}$ trigger names

HLT trigger names in ATLAS follow strict rules as most of the information for determining which selections they apply is contained within the name and parsed by a regular expression within the ATLAS code. Different pieces of information are separated by underscores. A trigger can contain multiple different selections even from different physics channels.

These selections begin with an optional number to signify the multiplicity of the selection (which does not apply to $E_{\mathrm{T}}^{\mathrm{miss}}$ triggers), a string which corresponds to the trigger signature and then another number which represents a threshold to apply. To what this threshold is applied depends on the signature, for example for jets it is the E_T of the jet and for $E_{\mathrm{T}}^{\mathrm{miss}}$ it is the $E_{\mathrm{T}}^{\mathrm{miss}}$ value calculated by the relevant algorithm. The signatures are represented by strings, in lower case for the HLT and in upper case for L1. For example $E_{\mathrm{T}}^{\mathrm{miss}}$ is represented by the string `xe`, jets by the the string `j`, electrons by `e` and muons by `mu`. Examples would be `6j45` which would correspond to a selection requiring 6 jets with an E_T of at least 45 GeV or `xe70` which requires $E_{\mathrm{T}}^{\mathrm{miss}} > 70$ GeV.

Additional pieces of information can follow these segments. In the $E_{\mathrm{T}}^{\mathrm{miss}}$ signature this usually means the algorithm used to calculate the $E_{\mathrm{T}}^{\mathrm{miss}}$ value. In cases where this isn't explicitly stated in the trigger name the `cell` algorithm is used. For example `xe70` requires $E_{T,\mathtt{cell}}^{miss} > 70$ GeV but `xe70_mht` requires $E_{T,\mathtt{mht}}^{miss} > 70$ GeV.

Multiple of these can be combined into a single trigger name. This means that the trigger will require all conditions to be true before it passes an event.

L1 items can also be added into the trigger string. If they aren't then a default L1 item is used. For the $E_{\mathrm{T}}^{\mathrm{miss}}$ trigger the L1 item is always explicitly stated. When used in a HLT name the underscore is removed from the L1 item. So for example `L1_XE50` becomes `L1XE50`.

Finally all HLT triggers must begin with the string `HLT`. So the trigger `HLT_xe110_mht_xe70_L1XE50` would only pass an event in which the L1 item `L1_XE50` had passed the event, $E_{T,\texttt{cell}}^{miss} > 70$ GeV and $E_{T,\texttt{mht}}^{miss} > 110$ GeV.

4.5 Performance metrics

4.5.1 Efficiency

From a physics analysis perspective the most important property of a trigger is its efficiency in an analysis selection. The efficiency for a given trigger in a given event selection is defined as the fraction of events passing the event selection that also pass the trigger

$$\epsilon = \frac{\mathrm{N(trigger\,\&\&\,event\,selection)}}{\mathrm{N(event\,selection)}}$$

This is often displayed as a function of some reference parameter. For the $E_{\mathrm{T}}^{\mathrm{miss}}$ trigger this is typically the offline reconstructed $E_{\mathrm{T}}^{\mathrm{miss}}$ (with muons subtracted) or some suitable proxy. These are then referred to as 'turn on' curves. For these plots the value in each bin is the efficiency for that event selection for a reference parameter value that falls *in* that bin. Sometimes cumulative efficiency turn on curves are shown instead, in these cases the value in each bin is the efficiency for that event selection for a reference parameter value that falls *in or above* that bin.

4.5.1.1 Signal models

Several toy models are used to study the efficiency of the $E_{\mathrm{T}}^{\mathrm{miss}}$ trigger. All of the selections described here use a logical OR of lepton triggers (of the relevant flavour). Signals with two leptons use an OR of single and di-lepton triggers. This ensures an unbiased selection for studying the trigger efficiency. Unless otherwise stated all leptons are required to pass 'gradient' isolation selection and medium ID quality cuts (see section 3.5).

$W \to \mu\nu/W \to e\nu$: These selections target the production of W bosons. In order to get a large enough $E_{\mathrm{T}}^{\mathrm{miss}}$ this production has to be in association with a jet (e.g. recoiling against ISR) but no explicit selection is made on this. The selections are as follows:

- Require any single electron (muon) trigger to have fired
- Exactly one electron (muon) and no muons (electrons)
- $m_T > 50$ GeV (equation 2.4).

The m_T selection is sometimes omitted as it can bias the reference $E_{\mathrm{T}}^{\mathrm{miss}}$ distribution at low values of $E_{\mathrm{T}}^{\mathrm{miss}}$. Usually this isn't a concern as we are more focused on the higher $E_{\mathrm{T}}^{\mathrm{miss}}$ region.

$Z \to \mu\mu/Z \to ee$: These selections target the production of Z bosons. As with the W this is usually in association with a jet but no explicit selection is made on this. $Z \to \mu\mu$ is a very clean signal in the $E_{\mathrm{T}}^{\mathrm{miss}}$ trigger as the muons deposit very little energy in the calorimeters. We can also use the reconstructed p_T of the Z boson as a proxy for the 'true' $E_{\mathrm{T}}^{\mathrm{miss}}$ in the event which also allows us to avoid any effects coming from the resolution of the offline $E_{\mathrm{T}}^{\mathrm{miss}}$. The selections are as follows:

- Require any single or di-electron (muon) trigger to have fired
- Exactly two electrons (muons) with opposite charge and no muons (electrons)
- $66.6\mathrm{GeV} < m_{ll} < 116.6\mathrm{GeV}$.

$t\bar{t}$: These selections target the pair production of top quarks. This can be a useful selection to look at in combination with those for weak gauge bosons above as it explicitly requires the presence of jets. This selection is split into three streams: $t\bar{t} \to b\bar{b}e\nu jj$, $t\bar{t} \to b\bar{b}\mu\nu jj$ and $t\bar{t} \to b\bar{b}e\nu\mu\nu$. The $e\mu$ channel is the only dilepton channel considered in order to remove the large background from lepton pair production, e.g. from Z/γ production.

For the single lepton channel we require:

- Any single electron (muon) trigger to have fired
- Exactly one electron (muon) and no muons (electrons)
- At least 4 jets, at least 2 of which are b-tagged.

For the dilepton channel we require:

- Any single electron or single muon trigger to have fired
- Exactly one electron and one muon of opposite charge
- At least 2 b-tagged jets.

$\mathrm{H} \to \mu/\mathrm{e}\,\mathrm{Inv}$: These selections are designed to test a signal phase space similar to the one used by the ATLAS BSM Higgs to invisible analysis group [121]. This selection targets events where a Higgs boson, produced via *vector boson fusion* (VBF), then decays either to neutrinos via a Z boson or to some invisible BSM particle. VBF is characterised by two energetic jets in the forward region of the detector and reduced jet activity in the central region. An additional lepton selection is added to allow the use of an orthogonal lepton trigger. We require:

- Any single electron (muon) trigger to have fired
- At least one electron (muon)
- Two jets
- - leading jet $p_T > 80$ GeV, subleading jet $p_T > 50$ GeV

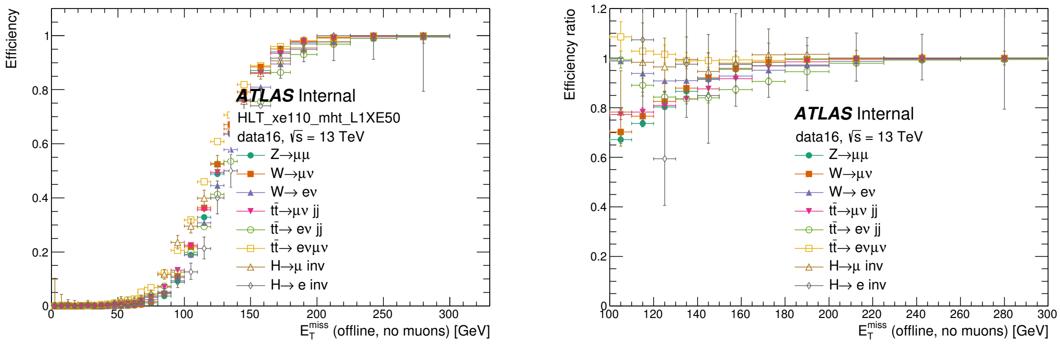

Figure 4.6: Left, the turn on curves (relative to the offline $E_{\mathrm{T}}^{\mathrm{miss}}$ with muons subtracted) for the trigger `HLT_xe110_mht_L1XE50` with various signal-like event selections. Right shows the ratio of the efficiency of a pure cell trigger with an equal rate to the efficiency of `HLT_xe110_mht_L1XE50`.

  - $\Delta\phi_{jj} < 1.8$
  - $\Delta\eta_{jj} > 4.9$

- Veto on any further jets with $p_T > 20$ GeV.

Figure 4.6 shows a comparison of the $E_{\mathrm{T}}^{\mathrm{miss}}$ trigger turn on for these various event selections. Also shown is the ratio between the efficiencies of `cell` and `mht` triggers with equal rates for the various selections. There is some selection dependence in the turn-on curves; they tend to be sharper, reaching full efficiency sooner in selections with more sources of 'true' $E_{\mathrm{T}}^{\mathrm{miss}}$ (e.g. neutrinos and muons) and worse in events with many jets. The important part of the turn on curve is the area around 200 GeV and here there is no difference between the different signal samples. Therefore for the most part the conclusions we can draw about the relative merits of different trigger strategies do not depend strongly on the chosen selection in which the efficiency is analysed. However, care needs to be taken to ensure that when optimising the trigger efficiency we do not improve the efficiency of one class of signals at the cost of another.

4.5.2 Rate

The rate is often the most stringent limitation placed on any given trigger, though for some slices and algorithms the CPU time to process events can also be a limiting factor. Therefore when comparing different algorithms it is important to make sure that the comparison is a fair one, i.e. that both triggers compared have similar rates. This is usually done using ‘equal rate thresholds’. First, a ‘target’ trigger is chosen and its rate calculated. Then for each other algorithm the threshold is chosen that produces the same rate as the target trigger. The trigger decisions for these equal rate thresholds can then be emulated and their efficiencies and turn ons calculated which allows for a more fair comparison between triggers. Note that the rate dependence on pile-up is different for different algorithms so these equal rate thresholds must be reevaluated at different pile-up thresholds.

Rate has an important impact on pile-up. As discussed in section 4.2.2 the trigger rate is dominated by object mismeasurement. This effect grows with pile-up; equations 4.3 and 4.4 show how the background trigger rates depend on the pile-up since $\sum E_T$ increases with pileup. This can result in large increases in rate which mean that the optimal trigger strategy depends strongly on the LHC running environment.

Rate can also be expressed as a cross-section, i.e. the total cross-section for processes that cause the trigger to fire. The conversion between cross-section and rate depends on the instantaneous luminosity at the time the cross-section was measured. There is a natural linear dependence on luminosity for all trigger rates since all processes become more likely with more luminosity. However, the trigger cross-section allows for this dependence and therefore all changes in the cross-section are due to the triggers’ sensitivity to pile-up.

When considering the overall rate cost of including a new trigger it is necessary to consider it in the context of all the other triggers that will be run. The limitation is on the total output rate of the trigger menu, not on the output rate of an individual trigger. Therefore we define a trigger’s unique rate to be the output rate at which *only* that trigger admits events to be written to disk.

4.5.3 Resolution

The resolution of an algorithm describes how accurately it calculates the 'true' $E_{\mathrm{T}}^{\mathrm{miss}}$ in an event. It corresponds to the σ parameter used in section 4.2.2. In general the resolution is calculated by constructing the distribution $E_{x,\mathrm{trigger}}^{\mathrm{miss}} - E_{x,\mathrm{true}}^{\mathrm{miss}}$ and fitting it to a Gaussian distribution. The resolution is then defined to be the width of this distribution. Given that some more complicated $E_{\mathrm{T}}^{\mathrm{miss}}$ calculations do not produce a mismeasurement distribution that is well modeled by a Gaussian distribution sometimes it is more convenient to calculate the resolution as the RMS of the $E_{\mathrm{x}}^{\mathrm{miss}}$ distribution, this also reduces the sensitivity to poor quality fits. This can also be calculated for $E_{\mathrm{y}}^{\mathrm{miss}}$ and it is expected (and found) that they agree. For events with no true $E_{\mathrm{T}}^{\mathrm{miss}}$ the $E_{\mathrm{T}}^{\mathrm{miss}}$ distribution can also be fitted to a Rayleigh distribution and the σ parameter of that distribution could also be used. The resolution is expected to vary as a function of ΣE_{T} and μ so this process must usually be done in slices of these variables. This dependency can also be parameterised (Equation 4.4) and this distribution can be fitted.
A difficulty arises since in most cases it isn't possible to know the 'true' $E_{\mathrm{T}}^{\mathrm{miss}}$ in an event. Monte Carlo simulations can be used in some cases. In data the offline $E_{\mathrm{T}}^{\mathrm{miss}}$ can be used and in the $Z \to \mu\mu$ selection the p_T of the Z boson is a good proxy for the true $E_{\mathrm{T}}^{\mathrm{miss}}$. The easiest approach however is to select events that are expected to have no true $E_{\mathrm{T}}^{\mathrm{miss}}$ such as $Z \to ee$ or ZeroBias events.

An algorithm with a low resolution can usually be understood to be performing well as it tends to model the true $E_{\mathrm{T}}^{\mathrm{miss}}$ in an event well. This therefore has an impact on the turn-on curve; an algorithm with a low resolution tends to have a sharper turn-on. An important caveat is that the scale of an algorithm is also important. When measured in events with no true $E_{\mathrm{T}}^{\mathrm{miss}}$ an algorithm which systematically underestimates the $E_{\mathrm{T}}^{\mathrm{miss}}$ value (like `cell` due to EM calibration) will appear to have a good resolution, however in events with real $E_{\mathrm{T}}^{\mathrm{miss}}$ the algorithm's resolution will be much worse.

4.5.4 Stability

Another important aspect of a trigger is its reliability. The efficiency of a trigger should ideally not depend on quantities that are irrelevant to analyses (e.g. pile-up, data taking period). Therefore another important performance metric for a trigger is its stability with respect to these variables. Typically the efficiency for a given trigger in a given event selection (including a cut on a proxy for the true $E_{\mathrm{T}}^{\mathrm{miss}}$) is plotted as a function of data taking period or pile-up. Ideally this line will be flat.

4.6 2015 studies

4.6.1 Algorithm performance comparisons

At the beginning of the 2015 run the performance of the various algorithms was not well known. During Run 1 the algorithm used was most similar to `cell` and though an algorithm similar to `tc_lcw` was run online it was not used as the primary trigger. The previous pile-up was also much lower, ranging to a maximum of around 15 rather than the maximum of 30 seen during 2015 [122]. A priority for the group during 2015 running was to use the lower pile-up environment to evaluate the performance of the various algorithms and design a trigger strategy for 2016 and beyond.

During 2015 $E_{\mathrm{T}}^{\mathrm{miss}}$ triggers based on all 5 of the algorithms were used; all had their lowest unprescaled threshold at 70 GeV and an `L1` threshold at 50 GeV. Triggers based on the `pueta` and `pufit` algorithms showed similar or very slightly worse performance compared to those based on the `tc_lcw` algorithm so those algorithms are excluded from the following discussion. Figure 4.7 shows the efficiencies of these triggers in a $Z \to \mu\mu$ selection. Also shown are the efficiencies for triggers with equal rates (section 4.5.2). Figure 4.8 shows the rates of the lowest unprescaled triggers. The key plot for this is the right hand plot of figure 4.7. This shows that when the thresholds are adjusted to ensure that the triggers have equal rates the efficiencies of the topocluster based algorithms (`mht` and `tc_lcw`) clearly out perform the `cell` algorithm. All the triggers reach plateau by $p_T(Z) = 180$ GeV but the efficiency of `mht` and `tc_lcw` are much greater within the turn on.

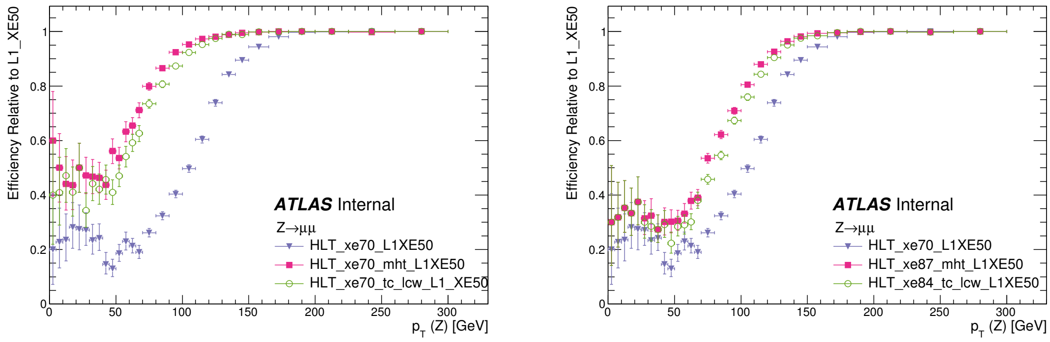

Figure 4.7: The efficiency in a $Z \to \mu\mu$ preselection for triggers based on a variety of algorithms. On the left the triggers are chosen to have an equal threshold (70 GeV). This was the threshold used online during this data taking period. On the right they are chosen to have an equal rate to `HLT_xe70_L1XE50` (the L1 trigger `L1_XE50` is kept the same, HLT decisions were emulated).

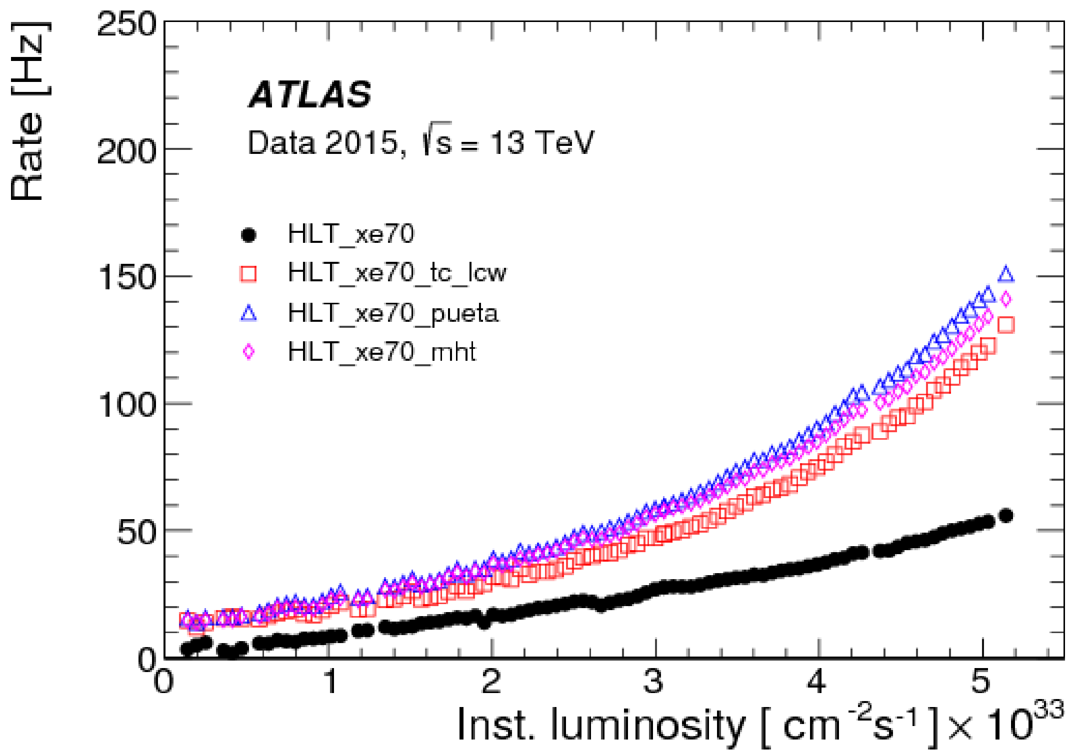

Figure 4.8: The rates of the baseline triggers in 2015 data taking as a function of the instantaneous luminosity. Figure taken from reference [3].

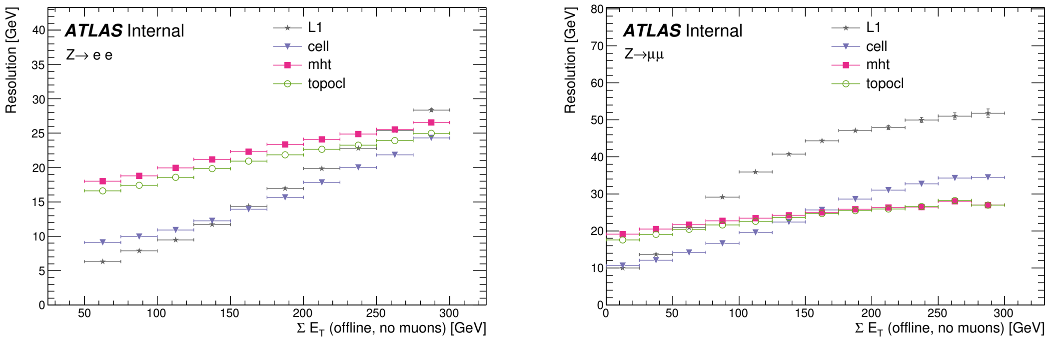

(a) $Z \to ee$ **(b)** $Z \to \mu\mu$

Figure 4.9: The resolution (defined in section 4.5.3) for each of the HLT trigger algorithms in $Z \to ee$ events (left) and in $Z \to \mu\mu$ events (right). In the $Z \to \mu\mu$ event selection the resolution is fitted to the different between the algorithm $\vec{\boldsymbol{p}}_{\mathrm{T}}^{\mathrm{miss}}$ and the transverse momentum of the reconstructed Z candidate.

Figure 4.9 shows the algorithm resolutions. In the $Z \to ee$ selection the resolutions of the `cell` and `L1` algorithms appear much better than those of the `mht` and `tc_lcw` algorithms, however this is mainly because of the difference in the calibration scale of the algorithm. As figure 4.5 shows, these algorithms tend to underestimate the $E_{\mathrm{T}}^{\mathrm{miss}}$ which causes the low values of resolution seen. This is more clear in the $Z \to \mu\mu$ selection in figure 4.9b where the resolution is constructed from the difference between the measured $\vec{\boldsymbol{p}}_{\mathrm{T}}^{\mathrm{miss}}$ and the 'true' $\vec{\boldsymbol{p}}_{\mathrm{T}}^{\mathrm{miss}}$ in the event (in this case the reconstructed $\vec{\boldsymbol{p}_T}$ of the Z boson). In this figure we see that the resolution of the `L1` algorithm quickly grows past the topocluster based algorithms and by around 150 GeV `cell` has also grown larger. From this we can also see that the topocluster based algorithms outperform `cell`. Figure 4.10 shows the stability of the trigger algorithms as a function of pileup. All of them show good stability over this pile-up range. Based on these studies it was decided to devote most of the available rate budget for the HLT $E_{\mathrm{T}}^{\mathrm{miss}}$ signature to the topocluster based signatures. Given the small difference in performance between `mht` and `tc_lcw` it was decided to run `tc_lcw` as the primary during 2016 as it was considered to be a simpler algorithm. The primary trigger that was chosen was `HLT_xe80_tc_lcw_L1XE50` with a backup trigger of `HLT_xe90_mht_L1XE50`.

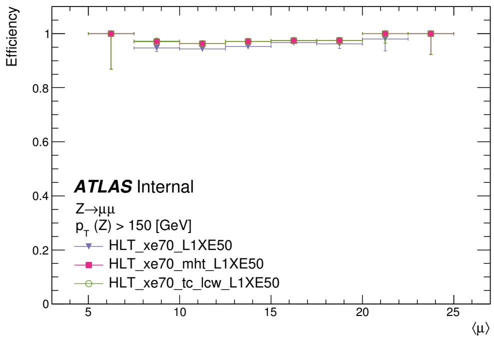

Figure 4.10: The stability of the trigger efficiency (for a fixed threshold of 70 GeV and offline selection as defined in section 4.5.4) for the HLT $E_{\mathrm{T}}^{\mathrm{miss}}$ algorithms during 2015 running as a function of pile-up.

4.7 2016 studies

4.7.1 Differences to 2015

The most substantial difference between 2015 and 2016 running was the pile-up. As shown in figure 4.2 the average pile-up almost doubled between the two years. Two other changes are relevant for the $E_{\mathrm{T}}^{\mathrm{miss}}$ trigger. The L1 Calo filters (cuts on the trigger towers designed to suppress electronic and pile-up noise) were updated to allow for the higher pile-up environment. New filters were also set later on during the year[6]. The trigger also benefited from changes to the HLT calo topocluster calibrations which were modified to include corrections for the earliest bunches in the train.

4.7.2 Rate behaviour with pile-up

Early in the 2016 run it became clear that the chosen triggers' rates far exceeded the allowed budget for the $E_{\mathrm{T}}^{\mathrm{miss}}$ slice; they showed an exponential dependence on the pile-up. The reason for this dependence can be seen by looking back at equation 4.3. The resolution σ grows with pile-up (equation 4.4) and larger values of resolution clearly give higher rates for a given threshold. However this effect was far stronger than expected for the topocluster based algorithms.

[6]On 26/07/2016 at the beginning of period G.

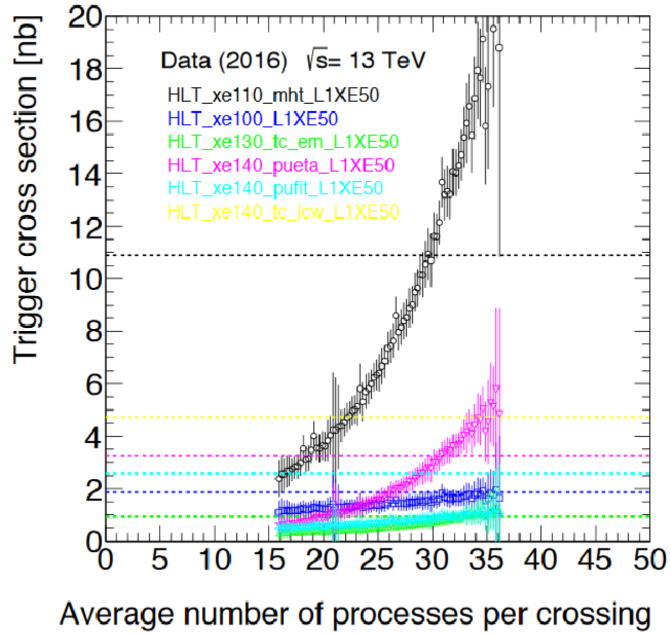

Figure 4.11: The trigger cross-section for a few different $E_{\mathrm{T}}^{\mathrm{miss}}$ triggers run during 2016. The `mht` trigger (which has the lowest effective threshold) has a very strong dependence on pile-up. This plot was produced by a collaborator.

The `tc_lcw` trigger at 80 GeV was removed and over the next few months of running the threshold of the `mht` trigger increased in steps to 110 GeV. Figure 4.11 shows the pile-up dependence of the cross-section of this trigger along with the cross-sections of triggers based on the other algorithms. Even at this threshold the trigger rate was worryingly high, certainly stretching the slice's budget if not outright exceeding it. However, simply increasing the threshold further would threaten the efficiency of the trigger in analysis group signal regions. Therefore a large campaign was launched to bring these rates under control. Figure 4.12 shows the efficiencies of `cell`, `mht` and `tc_lcw` triggers with equal rates for two different pile-up slices. The same `cell` trigger is shown in each plot with the thresholds placed on the other two algorithms adjusted to give an equal rate to the `cell` trigger in each case. Even in the higher pile-up environment the performance of `mht` and `cell` become similar which meant that it was not possible to simply switch algorithms to `cell`. The impact of pile-up on `tc_lcw` is also far greater than it is on `mht`. This can be seen by high threshold (114 GeV) and the accompanying much lower efficiency in the right hand plot. This is likely due to the fact that

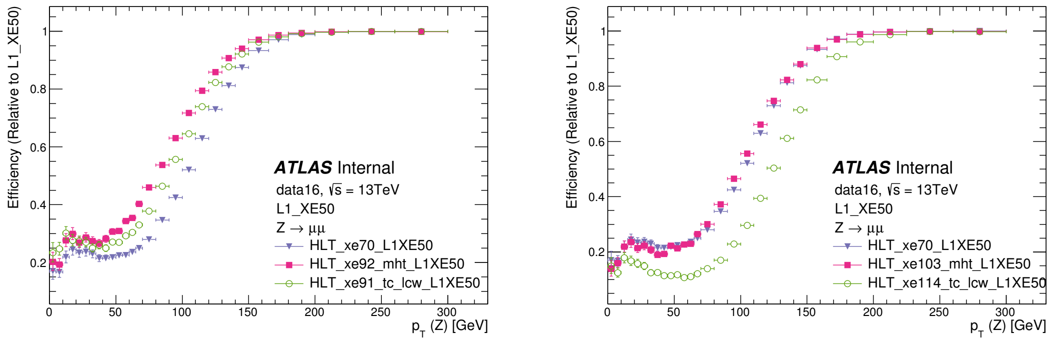

Figure 4.12: The efficiency in a $Z \to \mu\mu$ preselection for the `mht`, `cell` and `tc_lcw` algorithms with a `L1` threshold of 50 GeV. The pure `cell` trigger `HLT_xe70_L1XE50` is used as a baseline and the thresholds of the other two algorithms are modified to give an equal rate to this trigger. This is done in two separate bins of pile-up: $\langle\mu\rangle < 25$ (left) and $\langle\mu\rangle > 25$ (right). The pile-up thresholds are chosen to cover the upper and lower half of the pile-up distribution. In the lower pile-up bin thresholds of 92 GeV and 91 GeV are used for the `mht` and `tc_lcw` algorithms respectively. In the higher pile-up bin the corresponding thresholds are 103 GeV and 114 GeV.

`tc_lcw` has no explicit pile-up rejection whereas the jets in the `mht` algorithm have had some area based pile-up subtraction applied to them.

4.7.3 Combined `cell` + `mht` trigger

One conclusion which we can draw from figure 4.12 is that while the `cell` trigger overall has a lower efficiency than `mht` it is much more pile-up resilient. This can be seen as the threshold required for `mht` to match the rate of `HLT_xe70_L1XE50` increases from 92 GeV for $\langle\mu\rangle < 25$ to 103 GeV for $\langle\mu\rangle > 25$ with a corresponding reduction in efficiency. One solution to the `mht` rate crisis was therefore to try a combined trigger; a trigger which combined cuts on both the `cell` *and* `mht` algorithms. The rational was fairly simple. The `mht` trigger shows good efficiency but a very poor behaviour of its rate with pile-up, whereas the `cell` trigger showed poor efficiency but strong pile-up rejection. Therefore with suitably chosen thresholds it should be possible to construct a trigger which showed good efficiency and good pile-up rejection. This works because the mismeasurements made by the different algorithms are relatively uncorrelated (jets and calorimeter cells being quite different objects) so when there is no real $E_{\mathrm{T}}^{\mathrm{miss}}$ it is less likely that both algorithms

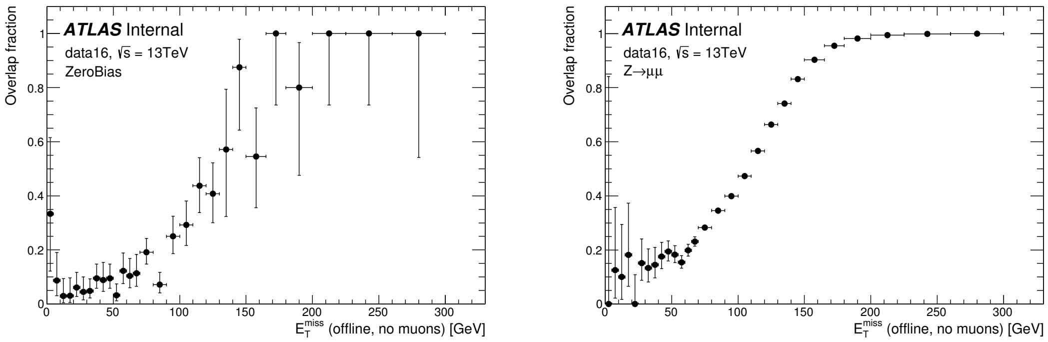

Figure 4.13: The overlap of the `HLT_xe110_mht_L1XE50` and `HLT_xe70_L1XE50` triggers on the ZeroBias dataset (left) and in a $Z \to \mu\mu$ preselection (right).

will measure a high enough $E_{\mathrm{T}}^{\mathrm{miss}}$ to pass the trigger. When real $E_{\mathrm{T}}^{\mathrm{miss}}$ is present however, both algorithms will detect it and therefore will be more correlated.

Figure 4.13 shows the overlap of two triggers, one pure `mht`, the other pure `cell`. Overlap is defined as

$$\mathrm{Overlap} = \frac{\mathrm{N(pass\,trigger\,1\,\&\&\,pass\,trigger\,2)}}{\mathrm{N(pass\,trigger\,1\,||\,pass\,trigger\,2)}}$$

We can see that indeed at low values of $E_{\mathrm{T}}^{\mathrm{miss}}$ the two triggers are much less correlated, with an overlap of less than 10% in background events with offline measured $E_{\mathrm{T}}^{\mathrm{miss}}$ less than 50 GeV in the ZeroBias sample. In a signal like sample however, the overlap is almost 1 at 200 GeV (where most analysis groups begin to have their offline cuts). This means that there is a potentially large scope for reducing rate with minimal efficiency loss.

Figure 4.14 shows efficiency vs. rejection curves for a selection of trigger strategies. We can see that the combined triggers almost always outperform the pure triggers. The almost vertical sections of these lines show the rate reduction that you can get almost ‘for free’, i.e. with only minimal efficiency loss. We can also see that the crossing points of these various strategies (which show which should be favoured for a target rate) are strongly pile-up dependent; at higher pile-up higher `cell` thresholds are favoured. In fact, in the higher pile-up plot we can see that the performance of the `cell` and `mht` triggers are very similar suggesting that sooner or later `cell` would begin to beat `mht`. Based on these studies we were able

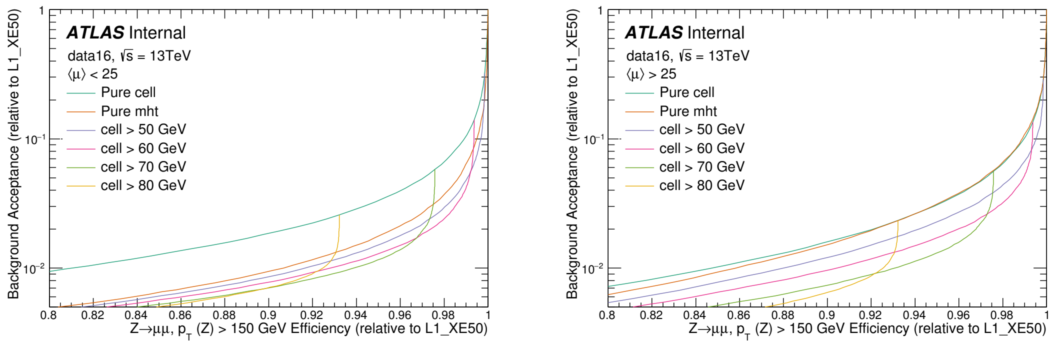

Figure 4.14: ROC curves are shown for various options for combined `mht` and `cell` triggers. Shown are curves corresponding to pure `mht` and `cell` triggers and also triggers with a fixed `cell` threshold and variable `mht` threshold. For all curves the thresholds are allowed to vary in 1 GeV steps from 0 to 110 GeV. The ROC curves are derived for two different pile-up conditions, $\langle\mu\rangle < 25$ (left) and $\langle\mu\rangle > 25$ (right).

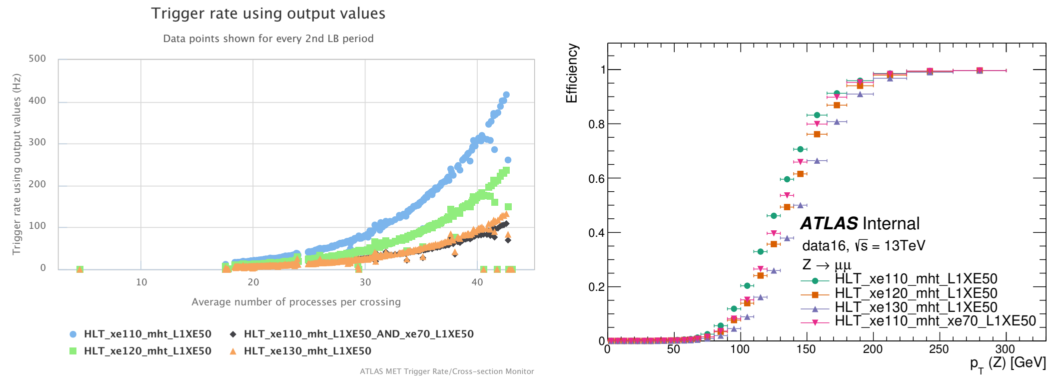

Figure 4.15: The trigger rates for four $E_{\mathrm{T}}^{\mathrm{miss}}$ triggers are shown along with a comparison of their efficiencies. While rate behaviours of `HLT_xe130_mht_L1XE50` and `HLT_xe110_mht_xe70_L1XE50` are similar the efficiency of the latter is clearly higher. The left hand plot was produced using a collaborator's tool.

to recommend a new trigger `HLT_xe110_mht_xe70_L1XE50` which corresponds to a threshold of 110 GeV on the `mht` algorithm and a threshold of 70 GeV on the `cell` algorithm. Figure 4.15 shows the rate and efficiency of this trigger compared to pure `mht` triggers. We can see that the turn-on curve is sharper than the pure `mht` triggers and it has only a small efficiency loss compared to the pure `mht` trigger `HLT_xe110_mht_L1XE50` at high values of $p_T(Z)$. With this small efficiency loss we see an enormous rate gain of between a factor of 3 and 4. Physics analysis groups were also asked to evaluate the efficiency of these different triggers in their analysis signal regions and they reported similar results to those shown here.

This strategy also had a few other significant advantages over other options

- All events passing it were necessarily a subset of the events passing `HLT_xe110_mht_L1XE50`. This means that all the events that would have passed the trigger before it was implemented (had it been online) had been recorded anyway.
- Emulating it offline required only information that already existed in the analysis datasets and so did not require a substantial reprocessing effort.

This trigger was activated during several late 2016 runs when the luminosity grew too high to support the rate of `HLT_xe110_mht_L1XE50`.

4.7.4 Use of the trigger in analysis

The $E_{\mathrm{T}}^{\mathrm{miss}}$ trigger is a vital part of the ATLAS physics program. The triggers described here were used to take data used for analyses covering many diverse areas. Examples include searches for SUSY, both strongly [123, 124] and weakly [125] produced, searches for other exotic signatures, such as vector-like quarks [126], high mass resonances [127] and dark matter [128] as well as Standard Model measurements such as searches for $H \to b\bar{b}$ decays [129].

As the $E_{\mathrm{T}}^{\mathrm{miss}}$ trigger reaches 100% efficiency at its plateau many analyses are able to work in this regime, removing the need for scale factors to allow for differences in modelling between data and Monte Carlo. Some analyses, such as the $H \to b\bar{b}$ search mentioned above, however need to work in the turn on region. In these cases dedicated scale factors must be derived to correct for differences between data and simulation. This scale factors must typically be derived on a case-by-case basis as they may be topology dependent.

4.8 Conclusion

The ATLAS $E_{\mathrm{T}}^{\mathrm{miss}}$ trigger in Run 2 of the LHC has been discussed. The good performance of this trigger is vital for many analyses searching for evidence of new physics, particularly for those searching for possible dark matter candidates. Various metrics which can be used to assess the trigger's performance have been presented, along with studies measuring these in order to compare several possible trigger strategies. These studies were used to form the ATLAS $E_{\mathrm{T}}^{\mathrm{miss}}$ trigger strategy for 2016.

Due to the larger than expected rates in 2016 this strategy was then revisited. A new technique of combining the decisions from multiple different trigger algorithms was presented. This technique takes advantage of the tendency of the measurements of these algorithms to be uncorrelated in events when little $E_{\mathrm{T}}^{\mathrm{miss}}$ is present, but correlated in the presence of large true $E_{\mathrm{T}}^{\mathrm{miss}}$and is shown to reduce rates by a factor of almost 4 without greatly impacting on analysis efficiencies. The use of combined triggers continues to be a vital part of the ATLAS $E_{\mathrm{T}}^{\mathrm{miss}}$ trigger strategy and will likely continue to be as LHC conditions become more challenging in the future.

5
Multijet Analysis

Contents

5.1 Statement of original work

The work presented in this chapter was performed as part of an analysis team. I wrote and maintained a software framework which took the reconstructed detector data (section 3.5), performed the object calibrations and selections (section 5.4.1) and the event selections (section 5.4.2) and allowed for the plotting of all analysis quantities. This framework was used to process all of the data used in this analysis, both from the ATLAS detector and from simulation. An additional piece of software written by a collaborator was used to combine the produced plots into canvases and to perform the statistical fit (section 5.6). I also contributed through studies into trigger efficiencies, for example figure 5.4. The entirety of section 5.8 is my own work. Where I did not produce a figure directly this has been noted in that figure's caption.

5.2 Introduction

The analysis aims to target a fairly general final state with large numbers of jets, no leptons and large $E_{\mathrm{T}}^{\mathrm{miss}}$. We took care to keep these selections as general as possible to allow easy re-interpretation of our results. This means the results can be used by others (e.g. in reference [130]) to test new theories or to extend our interpretations to models that we didn't consider.

The analysis was published as a paper [2] and was an extension to a previous paper [1] produced using only data taken in 2015 to which the author also contributed. Data from two years of LHC collisions was considered in this analysis. During 2015 good quality data comprising a total integrated luminosity of $3.21 \pm 0.07\,\mathrm{fb}^{-1}$ was recorded. During 2016 a further $32.9 \pm 1.1\,\mathrm{fb}^{-1}$ was recorded. Reference [93] describes the techniques used to measure luminosity.

5.2.1 Analysis motivation

In RPC SUSY models states with an R-parity of -1 (i.e. containing an odd number of sparticles) can only decay to states which also have an R-parity of -1. Models where gluinos are produced in LHC collisions can therefore cascade through multiple

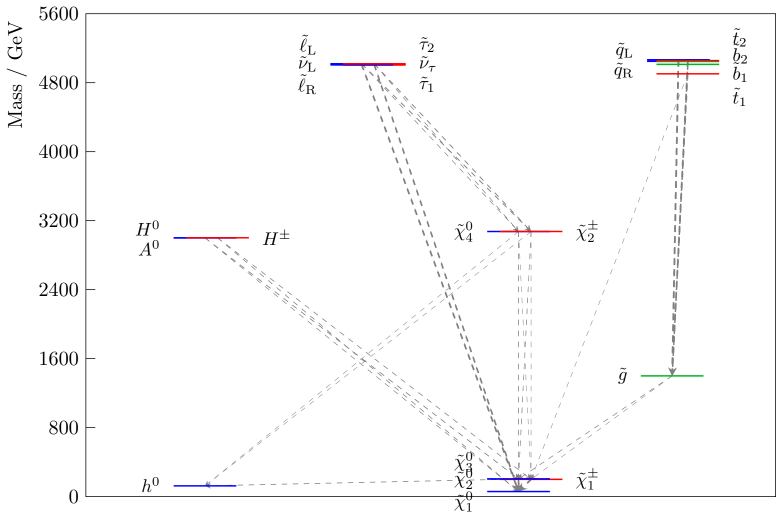

Figure 5.1: The SUSY mass spectrum for a pMSSM benchmark model used in this analysis. Possible decays are shown with dashed arrows. The thickness of the line corresponds to the branching ratio of the decay and only decays with a branching ratio greater than 10% are shown. This figure was created using the software described in Ref. [131].

intermediate R-parity$= -1$ particles which can result in a large number of decay products in the final state in addition to the LSP. This can lead to final states with very high multiplicities of energetic objects and moderate amounts of $E_{\mathrm{T}}^{\mathrm{miss}}$ which are rare in the Standard Model.

An example model spectrum is shown in figure 5.1 which may produce events corresponding to the pseudo-Feynman diagram shown in figure 5.2b. In this model gluinos can decay through an electroweakino which subsequently decays to the LSP. These decays also produce other particles such as quarks and gauge bosons. Heavy quarks and gauge bosons will also decay further. This often results in final states with large numbers of jets.

A prime motivation for SUSY models is to provide a dark matter candidate. If such a particle is produced in an LHC collision then $E_{\mathrm{T}}^{\mathrm{miss}}$ is a natural consequence. However, as discussed in chapter 4, analyses relying on the $E_{\mathrm{T}}^{\mathrm{miss}}$ trigger will be limited to offline $E_{\mathrm{T}}^{\mathrm{miss}}$ thresholds of at least 200 GeV which limits their sensitivities to certain models. By targeting states with large numbers of jets the multijet analysis is able to use a multijet trigger which allows us to pick an offline $E_{\mathrm{T}}^{\mathrm{miss}}$

threshold which is not limited by the trigger. This gives us sensitivity to models to which analyses dependent on the $E_{\mathrm{T}}^{\mathrm{miss}}$ trigger would be insensitive.

5.2.2 Benchmark signal models

Even though a wide range of models is targeted it is still useful to optimise cuts with respect to some signal models so long as one does not optimise too much towards any one particular sample. This allows selection on common characteristics of many SUSY models and other BSM scenarios which exhibit those same characteristics. The search was optimised using four models. Pseudo-Feynman diagrams are shown for these in figure 5.2.

These models contain free parameters, e.g. sparticle masses, which are varied to form a two-dimensional 'signal grid' of individual model points. Monte Carlo datasets are created for each point and the numbers of events from the simulated processes expected to pass the analysis selections are calculated. These are then used in the statistical fit 5.6 to evaluate the exclusion limits in those models. For example, in the case of no significant excesses being measured the significance of the exclusion of each model point is calculated. This is then interpolated across the grid to calculate the exclusion limits.

Two-step (Fig. 5.2a)

In this simplified model the only accessible SUSY particles are the $\tilde{g}$, $\tilde{\chi}_1^{\pm}$, $\tilde{\chi}_2^0$ and the $\tilde{\chi}_1^0$. The decays to Standard Model particles are fixed and the decay path is as follows

$$\begin{aligned} \tilde{g} &\to \tilde{\chi}_1^{\pm} + q + \overline{q}', (\mathrm{q} = \mathrm{u, d, s, c}) \\ \tilde{\chi}_1^{\pm} &\to \tilde{\chi}_2^0 + W^{\pm} \\ \tilde{\chi}_2^0 &\to \tilde{\chi}_1^0 + Z, \end{aligned}$$

where the first decay proceeds via an off-shell squark. The 2-dimensional signal grid used for the presentation of results is formed by allowing the masses of the gluino and LSP to vary. The masses of the remaining two particles are fixed so that they lie halfway between the masses of their parent particles and the LSP. That is, $m_{\tilde{\chi}_1^{\pm}} = {}^{(m_{\tilde{g}} + m_{\tilde{\chi}_1^0})}/_2$ and $m_{\tilde{\chi}_2^0} = {}^{(m_{\tilde{\chi}_1^{\pm}} + m_{\tilde{\chi}_1^0})}/_2$.

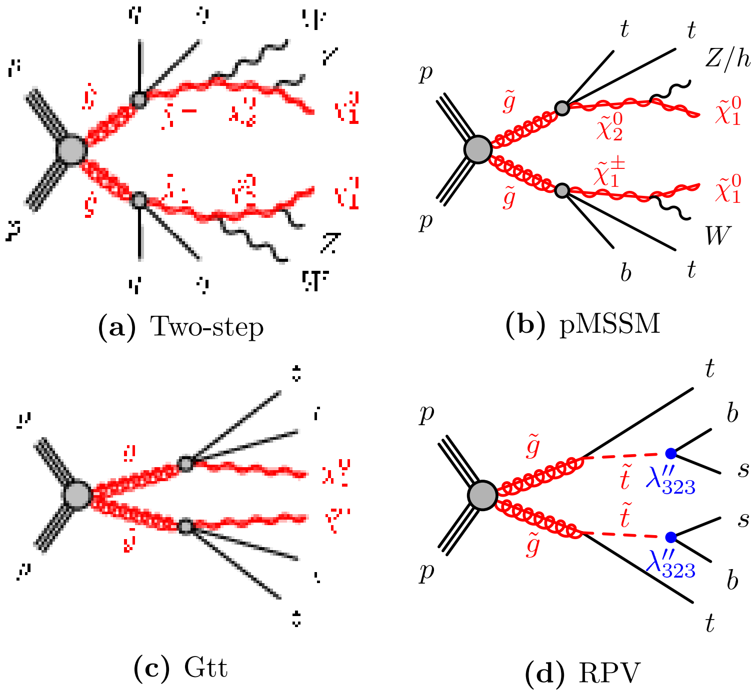

(a) Two-step **(b)** pMSSM

(c) Gtt **(d)** RPV

Figure 5.2: Pseudo-Feynman diagrams for four signal types targeted by this analysis. These signal points are used to optimise analysis cuts as well as to interpret the results in the form of exclusion plots. The leading order diagrams for gluino pair-production are shown in figure 5.3.

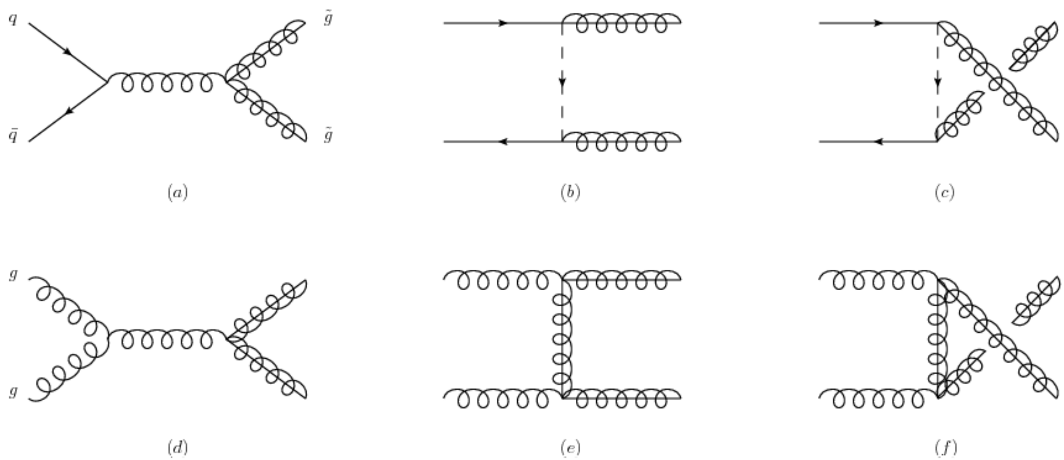

Figure 5.3: Leading order Feynman diagrams for gluino pair-production, taken from reference [132].

pMSSM (Fig. 5.2b)

This grid is a set of pMSSM model points inspired by the results of Ref. [79], designed to not be excluded by other means and to lie in an area of phase space to which this analysis is uniquely sensitive. That paper found that a class of models existed that were only excluded by the Run 1 version of this analysis so this grid was designed to focus on similar, unexcluded models. As seen in figure 5.1 relatively few other SUSY particles have lower masses than the $\tilde{g}$, limiting its possible decays. In this model slice the only accessible SUSY particles are those of two of the electroweakino multiplets: a Higgsino-dominated intermediate mass multiplet and a bino dominated LSP. The grid is formed by varying two of the SUSY soft-breaking parameters, M_3 and μ, which are strongly correlated to the gluino mass and the masses of the Higgsinos respectively. The mass of the bino LSP is strongly correlated to M_1 which is set to 60 GeV. The other parameters are set to $m_A = M_2 = 3$ TeV, $A_\tau = 0$, $\tan\beta = 10$, $A_t = A_b = m_{(\tilde{e},\tilde{\mu},\tilde{\tau})(L,R)} = m_{\tilde{q}L(1,2,3)} = m_{(\tilde{u},\tilde{c},\tilde{t})R} = m_{(\tilde{d},\tilde{s},\tilde{t})R} = 5$ TeV. These choices ensure that the dominant decays are the ones in which we are interested and also ensure that the Higgs mass is close to 125GeV.

Unlike in the simplified models, the branching ratios are not fixed for a particular decay path, or even a limited set. Instead the dominant decays vary, largely driven by the difference between M_3 and μ. When this difference is large ($M_3 \gtrsim 1200$ GeV, $\mu \lesssim 500$ GeV) the decay is dominated by the decay paths shown in figure 5.2b. As the gluino mass decreases and/or the masses of the Higgsinos increase the gluino decay becomes dominated by the decay via an off-shell squark $\tilde{g} \to qq\tilde{\chi}_1^0$ (where q here refers to a light quark) and the multijet analysis becomes loses sensitivity as the final state contains only 4 jets.

Gtt (Fig. 5.2c)

In this simplified model only the $\tilde{\chi}_1^0$ has a lower mass than the gluino which decays with a branching ratio of unity to $t\bar{t} + \tilde{\chi}_1^0$ via an off-shell top squark. The grid is formed by varying the masses of the gluino and the $\tilde{\chi}_1^0$. The kinematics of this model are largely insensitive to the top squark mass, so long as it remains heavier than the gluino and sufficiently lighter than the other squarks.

RPV (Fig. 5.2d)
In this simplified model R-parity is no longer conserved. This allows the top squark to decay via a baryon-number-violating vertex to a bottom quark and a strange quark. In this scenario the LSP is not stable so the true $E_{\mathrm{T}}^{\mathrm{miss}}$ is low, coming from semi-leptonic b decays. This means that many SUSY searches have no sensitivity. However, the present search retains sensitivity as it is able to select events with lower $E_{\mathrm{T}}^{\mathrm{miss}}$ values.

5.3 Experimental signatures and Standard Model backgrounds

5.3.1 Signatures of targeted models

The cross-sections of the beyond-standard-model processes which we are targeting are predicted to be much smaller than those of many Standard Model processes. Hence, it is necessary to select kinematic regions which would be rich in signal events but with comparatively few background events. We can use our benchmark models as well as generic features of the targeted models to guide our selections while still remaining sensitive to a broad range of processes. We target models with long decay chains including the production of stable, weakly interacting massive particles therefore all of our models will feature high jet multiplicities as well as moderate quantities of $E_{\mathrm{T}}^{\mathrm{miss}}$.

From the results of previous searches [79] we expect that gluinos should have a mass of at least 1 TeV. These high masses mean that the particles produced at the start of the decay chain tend to be produced with low velocities in the centre of mass frame and therefore their decay products are produced mostly in the central region of the detector. In comparison, the most massive particle in the Standard Model is the top quark with a mass of approximately 170 GeV. Standard Model particles are therefore preferentially produced with higher boosts and, given that the propagators of t and u channel production favour forward production, Standard Model processes are more likely to produce jets in the forward region than those predicted by SUSY models. This motivates selecting events with jets in the central region of the detector.

Inspecting the benchmark models we can see that most of them feature production of large numbers of t and b quarks. This is because constraints from the Higgs boson mass require loop corrections including a light top squark, and the corresponding constraints for the other squarks are far weaker, so the $\tilde{t}$ features in many SUSY decays. Given that t quarks decay almost exclusively to b quarks this results in states with large numbers of b-jets which are rare in the Standard Model.

The decay chains often feature the production of heavy Standard Model particles, either t quarks as described above or bosons produced in decays between different electroweakino states. In contrast Standard Model multijet events tend to be largely from additional quarks and gluons in the matrix element with few heavy particles. Using reclustered jets (section 3.5.2.3) we can attempt to reconstruct the decays of these heavier objects. We expect to find higher masses among these reclustered jets in SUSY events than in QCD multijet events.

These last two points motivate forming two separate streams of the analysis called the 'flavour stream' and the 'mass stream' which use selections based on the number of b tagged jets and the total mass of reclustered jets respectively.

5.3.2 Signatures of Standard Model backgrounds

Invisible particles are rare in the Standard Model so selecting on $E_{\mathrm{T}}^{\mathrm{miss}}$ should remove much of the background. Events which would pass this selection mainly fall into to two categories: events with fake $E_{\mathrm{T}}^{\mathrm{miss}}$ due to mismeasurement and events with true $E_{\mathrm{T}}^{\mathrm{miss}}$ from neutrinos.

The determination of $E_{\mathrm{T}}^{\mathrm{miss}}$ was previously discussed in section 4.2.2. Equation 4.2 predicts that the probability for an event to have no true $E_{\mathrm{T}}^{\mathrm{miss}}$ but a measured $E_{\mathrm{T}}^{\mathrm{miss}}$ depends only on the width parameter σ which is the sum in quadrature of resolutions of the objects used to form the original $E_{\mathrm{T}}^{\mathrm{miss}}$ sum. In multijet events the resolution of the $E_{\mathrm{T}}^{\mathrm{miss}}$ is dominated by the jets. As shown in reference [133] for jets in the region $20 \leq p_T \leq 500$ GeV the stochastic ($b\sqrt{p_T}$) term dominates the resolution. This means that we can approximate the $E_{\mathrm{T}}^{\mathrm{miss}}$ resolution to be $\sigma = b\sqrt{H_{\mathrm{T}}}$ where H_{T} is the scalar sum of jet p_Ts[1]. This allows the construction of the ratio ($E_{\mathrm{T}}^{\mathrm{miss}}/\sqrt{H_{\mathrm{T}}}$) which gives a measure of how likely it is that a given measured $E_{\mathrm{T}}^{\mathrm{miss}}$ comes from invisible particles rather than from detector resolution effects. Selecting events with high $E_{\mathrm{T}}^{\mathrm{miss}}/\sqrt{H_{\mathrm{T}}}$ then allows us to remove more of the fake $E_{\mathrm{T}}^{\mathrm{miss}}$ background than a flat $E_{\mathrm{T}}^{\mathrm{miss}}$ selection would.

The significance $E_{\mathrm{T}}^{\mathrm{miss}}/\sqrt{H_{\mathrm{T}}}$ could be calculated using ΣE_{T}, the scalar sum over the transverse momenta of all measured objects, instead of H_{T}. However the modelling of this quantity is much more complicated, given that it has to allow for contributions from all soft particles in the event. Additionally, given the high jet multiplicities in the signal regions both the $E_{\mathrm{T}}^{\mathrm{miss}}$ and its resolution are dominated by jets, making H_{T} a suitable proxy.

Due to lepton number conservation neutrinos are only produced in the Standard Model in association with other neutrinos through the couplings to the Z boson or with charged leptons through couplings to the W boson. While the former case is an irreducible background to this analysis, the latter is greatly reduced by removing any events with reconstructed leptons.

5.4 Object and event selections

5.4.1 Object selections

Each event is reconstructed using the techniques described in section 3.5. The object definitions used in this reconstruction are those defined in table 5.1. Two sets of object definitions are used: baseline and signal. Baseline objects are used to compute overlap removal decisions and to calculate $E_{\mathrm{T}}^{\mathrm{miss}}$, whereas the signal objects have additional selection criteria and are used to define the event selections.

The $R = 0.4$ anti-k_t signal jets with $p_{\mathrm{T}} > 50$GeV used directly in the event selection are also reclustered using a second iteration of the anti-k_t algorithm with

[1] This is also a further approximation as the parameters of the resolution are also binned in $|\eta|$.

Object type	Selections
Baseline Electron	LooseBLayer ID [112] $p_{\mathrm{T}} > 10$ GeV $\lvert\eta\rvert < 2.47$
Signal Electron	Pass baseline overlap removal Tight ID [112] $p_{\mathrm{T}} > 25$ GeV 'GradientLoose' isolation [115] $d_0/\sigma_{d_0} < 5$ $z_0 < 0.5$mm
Baseline Muon	Medium ID [114] $p_{\mathrm{T}} > 10$ GeV $\lvert\eta\rvert < 2.7$
Signal Muon	Pass baseline overlap removal $p_{\mathrm{T}} > 25$ GeV 'GradientLoose' isolation [115] $d_0/\sigma_{d_0} < 3$ $z_0 < 0.5$mm
Baseline Photon	Tight ID [113] $p_{\mathrm{T}} > 25$ GeV $\lvert\eta\rvert < 2.37$
Baseline Jet	Medium JVT working point [109] $p_{\mathrm{T}} > 20$ GeV $\lvert\eta\rvert < 2.8$
Signal Jet	Pass baseline overlap removal $p_{\mathrm{T}} > 50$ or 80 GeV $\lvert\eta\rvert < 2.0$

Table 5.1: Summary table of the object definitions used in this analysis. The working points and their efficiencies are described in section 3.5.2. The baseline photon selection is used solely for overlap removal and $E_{\mathrm{T}}^{\mathrm{miss}}$ reconstruction.

a radius parameter $R = 1.0$ as described in section 3.5.2.3. This radius is chosen to capture the decay of more massive particles such as W and Z bosons and t quarks. We then define M_J^{Σ} as the sum over all the masses of the new reclustered jets which satisfy $p_{\mathrm{T}} > 100$ GeV and $|\eta| < 1.5$.

5.4.2 Event selections

Selections are used to divide the data into several kinematic regions which form four separate categories: *template*, *signal*, *control* and *validation*. Signal regions are designed to have only small populations of events from Standard Model processes but to be rich in signal events. Control regions are designed to be dominated by events from specific backgrounds, in order to test and normalise the predictions of Monte Carlo. Template and validation regions are designed to be dominated by Standard Model multijet production; the former are used to predict the contribution of Standard Model multijet production to the signal regions, the latter to provide an assessment of the uncertainty associated to that prediction. The control, template and validation regions will be described in more detail in section 5.5.

The signal regions veto events containing baseline electrons or muons to reduce contributions from Standard Model backgrounds containing true $E_{\mathrm{T}}^{\mathrm{miss}}$. They all also require $E_{\mathrm{T}}^{\mathrm{miss}}/\sqrt{H_{\mathrm{T}}} > 5$ GeV$^{-1/2}$ to select events with large true $E_{\mathrm{T}}^{\mathrm{miss}}$ but trying to reduce contributions from events whose $E_{\mathrm{T}}^{\mathrm{miss}}$ is mismeasured. As the signal models we target feature long decay chains we require high jet multiplicities. As the number of measured signal jets will vary between points in our signal grids we define a variety of inclusive selections on jet multiplicity. The regions are also split into two streams; the flavour stream selecting on the number of b-jets and the mass stream selecting on the M_J^{Σ} variable.

For the flavour stream two different jet thresholds are used to define the multiplicity: 50 and 80 GeV, using the 6 and 5 jet triggers respectively. The 50 GeV threshold is associated with 4 inclusive multiplicity thresholds: running from 8 to 11. The 80 GeV threshold is associated with 3 inclusive multiplicity thresholds: running from 7 to 9. Each of these regions is further split requiring at least one or two b-tagged jets as well as regions without any b-jet requirement. The mass stream only uses the 50 GeV jet thresholds and multiplicity selections from 8 to 10. These regions are then further split by requiring M_J^{Σ} of at least 340 or 500 GeV. This leads to $(4 + 3) \times 3 = 21$ regions in the flavour stream and $2 \times 3 = 6$ regions in the mass stream. The signal regions are summarised in table 5.2 and the selections motivated in section 5.3.

The control regions (table 5.3) are designed to be rich in background events while still remaining kinematically close to the signal regions. In order to reduce statistical uncertainties the selection on n_{jets} is relaxed by 1. The lepton is also

	Flavour Stream		Mass Stream
Lepton Veto	No baseline e or μ remaining after overlap removal		
Jet η	< 2.0		
Trigger Jet p_T n_{jets}	`HLT_6j45_0eta240` > 50 GeV $\geq \{8, 9, 10, 11\}$	`HLT_5j70` > 80 GeV $\geq \{7, 8, 9\}$	`HLT_6j45_0eta240` > 50 GeV $\geq \{8, 9, 10\}$
n_{bjets} M_J^Σ	$\geq \{0, 1, 2\}$ No selection		No selection $\geq \{340, 500\}$ GeV
$E_{\text{T}}^{\text{miss}}/\sqrt{H_{\text{T}}}$	> 5 GeV$^{1/2}$		

Table 5.2: Summary table of the selections used to define the signal regions used in this analysis.

Lepton Multiplicity	Exactly one signal e or μ remaining after overlap removal
Lepton p_T	> 20 GeV
m_T	< 120 GeV
Trigger	Same as SR
Jet $p_T, \lvert\eta\rvert$	Same as SR
n_{jets}(including lepton)	$n_{\text{jets}}^{SR} - 1$
n_{bjets}	$= 0$ ($W +$ jets), ≥ 1 ($t\bar{t}$)
M_J^Σ	Same as SR
$E_{\text{T}}^{\text{miss}}/\sqrt{H_{\text{T}}}$	Table 5.4

Table 5.3: Summary table of the selections used to define the leptonic control regions used in this analysis.

allowed to be counted as a jet if it passes the $|\eta|, p_{\text{T}}$ selections made on jets. This is to allow the control regions to better model hadronic τ decays and leptons which are misidentified as jets.

The control region selections on the number of b tagged jets are designed to produce regions with high purities for $W +$ jets (0 b tagged jets) and $t\bar{t}$ (at least 1 b tagged jet). The m_T selection is designed to remove contributions from signal processes. As discussed in section 2.2.5.6 this variable is approximately bounded at m_W for leptonic decays of the W boson but is not bounded for cases where the $E_{\text{T}}^{\text{miss}}$ and lepton originate from different decays so this selection is useful to reduce signal contamination in our control regions. In some of the control regions very few events pass $E_{\text{T}}^{\text{miss}}/\sqrt{H_{\text{T}}} > 5\text{GeV}^{1/2}$ which would result in very large statistical uncertainties. Therefore in some regions this selection is relaxed. These selections are summarised in table 5.4.

Signal stream	CR n_{jets}		$E_{\mathrm{T}}^{\mathrm{miss}}/\sqrt{H_{\mathrm{T}}}$selection
Flavour stream	Jet $p_T > 50$ GeV	Jet $p_T > 80$ GeV	
	7, 8	6	> 5 GeV$^{1/2}$
	9	7	> 4 GeV$^{1/2}$
	10	8	> 3 GeV$^{1/2}$
Mass stream	$M_J^{\Sigma} > 340$ GeV	$M_J^{\Sigma} > 500$ GeV	
	8	-	> 5 GeV$^{1/2}$
	9	8	> 4 GeV$^{1/2}$
	10	9, 10	> 3 GeV$^{1/2}$

Table 5.4: Specific $E_{\mathrm{T}}^{\mathrm{miss}}/\sqrt{H_{\mathrm{T}}}$ selections for the control regions.

5.4.2.1 Region nomenclature

We adopt a shorthand to refer to regions based on the selections which define them. Each region name is split into sections by hyphens and begins with a string indicating which type it is: signal region (SR), control region (CR), template region (TR) or validation region (VR).

This is followed by a piece following the pattern <multiplicity><i/e>j<threshold> where the multiplicity and threshold refer to the jet multiplicity and the p_{T} selection used to define that multiplicity. The middle section details whether the selection is inclusive (i), requiring at least n jets or exclusive (e), requiring exactly n jets, where n is the jet multiplicity requirement. So 8ij50 signifies a selection requiring at least 8 jets with p_{T} greater than 50 GeV.

The last piece is the stream specific information. For the flavour stream this follows the pattern <multiplicity><i/e>b where the multiplicity now refers to the number of b tagged jets, for example 1ib would require at least 1 b tagged jet. For the mass stream the pattern is MJ<threshold> where the threshold refers to the selection on the M_J^{Σ} variable, measured in GeV, for example MJ340 would require $M_J^{\Sigma} > 340$ GeV.

So, the complete identifier SR-9ij50-MJ340 describes a signal region requiring at least 9 jets with p_{T} greater than 50 GeV and M_J^{Σ} greater than 340 GeV while CR-8ij80-0eb describes a control region requiring at least 8 jets with p_{T} greater than 80 GeV and exactly 0 b-tagged jets.

	2-step $[\tilde{g}, \tilde{\chi}_1^0] : [1400, 200]$ GeV	pMSSM $[\tilde{g}, \tilde{\chi}_1^\pm] : [1400, 200]$ GeV
Number of Events ($L_{\text{int}} = 36.1\,\text{fb}^{-1}$)	912.6	912.6
Preselection	896.9	875.5
Event Cleaning	888.7	872.9
4ij50 ($\lvert\eta\rvert < 2.0$)	886.4	870.1
Lepton Veto	482.7	400.5
Additional $E_{\text{T}}^{\text{miss}}$ Cleaning	459.8	382.7
8j50, $\lvert\eta\rvert < 2.0$ & $E_{\text{T}}^{\text{miss}}/\sqrt{H_{\text{T}}} > 5\,\text{GeV}^{1/2}$	314.7	226.2
HLT_6j45_0eta240	314.7	226.2
& ≥ 0 b-jet	314.7	226.2
& $M_J^\Sigma > 340$ GeV	284.3	210.2
& $M_J^\Sigma > 500$ GeV	201.8	162.9
& ≥ 1 b-jet	134.4	216.1
& ≥ 2 b-jet	43.0	172.0
9j50, $\lvert\eta\rvert < 2.0$ & $E_{\text{T}}^{\text{miss}}/\sqrt{H_{\text{T}}} > 5\,\text{GeV}^{1/2}$	210.4	150.1
HLT_6j45_0eta240	210.4	150.1
& ≥ 0 b-jet	210.4	150.1
& $M_J^\Sigma > 340$ GeV	196.6	143.2
& $M_J^\Sigma > 500$ GeV	148.0	117.8
& ≥ 1 b-jet	94.9	145.8
& ≥ 2 b-jet	32.7	121.1
10j50, $\lvert\eta\rvert < 2.0$ & $E_{\text{T}}^{\text{miss}}/\sqrt{H_{\text{T}}} > 5\,\text{GeV}^{1/2}$	117.1	87.1
HLT_6j45_0eta240	117.1	87.1
& ≥ 0 b-jet	117.1	87.1
& $M_J^\Sigma > 340$ GeV	112.4	84.4
& $M_J^\Sigma > 500$ GeV	90.7	73.4
& ≥ 1 b-jet	56.1	85.4
& ≥ 2 b-jet	20.3	73.4
11j50, $\lvert\eta\rvert < 2.0$ & $E_{\text{T}}^{\text{miss}}/\sqrt{H_{\text{T}}} > 5\,\text{GeV}^{1/2}$	52.9	43.2
HLT_6j45_0eta240	52.9	43.2
& ≥ 0 b-jet	52.9	43.2
& ≥ 1 b-jet	26.5	42.6
& ≥ 2 b-jet	10.9	37.5
7j80, $\lvert\eta\rvert < 2.0$ & $E_{\text{T}}^{\text{miss}}/\sqrt{H_{\text{T}}} > 5\,\text{GeV}^{1/2}$	279.5	186.7
HLT_5j70 OR HLT_5j65_0eta240	279.5	186.7
& ≥ 0 b-jet	279.5	186.7
& ≥ 1 b-jet	119.0	177.9
& ≥ 2 b-jet	37.1	143.8
8j80, $\lvert\eta\rvert < 2.0$ & $E_{\text{T}}^{\text{miss}}/\sqrt{H_{\text{T}}} > 5\,\text{GeV}^{1/2}$	168.3	100.5
HLT_5j70 OR HLT_5j65_0eta240	168.3	100.5
& ≥ 0 b-jet	168.3	100.5
& ≥ 1 b-jet	76.0	97.3
& ≥ 2 b-jet	25.9	81.9
9j80, $\lvert\eta\rvert < 2.0$ & $E_{\text{T}}^{\text{miss}}/\sqrt{H_{\text{T}}} > 5\,\text{GeV}^{1/2}$	76.1	47.7
HLT_5j70 OR HLT_5j65_0eta240	76.1	47.7
& ≥ 0 b-jet	76.1	47.7
& ≥ 1 b-jet	36.4	47.0
& ≥ 2 b-jet	13.2	40.3

Table 5.5: Signal region cutflows for benchmark points from the pMSSM and two-step signal grids.

	Gtt $[\tilde{g}, \tilde{\chi}_1^0] : [1500, 200]\,\text{GeV}$	RPV $[\tilde{g}, \tilde{t}] : [1400, 400]\,\text{GeV}$
Number of Events ($L_{\text{int}} = 36.1\,\text{fb}^{-1}$)	511.9	912.6
Preselection	473.8	904.4
Event Cleaning	472.8	896.6
4ij50 ($\|\eta\| < 2.0$)	469.4	895.9
Lepton Veto	205.6	580.5
Additional $E_{\text{T}}^{\text{miss}}$ Cleaning	195.7	554.0
`HLT_6j45_0eta240`	189.1	544.9
8j50, $\|\eta\| < 2.0$ & $E_{\text{T}}^{\text{miss}}/\sqrt{H_{\text{T}}} > 5\,\text{GeV}^{1/2}$	94.8	340.9
& ≥ 0 b-jet	94.8	340.9
& $M_J^{\Sigma} > 340\,\text{GeV}$	87.3	321.9
& $M_J^{\Sigma} > 500\,\text{GeV}$	62.9	270.9
& ≥ 1 b-jet	92.2	334.1
& ≥ 2 b-jet	75.8	265.6
9j50, $\|\eta\| < 2.0$ & $E_{\text{T}}^{\text{miss}}/\sqrt{H_{\text{T}}} > 5\,\text{GeV}^{1/2}$	52.5	198.8
& ≥ 0 b-jet	52.5	198.8
& $M_J^{\Sigma} > 340\,\text{GeV}$	49.7	191.4
& $M_J^{\Sigma} > 500\,\text{GeV}$	38.7	166.5
& ≥ 1 b-jet	51.4	195.8
& ≥ 2 b-jet	43.3	161.2
10j50, $\|\eta\| < 2.0$ & $E_{\text{T}}^{\text{miss}}/\sqrt{H_{\text{T}}} > 5\,\text{GeV}^{1/2}$	22.9	94.8
& ≥ 0 b-jet	22.9	94.8
& $M_J^{\Sigma} > 340\,\text{GeV}$	22.2	92.6
& $M_J^{\Sigma} > 500\,\text{GeV}$	18.5	83.2
& ≥ 1 b-jet	22.7	93.5
& ≥ 2 b-jet	19.4	78.6
11j50, $\|\eta\| < 2.0$ & $E_{\text{T}}^{\text{miss}}/\sqrt{H_{\text{T}}} > 5\,\text{GeV}^{1/2}$	8.4	36.6
& ≥ 0 b-jet	8.4	36.6
& ≥ 1 b-jet	8.3	36.2
& ≥ 2 b-jet	7.3	30.6
`HLT_5j70` OR `HLT_5j65_0eta240`	188.4	551.3
7j80, $\|\eta\| < 2.0$ & $E_{\text{T}}^{\text{miss}}/\sqrt{H_{\text{T}}} > 5\,\text{GeV}^{1/2}$	67.5	328.2
& ≥ 0 b-jet	67.5	328.2
& ≥ 1 b-jet	65.9	321.6
& ≥ 2 b-jet	54.4	257.2
8j80, $\|\eta\| < 2.0$ & $E_{\text{T}}^{\text{miss}}/\sqrt{H_{\text{T}}} > 5\,\text{GeV}^{1/2}$	30.5	177.7
& ≥ 0 b-jet	30.5	177.7
& ≥ 1 b-jet	29.9	175.4
& ≥ 2 b-jet	25.3	143.0
9j80, $\|\eta\| < 2.0$ & $E_{\text{T}}^{\text{miss}}/\sqrt{H_{\text{T}}} > 5\,\text{GeV}^{1/2}$	10.6	71.8
& ≥ 0 b-jet	10.6	71.8
& ≥ 1 b-jet	10.4	71.4
& ≥ 2 b-jet	9.0	60.1

Table 5.6: Signal region cutflows for benchmark points from the RPV and Gtt signal grids.

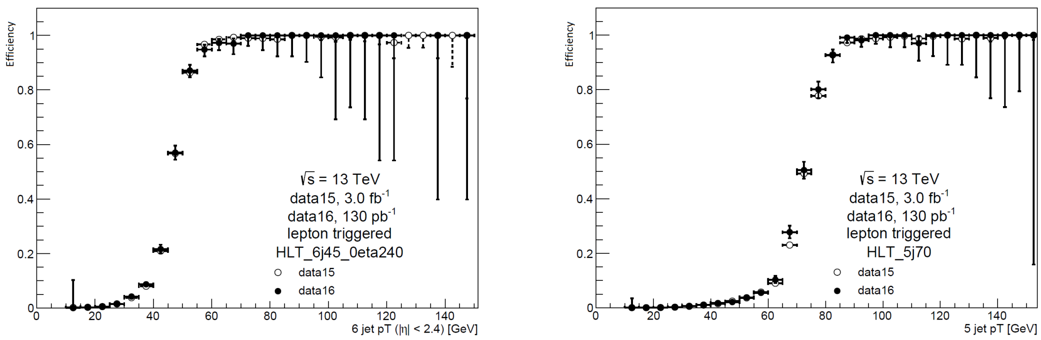

(a) 6 jet trigger **(b)** 5 jet trigger

Figure 5.4: Trigger turn on curves for the two main triggers used in this analysis. The data is shown separately for 2015 and early 2016, showing a similar performance for both years. In order to ensure an unbiased sample all events in these plots are required to pass a single lepton trigger. The left plot shows the efficiency of the 6 jet trigger as a function of the p_{T} of the 6th jet and the right plot shows the efficiency of the 5 jet trigger as a function of the p_{T} of the 5th jet.

5.4.2.2 Triggers

In order to ensure an unbiased sample of events passing the HLT we only use events which pass either or both of the two multijet triggers `HLT_5j70` or `HLT_6j45_0eta240`. These triggers select respectively events with either 5 jets with $p_{\mathrm{T}} > 70$ GeV or 6 jets with $p_{\mathrm{T}} > 45$ GeV and $|\eta| < 2.4$. The efficiencies of these triggers as a function of the 5$^{\mathrm{th}}$ and 6$^{\mathrm{th}}$ jet p_{T}s respectively are shown in figure 5.4. The 5 jet trigger becomes fully efficient by 85 GeV (Fig 5.4b) and the 6 jet trigger by 70 GeV (Fig 5.4a).

5.5 Background estimation

The vast majority of Standard Model events are removed by the selections described in the previous section. However there are still contributions from the Standard Model in the signal regions which must be accounted for.

5.5.1 Leptonic backgrounds

We use Monte Carlo simulation to predict the numbers of events from leptonic backgrounds which should appear in our signal regions. The largest single contributions are expected to be from $t\bar{t}$ and $W+$jets events so we normalise the

Process	Generator
$t\bar{t}$	POWHEG[138] with PYTHIA6[139] for the parton shower
Single top quarks	POWHEG[138] with PYTHIA6[139] for the parton shower
W/Z + jets	SHERPA 2.2.1[140]
Diboson	SHERPA 2.1[140]
$t\bar{t} + X$	MADGRAPH5 v.2.2.2[141] with PYTHIA8 for the parton shower
$t\bar{t} + h$	MADGRAPH5_aMC@NLO v.2.2.3[141] with PYTHIA8 for the parton shower

Table 5.7: The generators used for the major leptonic backgrounds. All processes generated require at least one lepton. The choice of generator is determined based on studies by the ATLAS Physics Modelling Group [142–145].

predictions of the simulations in these cases using the control regions described in table 5.3. These control regions are designed to be kinematically close to our signal regions but to be dominated by events from the targeted background process and very little signal. These are then used to derive normalisation factors for the predictions from simulation.

Table 5.7 shows the Monte Carlo generators used to generate the leptonic backgrounds. All simulated events are overlaid with multiple soft pp collisions simulated using PYTHIA8 [134]. The distribution of the pile-up generated this way is then reweighted to match the measured pile-up distribution from data. The ATLAS detector is then simulated using GEANT4 [135, 136]. More details are provided in reference [2]. As it is our largest leptonic background $t\bar{t}$ events are also simulated using MADGRAPH5_aMC@NLO with HERWIG++ [137] as well as with modified parameters in the nominal sample to account for uncertainties in the modelling.

Weights are applied to the Monte Carlo events. These can come from different sources. 'Pile-up' weights are applied to ensure that the simulated pile-up distribution is the same as the measured one. Scale factors are also applied to correct for differences between data and Monte Carlo for the selection of b jets, electrons and muons.

Figure 5.5 shows the jet multiplicity distributions for $W+$jets and $t\bar{t}$ control regions in the flavour stream after a fitting procedure described in section 5.6 has been applied, figure 5.6 shows the H_{T}distributions in the 80 GeV control regions

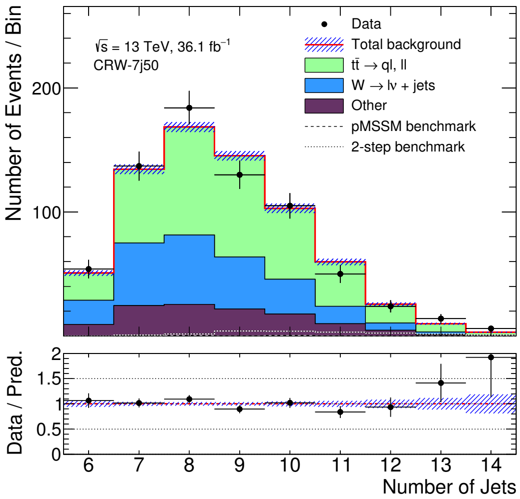

(a) $p_{T,j} = 50$ GeV, W CR

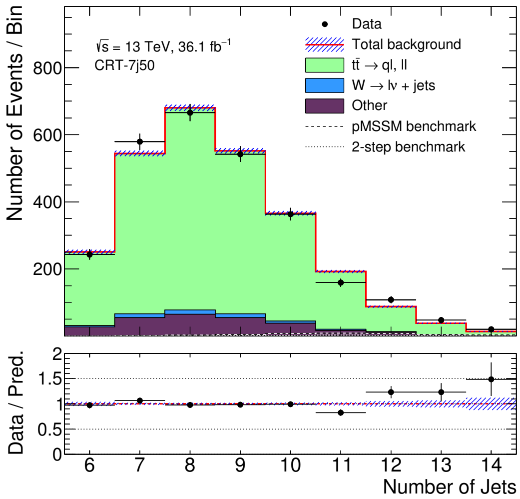

(b) $p_{T,j} = 50$ GeV, t CR

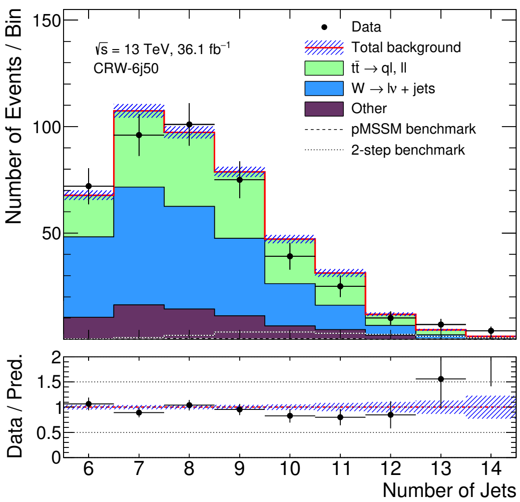

(c) $p_{T,j} = 80$ GeV, W CR

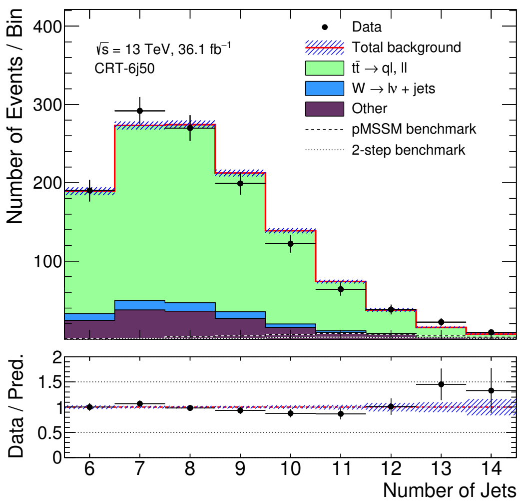

(d) $p_{T,j} = 80$ GeV, t CR

Figure 5.5: The n_j distributions are shown for the control regions with the lowest jet multiplicities. The distributions are shown for both W (left) and $t\bar{t}$ (right) control regions for regions with jets with p_{T} greater than 50 GeV (top) and 80 GeV (bottom). The W + jets and $t\bar{t}$ Monte Carlo predictions are shown using the scaling factors derived from the background-only fit described in section 5.6. The final bin does not include the overflow. This figure was produced by the analysis team.

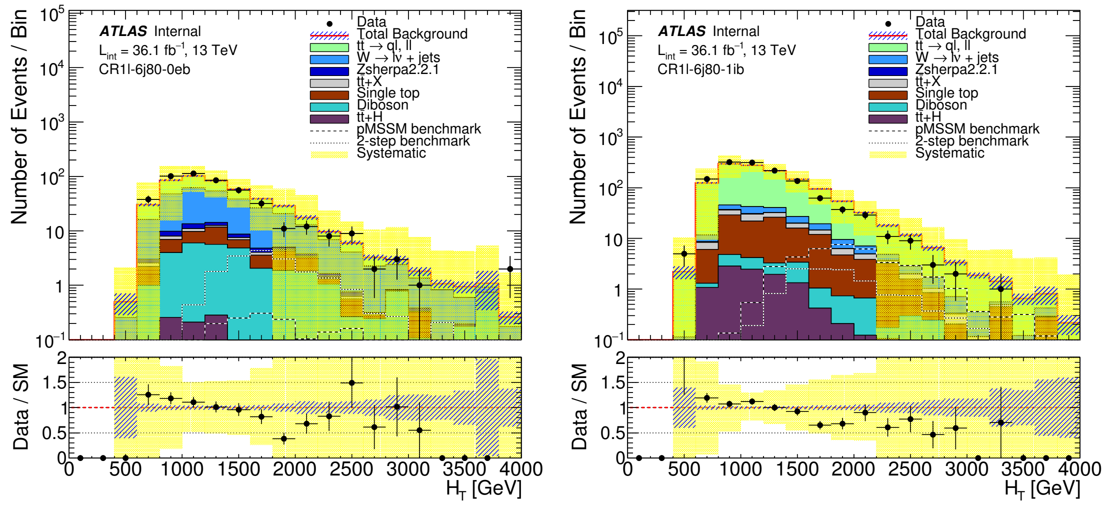

(a) W CR **(b)** t CR

Figure 5.6: The H_{T}distributions are shown for the $n_{\mathrm{jets}}(p_{\mathrm{T}} > 80\,\mathrm{GeV}) \geq 6$ control regions. The distributions are shown for both W (left) and $t\bar{t}$ (right) control regions. Systematic errors are shown as a yellow band separately to statistical errors, the error here is calculated as the sum in quadrature of all contribution and makes no attempt to allow for any correlations between them. This figure was produced by the analysis team.

with the lowest jet multiplicity. The Monte Carlo shows good agreement with data. The figure also shows a high purity in the $t\bar{t}$ regions but that there is a large component from $t\bar{t}$ in the W + jets control region.

5.5.2 QCD multijet background

The major background for this analysis comes from QCD multijet production. At the truth level this process contains little or no $E_{\mathrm{T}}^{\mathrm{miss}}$, with the majority coming from neutrinos produced in the decays of b and c jets. However the resolution effects described in section 4.2.2 lead to fake $E_{\mathrm{T}}^{\mathrm{miss}}$. Monte Carlo simulation of high multiplicity QCD events is unreliable so a data-driven method is used to predict the background from this source.

As discussed in section 5.3.2 the distribution of the $E_{\mathrm{T}}^{\mathrm{miss}}/\sqrt{H_{\mathrm{T}}}$ variable should be approximately invariant under changes in jet multiplicity. We use this observation to predict the contribution of events with large fake $E_{\mathrm{T}}^{\mathrm{miss}}$ to our signal regions, employing a method known as the template or 'ABCD' method illustrated in figure 5.7. In the limit where the distribution of $E_{\mathrm{T}}^{\mathrm{miss}}/\sqrt{H_{\mathrm{T}}}$ from fake $E_{\mathrm{T}}^{\mathrm{miss}}$ does not depend

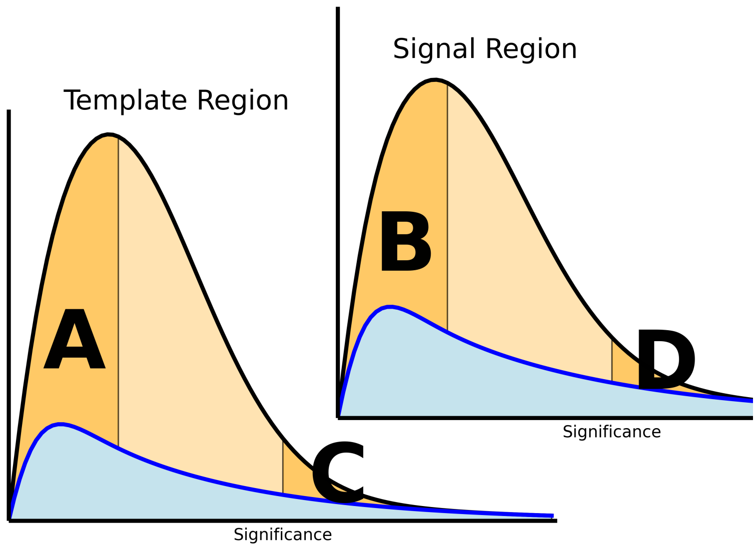

Figure 5.7: Graphic illustrating the template method. The distributions of $E_{\mathrm{T}}^{\mathrm{miss}}/\sqrt{H_{\mathrm{T}}}$ from the backgrounds are shown with the QCD in orange and the leptonic backgrounds in blue. The template and signal regions are shown in a darker orange and labeled.

on changes in jet multiplicity then we expect that the shapes of the two orange shaded areas should be same. We can therefore use a region (A and C in the figure) with low jet multiplicity to derive this shape and a region with low $E_{\mathrm{T}}^{\mathrm{miss}}/\sqrt{H_{\mathrm{T}}}$ but high jet multiplicity (C) to derive a scaling. Combining these we have a prediction of the contribution from this process to an area with high jet multiplicity and high $E_{\mathrm{T}}^{\mathrm{miss}}/\sqrt{H_{\mathrm{T}}}$ where we also expect to observe signal events (D).

We measure the A, B and C areas by counting the number of events in those regions and subtracting the predicted number of events from leptonic backgrounds (section 5.5.1). As we predict the shape should be the same we expect that $n_D/n_B = n_C/n_A$. In other words, the number of multijet events in region D is given by

$$n_D = n_B \frac{n_C}{n_A}.$$

The prediction is solely based on yields and cannot be interpreted as an event weighting. Therefore it is not possible to assess the modelling of kinematic variables beyond $E_{\mathrm{T}}^{\mathrm{miss}}/\sqrt{H_{\mathrm{T}}}$ itself. However checks on kinematic distributions in the control regions, whose predictions come solely from Monte Carlo, show measurements

Jet multiplicity		$E_{\mathrm{T}}^{\mathrm{miss}}/\sqrt{H_{\mathrm{T}}}$ [GeV$^{1/2}$]				
$p_{\mathrm{T}} > 50$ GeV	$p_{\mathrm{T}} > 80$ GeV	0 - 1.5	1.5 - 2.0	2.0 - 3.0	3.0 - 4.0	≥ 5.0
$== 6$	$== 5$	TR (A)	TR (C)	TR (C)	TR (C)	TR (C)
$== 7$	$== 6$	TR (B)	VR	VR	VR	VR
≥ 8	≥ 7	TR (B)	VR	VR	VR	SR
≥ 9	≥ 8	TR (B)	VR	VR	VR	SR
≥ 10	≥ 9	TR (B)	VR	VR	VR	SR
≥ 11		TR (B)	VR	VR	VR	SR

Table 5.8: Table showing the jet multiplicity and $E_{\mathrm{T}}^{\mathrm{miss}}/\sqrt{H_{\mathrm{T}}}$ selections for the multijet template, validation and signal regions in the analysis. For any signal region with an M_J^{Σ} or n_{bjets} selection the corresponding template and validation regions have the same M_J^{Σ} or n_{bjets} selection applied, except that there is no 11 jet signal region in the mass stream. The template regions are labeled with 'A', 'B' or 'C' to show which region they correspond to in figure 5.7.

of quantities such as n_{jets}(figure 5.5 and H_{T}(figure 5.6) agree with predictions to within uncertainties.

In order to assess the uncertainty on this prediction we define several validation regions at lower jet multiplicity and/or $E_{\mathrm{T}}^{\mathrm{miss}}/\sqrt{H_{\mathrm{T}}}$. These are shown in table 5.8. Each template/validation region has the same set of selections as its corresponding signal region, except for the jet multiplicity and $E_{\mathrm{T}}^{\mathrm{miss}}/\sqrt{H_{\mathrm{T}}}$ selections. The 'non-closure' uncertainty for any signal region is then defined as the maximum fractional difference between the measured data and prediction in any validation region with the same or lower jet multiplicity. This can be visualised on the table; for any signal region (D in the above notation) the corresponding template regions are the top left (A), the topmost cell in its column (C) and the leftmost cell in its row (B). The non-closure uncertainty is then the maximum fractional difference in any 'VR' cell inside the square described by those four cells. Figure 5.8 shows example $E_{\mathrm{T}}^{\mathrm{miss}}/\sqrt{H_{\mathrm{T}}}$ distributions in two of the validation regions, where we can see a good agreement between measured data and predictions.

There are a few effects which modify the idealised invariance of the template which we have to account for. While the template should be invariant under changes of jet multiplicity, by requiring a different jet multiplicity with a fixed p_{T} threshold we have made an implicit selection on H_{T}, and we do not expect the template to be exactly invariant under changes in H_{T} selection. In order to account for this, we 'bin'

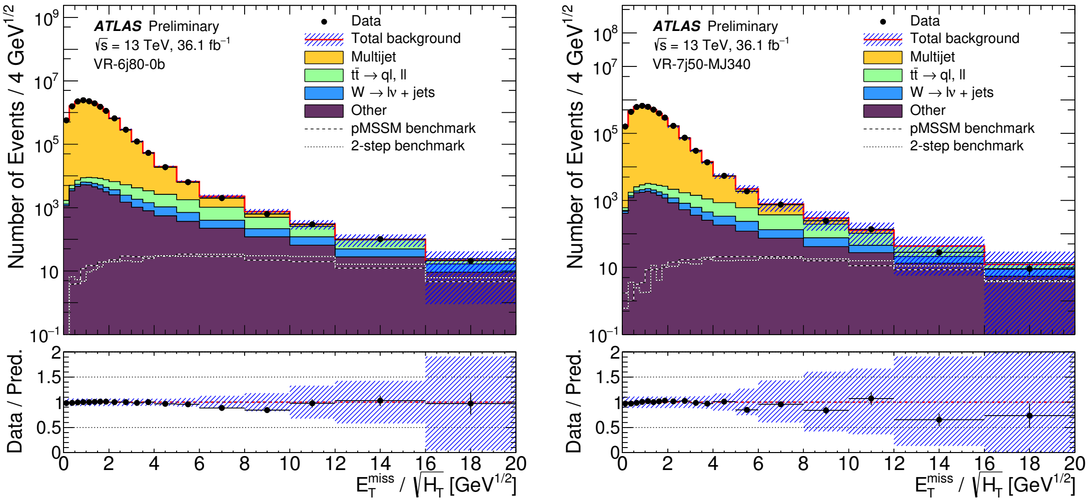

(a) `VR-6ej80-0ib` **(b)** `VR-7ej50-MJ340`

Figure 5.8: The $E_{\mathrm{T}}^{\mathrm{miss}}/\sqrt{H_{\mathrm{T}}}$ distribution measured in two of the validation regions is shown along with the prediction from Monte Carlo and the template method. This figure was produced by the analysis team.

the template method in H_{T}, making different template predictions for each H_{T} bin and summing the predictions together at the end. The lower bin edges are 0, 600, 900 and 1200 GeV. In order to account for differences from the choice of H_{T} binning we also use an alternative binning with lower edges at 0, 600, 800, 1000, 1200, and 1400 GeV and use the difference between the predictions as an additional uncertainty.

Another source of invariance comes from the heavy flavour decays. Decays of b quarks can produce real $E_{\mathrm{T}}^{\mathrm{miss}}$ from neutrinos which result in a larger $E_{\mathrm{T}}^{\mathrm{miss}}/\sqrt{H_{\mathrm{T}}}$ value. This effect is more important in events with a higher fraction of b jets, so when we predict the multijet background in the signal regions with a selection on n_{bjets} it is likely to be an overprediction. In order to account for this we define an additional uncertainty. We construct an additional template prediction by binning in n_{bjets}, splitting the inclusive $\geq n_{\mathrm{bjets}}$ selection into $== n_{\mathrm{bjets}}$ and $\geq n_{\mathrm{bjets}} + 1$ bins. We form a linear combination of the nominal template and this 'flavour-split' variant and use a χ^2 fit to find the optimal combination of the two. The fractional difference between this combination and the nominal is used as an additional uncertainty.

5.6 Statistical methods

5.6.1 Systematic uncertainties

As well as statistical uncertainties there are several sources of systematic uncertainties to consider. These are divided into three categories: detector, theory and template. These are all applied to Monte Carlo only, except for the template systematics which are only applied to the prediction from the template method. These uncertainties enter into the fitting procedure described in appendix B as Gaussian constraints whose widths are given by the differences between the nominal values and the values obtained after varying the relevant parameter.

5.6.1.1 Detector

Detector systematics are used to describe uncertainties arising from the simulation of the detector and the subsequent reconstruction algorithms described in section 3.5. Contributions from reconstruction and identification efficiencies are considered for selecting electrons, muons and hard-scatter jets using JVT, as well as for b tagging. Of these, only the latter has a significant effect on the predicted yield, at most 4% in some of the flavour stream signal regions. Contributions from measurements of the kinematics of electrons, muons, jets and photons are also considered, including propagating these through to the $E_{\mathrm{T}}^{\mathrm{miss}}$ calculation. Of these, uncertainties related to the jet energy scale and resolution are the most significant, contributing 6-12% to the uncertainty of the signal region yields. There is also an additional uncertainty associated with the simulation of the soft term of the $E_{\mathrm{T}}^{\mathrm{miss}}$ which has an effect of up to 8% on the yield in the mass stream. We also consider the effect of the uncertainty on the measurement of the total integrated luminosity of the data used in this measurement. This is a small effect ($< 1\%$) as it is only used in the normalisation of signal predictions and minor backgrounds, the normalisation of the major backgrounds being performed by the fitting process.

The full list of systematics is as follows:

Jet energy scale Nuisance parameters are derived which arise from measurements of the jet energy scale. In total there are 73 of these parameters which are impractical for use in most analyses. However, correlations between them can be exploited to form a reduced set of 4 nuisance parameters [146] which are varied independently in the fit (appendix B).

Jet energy resolution Jet energies are smeared according to a Gaussian whose width is given by the difference between the measurements of the jet energy resolution from Monte Carlo and data.

b **tagging** The *b* tagging scale factors are varied to account for uncertainties from their measurment. Uncertainties on the measurements of these scale factors are propagated through to the fit.

$E_{\mathrm{T}}^{\mathrm{miss}}$ **soft term** The effect of uncertainties on the hard objects in the $E_{\mathrm{T}}^{\mathrm{miss}}$ sum are propagated through from those sources (e.g. the jet energy scale). Additional uncertainties are applied to the soft term in the $E_{\mathrm{T}}^{\mathrm{miss}}$, through up/down variations on its scale and through smearing the measured soft term to correct for the difference in resolution between data and Monte Carlo.

Pile-up reweighting Up and down variations are applied to the pile-up reweighting scale factor to account for uncertainties deriving from the minimum bias overlay used in Monte Carlo simulation.

Electron/photon energy scale and resolution Two nuisance parameters are used, one for the total resolution uncertainty and a second for the scale uncertainty. All contributing components are treated as uncorrelated.

Electron selection efficiency The electron scale factors are varied to account for uncertainties from their measurement, allowing for uncertainties from the reconstruction process and the particle ID and isolation selections.

Muon momentum scale and resolution A single up/down variation is applied to the absolute momentum scale. Additionally, the tracks in the inner detector and the muon spectrometer are independently varied according to the resolutions of those detectors then the impact on the momentum measurement of the combined track is calculated.

Muon selection efficiency The muon scale factors are varied to account for uncertainties in their measurement. The statistical and systematic uncertainties are treated separately.

5.6.1.2 Theory

Theory systematics are used to describe uncertainties from the event generation, including effects from the process' matrix element and from the subsequent showering and decay of particles produced in the matrix element. The single largest source of uncertainty in the signal regions comes from the simulation of QCD radiation from t quarks in $t\bar{t}$ events, comprising an uncertainty of 10-25% of the $t\bar{t}$ prediction. A smaller contribution comes from the parton shower uncertainties which can sometimes be comparable to the radiation systematic uncertainty. The full list of theory systematics is as follows:

$t\bar{t}$

- Uncertainties from the generation of the matrix element and parton showers for the dominant $t\bar{t}$ background are estimated by varying the generators used. The baseline sample is generated using Powheg for the matrix element and Pythia6 for the parton shower. Alternative samples are generated using alternative parton shower generators Pythia8 and Herwig, both still using Powheg for the matrix element. An additional sample is generated where MadGraph5_aMC@NLO is used instead of Powheg. The predictions from these samples are used as separate variations in the fit.
- RadHi/RadLo increase/decrease the rate of extra QCD radiation produced in addition to the base physics process.

$W +$ jets

Uncertainties are generated by considering variations to the renormalisation, factorisation, resummation and matching scales. The first two (section 2.2.4.2) are varied together in 7 combinations:

$$\{\mu_F, \mu_R\} = \{0.5, 0.5\}, \{1, 0.5\}, \{0.5, 1\}, \{1, 1\}, \{2, 1\}, \{1, 2\}, \{2, 2\}.$$

The resummation scale describes the energy scale at which the parton shower is truncated. The matching scale determines whether an emission is treated as part of the matrix element or parton shower. Each of the scales is varied between $1/\sqrt{2}$ and $\sqrt{2}$.

Minor backgrounds

The other Monte Carlo backgrounds are not significant enough to warrant a detailed calculation of uncertainties, as they only predict samll numbers of events in the signal regions. Therefore global, conservative uncertainties on the their predictions are applied:

- diboson: 50%
- $t\bar{t} + X$: 30%
- single top: 30%
- $Z+$ jets: 40%

5.6.1.3 Template

Template systematics are used to assess the uncertainty inherent in the predictions from the template method. These have already been discussed in section 5.5.2 and consist of the non-closure, flavour and H_{T} binning uncertainties. As all of these systematics are derived solely by comparing yields they tend to be largest in the tightest signal regions where statistical fluctuations become more important. The non-closure systematic is typically in the range 8-12% but reaches 30% in the tightest signal regions. The flavour systematic tends to be most important in regions with tighter requirements on n_{bjets}, reaching at most 20% while it never rises above 2% for the mass stream. The H_{T} binning uncertainty is smallest in low jet multiplicity signal regions in the mass stream where the M_J^{Σ} selection has a similar effect to the binning and rises to between 5 and 10% in other signal regions.

5.6.2 Statistical tests

The measurements from data in the various defined regions (section 5.4.2) are combined with the predictions from simulation and the uncertainties described above into a statistical fitting process. This process is described in full in appendix B. Three different fits are performed: the background-only fit, the model independent fit and the model dependent fit. The background-only fit uses the background predictions (from simulation and the template method) in the control and template regions in concert with their uncertainties to provide normalisation factors (μ_W, $\mu_{t\bar{t}}$, $\mu_{\mathrm{multijets}}$) to modify their predictions in the signal regions. In the absence of an excess of measured events in a signal region, the model independent fit uses the predictions from the background-only fit to predict the maximum number of events a given signal model could predict in that region and still be compatible with the measurements. The model dependent fit is similar to the background-only fit, but it also considers the contribution from a specific signal model to the control and signal regions and calculates the confidence level at which that model can be excluded.

As the individual signal regions overlap in a non-trivial manner a combined fit including information from all regions is not possible. Therefore instead for each model point the signal region with the best *expected* sensitivity is chosen to provide the information for the fit.

5.7 Results

The selections described in section 5.4.2 are applied to the processed data and the numbers of events entering into each of the defined kinematic regions are counted. These counts are then used as the inputs to the fitting procedure described in section 5.6. The results of the background-only fit are shown in figure 5.9. For most signal regions $\mu_{t\bar{t}}$ is close to unity, however for regions with higher jet

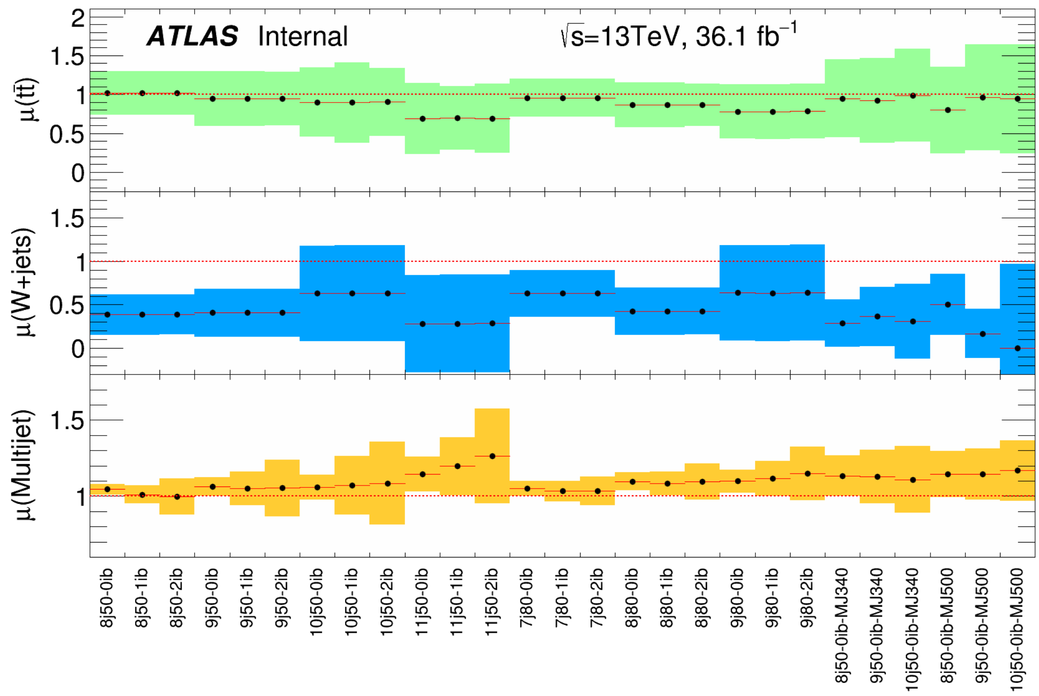

Figure 5.9: The normalisation factors and associated uncertainties derived for each signal region using the background-only fit described in section 5.6. This figure was produced by the analysis team.

multiplicities the normalisation can fall to as low as 0.71. The normalisation for $W+$jets μ_W falls within the range 0.3 - 0.6, consequently μ_{multijet} is corrected upwards. Figure 5.5 on page 114 shows that the modelling of the Standard Model backgrounds in the control regions remains good.

The distribution of $E_{\mathrm{T}}^{\mathrm{miss}}/\sqrt{H_{\mathrm{T}}}$ in two of the signal regions is shown in figure 5.10. The full distribution is shown, including the template and validation regions. The background prediction agrees with the data within uncertainties.

The numbers of data events measured in the signal regions are shown, along with the predicted Standard Model backgrounds in table 5.9 and figure 5.11. The results show no tension with the Standard Model, with the most significant deviation being a 1.8σ deficit in `SR-9ij50-MJ500`.

Figures 5.12 and 5.13 show the exclusion limits for all of the benchmark signal models described in section 5.2.2. The CL_s values are calculated for each grid point considered as described in section 5.6. These values are then converted

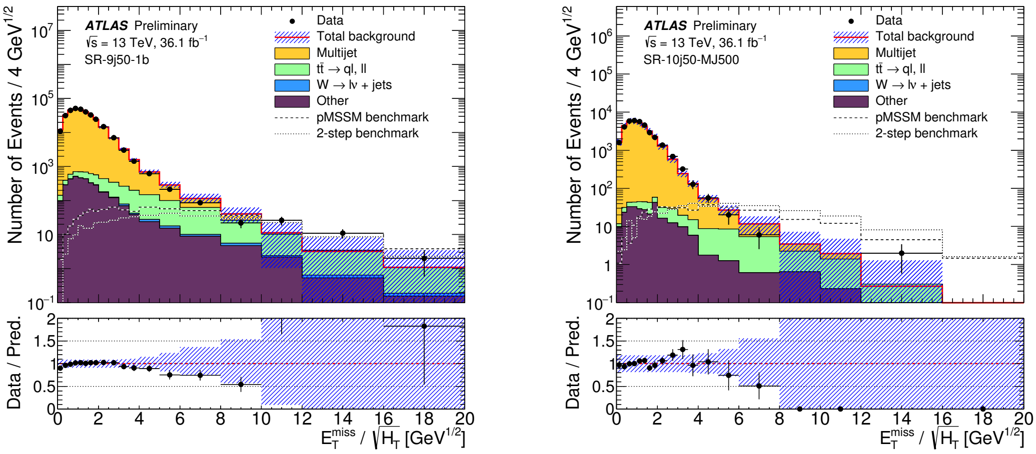

(a) `SR-9ij50-1ib` **(b)** `SR-10ij50-MJ500`

Figure 5.10: The full $E_{\mathrm{T}}^{\mathrm{miss}}/\sqrt{H_{\mathrm{T}}}$ distributions for two of the signal regions. The left plot shows a region requiring at least 9 jets with p_{T} greater than 50 GeV and at least 1 b-tagged jet, the right a region requiring at least 10 jets with p_{T} greater than 50 GeV and M_J^{Σ} greater than 500 GeV. The background predictions and uncertainties are shown after the background-only fitting procedure described in section 5.6. Two benchmark signal points are also shown: a pMSSM point with $(m_{\tilde{g}}, m_{\tilde{\chi}_1^{\pm}}) = (1400, 200)$ GeV and a 2-step point with $(m_{\tilde{g}}, m_{\tilde{\chi}_1^0}) = (1400, 200)$ GeV. This figure was produced by the analysis team.

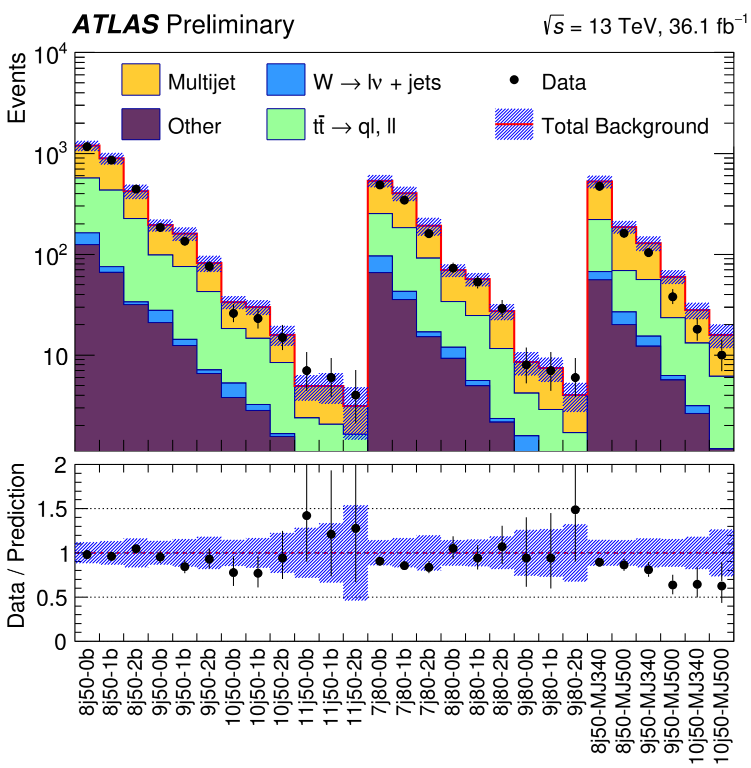

Figure 5.11: The expected Standard Model backgrounds split by process, and the observed data yields. This figure was produced by the analysis team.

Signal Region	Predicted Background			Observed Events
	Multijet	Leptonic	Total	
SR-8ij50-0ib	622 ± 42	570 ± 140	1190 ± 140	1169
SR-8ij50-1ib	460 ± 50	430 ± 110	890 ± 140	856
SR-8ij50-2ib	196 ± 39	226 ± 57	422 ± 81	442
SR-9ij50-0ib	96 ± 11	98 ± 24	194 ± 28	185
SR-9ij50-1ib	84 ± 15	76 ± 20	160 ± 31	135
SR-9ij50-2ib	39 ± 12	42.5 ± 9.5	82 ± 19	76
SR-10ij50-0ib	15.1 ± 3.0	18.3 ± 3.9	33.5 ± 5.1	26
SR-10ij50-1ib	15.3 ± 3.7	14.7 ± 3.3	30.0 ± 5.9	23
SR-10ij50-2ib	7.6 ± 3.1	8.4 ± 1.8	16.0 ± 4.2	15
SR-11ij50-0ib	2.54 ± 0.76	2.4 ± 1.2	4.9 ± 1.2	7
SR-11ij50-1ib	2.88 ± 0.84	2.1 ± 1.4	5.0 ± 1.3	6
SR-11ij50-2ib	1.49 ± 0.72	1.6 ± 1.5	3.1 ± 1.5	4
SR-7ij80-0ib	282 ± 32	253 ± 69	535 ± 74	486
SR-7ij80-1ib	219 ± 28	183 ± 60	402 ± 74	343
SR-7ij80-2ib	100 ± 17	91 ± 34	191 ± 44	160
SR-8ij80-0ib	35.7 ± 4.6	33.8 ± 8.3	70 ± 10	73
SR-8ij80-1ib	31.6 ± 5.7	24.8 ± 6.4	56 ± 10	53
SR-8ij80-2ib	15.5 ± 3.8	11.6 ± 3.3	27.1 ± 6.0	29
SR-9ij80-0ib	4.3 ± 1.3	4.2 ± 1.8	8.5 ± 2.0	8
SR-9ij80-1ib	4.5 ± 1.3	2.9 ± 1.5	7.4 ± 1.8	7
SR-9ij80-2ib	2.34 ± 0.95	1.69 ± 0.89	4.0 ± 1.2	6
SR-8ij50-MJ340	306 ± 54	220 ± 55	526 ± 72	471
SR-8ij50-MJ500	118 ± 18	69 ± 20	187 ± 54	161
SR-9ij50-MJ340	73 ± 15	56 ± 15	129 ± 23	104
SR-9ij50-MJ500	36.5 ± 6.3	23.3 ± 7.0	60 ± 10	38
SR-10ij50-MJ340	14.6 ± 3.8	13.2 ± 3.5	27.9 ± 5.7	18
SR-10ij50-MJ500	9.8 ± 2.6	6.2 ± 3.3	16.0 ± 4.7	10

Table 5.9: The expected Standard Model backgrounds split into multijet and leptonic contributions and the observed data yields. Expected background counts are shown after the fitting procedure described in section 5.6

into a significance measure and interpolated to form a contour plot, with the contour drawn at $Z = 1.64$, corresponding to a $\mathrm{CL}_s = 0.05$. The expected limits are shown with the $\pm 1\sigma$ variations on the background prediction in the signal regions. The observed limits are also shown with $\pm 1\sigma$ variations on the predicted signal cross-section. Figure 5.12 also shows the exclusion limits from the earlier $3.2\mathrm{fb}^{-1}$ analysis [1] in grey.

In the **two-step signal model** gluinos are excluded up to a mass of 1.8 TeV

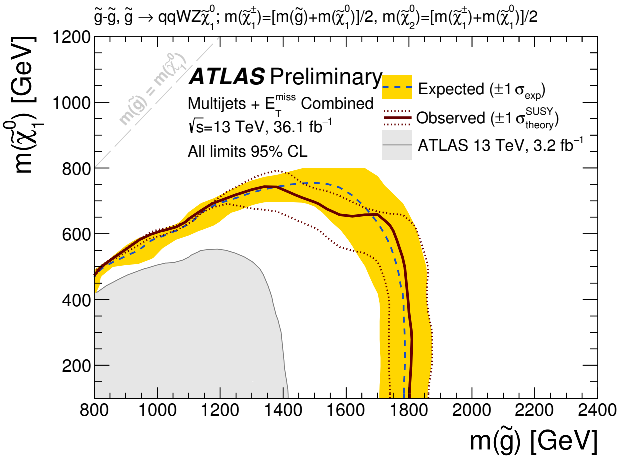

(a) Two-step

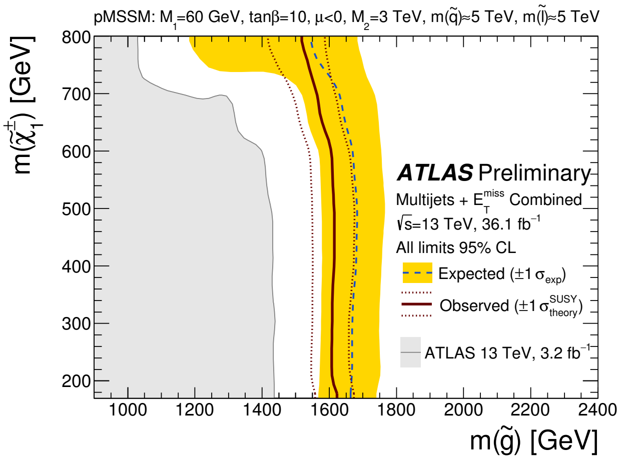

(b) pMSSM

Figure 5.12: Exclusion limits for the pMSSM and two-step signal models. This figure was produced by the analysis team.

up to a LSP mass of 650 GeV. For gluino masses between 1 and 1.8 TeV the exclusion limit for the LSP mass ranges from between 600 and 750 GeV. For the **pMSSM slice** gluinos are excluded up to a mass of 1.6 TeV for chargino masses of up to 600 GeV. The exclusion falls to a gluino mass of 1.5 TeV for a chargino mass of 800 GeV, no model points were generated above this. In the **Gtt model** gluinos are excluded beyond masses of 1.5 TeV for LSP masses up to 500 GeV. For gluino masses between 1 and 1.45 TeV the exclusion limit for the LSP mass ranges from between 600 and 700 GeV. Below 1 TeV the exclusion is limited by the kinematic limit, with sensitivity lost only in very compressed

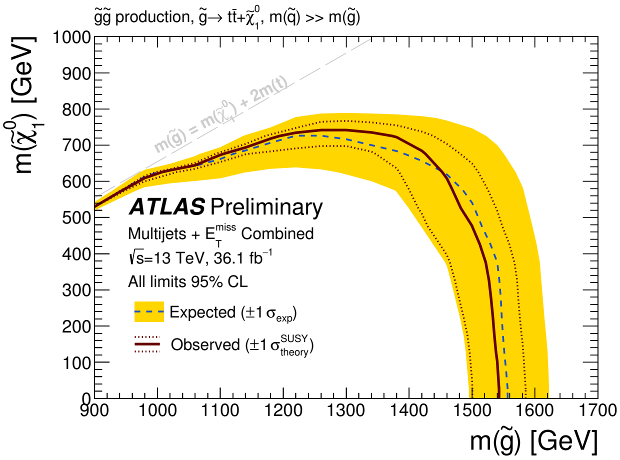

(a) Gtt

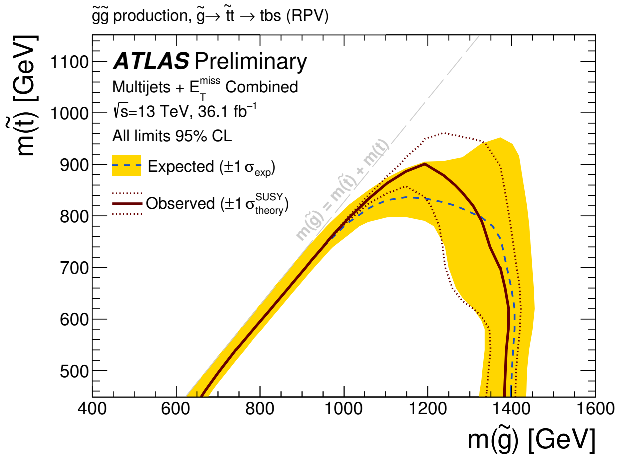

(b) RPV

Figure 5.13: Exclusion limits for the Gtt and RPV signal models. On both plots dashed lines show the kinematic limits beyond which the simulated decays would not obey conservation of energy. This figure was produced by the analysis team.

scenarios ($m_{\tilde{g}} - (m_{\tilde{\chi}_1^0} + 2m_t) < 30\,\text{GeV}$). For the **RPV model** gluino masses up to 1.4 TeV are excluded for low stop masses. The exclusion in stop mass reaches 900 GeV for a gluino mass of 1.2 TeV. For lower gluino masses the exclusion limit approaches the kinematic limit, only losing sensitivity in the compressed region ($m_{\tilde{g}} - (m_{\tilde{t}} + m_t) < 50\,\text{GeV}$). This concludes the results of reference [2].

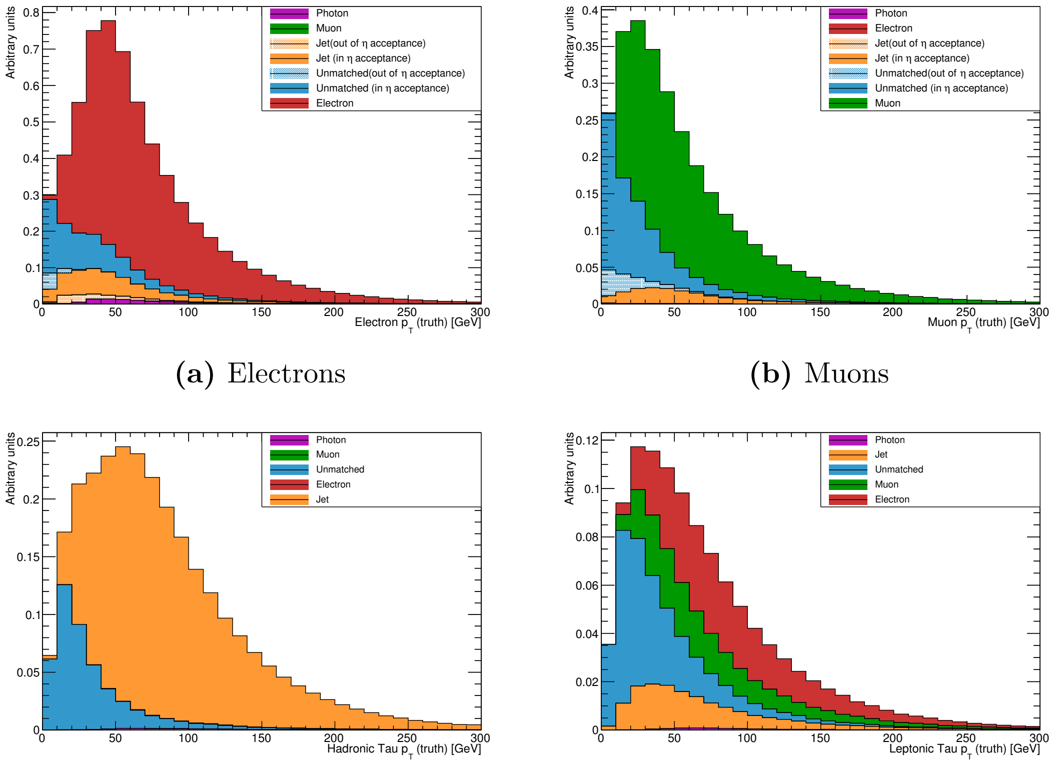

(a) Electrons

(b) Muons

(c) Hadronic Taus

(d) Leptonic Taus

Figure 5.14: Plots showing how truth level leptons in $t\bar{t}$ events are classified at the reconstruction level. Leptons are split into electrons, muons and taus with the taus split into leptonic and hadronic decay modes. No attempt is made to identify reconstructed taus.

5.8 Possible future improvements

In this section, improvements beyond the techniques used in reference [2] are investigated. First, the origins of leptonic events entering the signal regions are investigated. Second, a more sophisticated measure of $E_{\mathrm{T}}^{\mathrm{miss}}$ significance is discussed.

5.8.1 Leptonic contamination in signal regions

Figure 5.14 shows how leptons simulated at the MC truth level are reconstructed by the detector simulation in the $t\bar{t}$ Monte Carlo. The truth level particles are matched to the closest reconstructed object, using ΔR as a measure of distance. Any truth level particles that are more than $\Delta R = 0.2$ away from a reconstructed object are labeled as ‘unmatched’. The majority of high p_{T} electrons and muons tend to be well reconstructed by the detector, however at low p_{T} there are significantly fewer muons being reconstructed than electrons. It is relatively rare for either lepton to be mis-IDed as a jet. However, the majority of the contributions from these events to the signal regions come from tau leptons. We make no attempt to ID hadronic taus and so they are usually reconstructed as jets. Leptonically decaying taus also tend to be identified less often than the other two leptons which may be due to the presence of the extra neutrinos which carry away a significant part of the p_{T} from the original tau. This suggests that a potentially significant proportion of the leptonic backgrounds could be removed by identifying hadronically decaying taus and extending the lepton veto to apply to them.

5.8.2 Object based significance

While the prediction shown in figure 5.10 is consistent to within uncertainties, a consistent shape in the data/prediction ratio plot is becoming visible. With larger quantities of simulated and observed events this shape may no longer be consistent with unity. This non-closure increases the corresponding template uncertainties and reduces the sensitivity of the analysis. Some predicted sources of non-closure were detailed in section 5.5.2. In particular, it was observed that applying a veto on b-tagged jets improved this non-closure but did not remove it.

Another potential source of non-closure lies in the assumption made in section 5.3.2 that the variance of the $E_{\mathrm{x}}^{\mathrm{miss}}$ and $E_{\mathrm{y}}^{\mathrm{miss}}$ distributions can be approximated purely as a function of H_{T}. Object resolutions can be measured in data [133] and these measurements used to more accurately calculate each σ_i (equation 4.1), again assuming that the mismeasurements follow a Gaussian distribution. A further improvement can be made by considering the full covariance between the x and y components of the $E_{\mathrm{T}}^{\mathrm{miss}}$. The covariance matrix for the measurement of a single particle (assuming that the mismeasurements parallel and perpendicular to its axis are uncorrelated) is given by

$$\mathbf{\Sigma}_i = \sigma_i^2 \begin{pmatrix} \cos^2\phi_i & \cos\phi_i \sin\phi_i \\ \cos\phi_i \sin\phi_i & \sin^2\phi_i \end{pmatrix} .$$

Given this covariance matrix, the probability density function for the mismeasurement of the i^{th} object is given by

$$f(\vec{\boldsymbol{x}}_i|\boldsymbol{\Sigma}_i)\mathrm{d}\vec{\boldsymbol{x}_i} = \frac{1}{2\pi\sqrt{|\boldsymbol{\Sigma}_i|}} e^{-1/2\,\vec{\boldsymbol{x}}^T\boldsymbol{\Sigma}_i^{-1}\vec{\boldsymbol{x}}}\mathrm{d}\vec{\boldsymbol{x}_i}$$

and the corresponding function for the mismeasured $\vec{\boldsymbol{p}}_{\mathrm{T}}^{\mathrm{miss}}$, i.e. the vector sum of all of the (assumed uncorrelated) mismeasurements is

$$f(\vec{\boldsymbol{x}}|\boldsymbol{\Sigma})\mathrm{d}\vec{\boldsymbol{x}} = \frac{1}{2\pi\sqrt{|\boldsymbol{\Sigma}|}} e^{-1/2\,\vec{\boldsymbol{x}}^T\boldsymbol{\Sigma}^{-1}\vec{\boldsymbol{x}}}\mathrm{d}\vec{\boldsymbol{x}}\,. \tag{5.1}$$

Equation 5.1 is only a property of the covariance matrix $\boldsymbol{\Sigma}$ which can be calculated on an event-by-event basis. Therefore following the same argument as in section 4.2.2, we expect the variable $S = \sqrt{\vec{\boldsymbol{p}}_{\mathrm{T}}^{\mathrm{miss}T}\boldsymbol{\Sigma}^{-1}\vec{\boldsymbol{p}}_{\mathrm{T}}^{\mathrm{miss}}}$ to follow a Rayleigh distribution that is independent of other properties of the event, such as the number of jets.

A true missing transverse momentum $\vec{\boldsymbol{p}}_{\mathrm{T\,true}}^{\mathrm{miss}}$ can be introduced into equation 5.1 using the transformation $\vec{\boldsymbol{x}} = \vec{\boldsymbol{p}}_{\mathrm{T\,obs}}^{\mathrm{miss}} - \vec{\boldsymbol{p}}_{\mathrm{T}}^{\mathrm{miss}}\mathrm{true}$, giving the likelihood

$$\mathcal{L}(\vec{\boldsymbol{p}}_{\mathrm{T\,obs}}^{\mathrm{miss}}|\boldsymbol{\Sigma},\vec{\boldsymbol{p}}_{\mathrm{T\,true}}^{\mathrm{miss}}) = \frac{1}{2\pi\sqrt{|\boldsymbol{\Sigma}|}} e^{-1/2(\vec{\boldsymbol{p}}_{\mathrm{T\,obs}}^{\mathrm{miss}}-\vec{\boldsymbol{p}}_{\mathrm{T\,true}}^{\mathrm{miss}})^T\boldsymbol{\Sigma}^{-1}(\vec{\boldsymbol{p}}_{\mathrm{T\,obs}}^{\mathrm{miss}}-\vec{\boldsymbol{p}}_{\mathrm{T\,true}}^{\mathrm{miss}})}\mathrm{d}\vec{\boldsymbol{x}}\,.$$

We can then construct a log-likelihood ratio to calculate how likely it is that the measured $E_{\mathrm{T}}^{\mathrm{miss}}$ is from mismeasurement by comparing the likelihoods of $\vec{\boldsymbol{p}}_{\mathrm{T\,obs}}^{\mathrm{miss}} = \vec{\boldsymbol{p}}_{\mathrm{T\,true}}^{\mathrm{miss}}$ and $\vec{\boldsymbol{p}}_{\mathrm{T\,obs}}^{\mathrm{miss}} = \vec{\boldsymbol{0}}$

$$-2\ln\left(\frac{\mathcal{L}(\vec{\boldsymbol{p}}_{\mathrm{T\,obs}}^{\mathrm{miss}}|\boldsymbol{\Sigma},\vec{\boldsymbol{p}}_{\mathrm{T\,obs}}^{\mathrm{miss}})}{\mathcal{L}(\vec{\boldsymbol{p}}_{\mathrm{T\,obs}}^{\mathrm{miss}}|\boldsymbol{\Sigma},\vec{\boldsymbol{0}})}\right) = \vec{\boldsymbol{p}}_{\mathrm{T\,obs}}^{\mathrm{miss}\;T}\boldsymbol{\Sigma}^{-1}\vec{\boldsymbol{p}}_{\mathrm{T\,obs}}^{\mathrm{miss}} = S^2\,.$$

Therefore S gives us an 'object based $E_{\mathrm{T}}^{\mathrm{miss}}$ significance' from which we can build the template, instead of $E_{\mathrm{T}}^{\mathrm{miss}}/\sqrt{H_{\mathrm{T}}}$.

Figure 5.15 shows a test of this idea. The template prediction is calculated for the `SR-9ij50-0ib` selection and the ratio between it and the measured data is plotted for the original $E_{\mathrm{T}}^{\mathrm{miss}}/\sqrt{H_{\mathrm{T}}}$ variable and S. This calculation was not done with the full statistical model so the fit is not derived and only statistical uncertainties are shown. However, it can be seen that the template constructed using the object based significance predicts the data in the signal region much better than does $E_{\mathrm{T}}^{\mathrm{miss}}/\sqrt{H_{\mathrm{T}}}$. It is also anticipated that this variable should provide better discrimination between signal and background. This method may be used in future analyses of this sort.

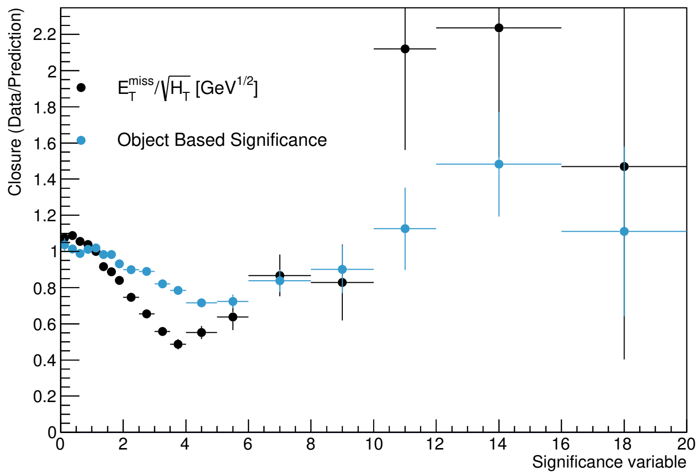

Figure 5.15: The template closure for two different choices of variables shown for the `SR-9ij50-0ib` region. Plotted is the ratio of the observed data to the full Standard Model prediction using Monte Carlo and the template method. The fit has not been applied so the Monte Carlo is not fully scaled and only statistical uncertainties are shown.

5.9 Conclusions

This chapter has presented a search for physics beyond the Standard Model producing final states with moderate $E_{\mathrm{T}}^{\mathrm{miss}}$ and large jet multiplicities. Models predicting final states matching this signature can be common in both RPV and RPC SUSY theories. As shown in chapter 4, a considerable background to this signature comes from events with little or no true $E_{\mathrm{T}}^{\mathrm{miss}}$ but which acquire a large measured $E_{\mathrm{T}}^{\mathrm{miss}}$ due to the effects of mismeasurement. This analysis used a template method on the variable $E_{\mathrm{T}}^{\mathrm{miss}}/\sqrt{H_{\mathrm{T}}}$ to estimate the contribution from this multijet background to the signal regions and Monte Carlo simulation to estimate the contribution from backgrounds containing leptons. The predictions for the largest two of these leptonic backgrounds were improved using a maximum likelihood fit based on dedicated control regions.

No significant excesses over the Standard Model prediction are observed so exclusion limits were set on new physics models. Two of the four studied models were also considered in a previous iteration of the analysis [1]. In the '2-step' model, the exclusion of gluino masses is extended by 400 GeV and in the 'pMSSM' model by 200 GeV.

6
Conclusions

As I write this thesis the LHC is approaching the end of its extremely successful second run. This run has seen the LHC breaking several records, including achieving an instantaneous luminosity of over $2 \times 10^{34} \mathrm{cm}^{-2}\,\mathrm{s}^{-1}$, double its design luminosity. This has provided analysers with the opportunity to test the Standard Model to unprecedented levels.

However, this performance can also place significant strain on the systems responsible for providing this data, driving the development of new techniques. One such system was discussed in chapter 4: the $E_{\mathrm{T}}^{\mathrm{miss}}$ trigger. This chapter discussed various metrics used to assess the performance of the trigger and select future strategies. The results of such studies using 2015 data were presented. This was followed by the introduction of a new technique of combining the results of multiple trigger algorithms, which was able to reduce rates by a factor of almost 4, without too greatly affecting analysis efficiencies. This technique is likely to continue to be important as conditions in the detector become more challenging.

This thesis also described a search for new physics using 13 TeV ATLAS data in chapter 5. This analysis targets final states with large jet multiplicity and moderate $E_{\mathrm{T}}^{\mathrm{miss}}$. A large Standard Model background exists for this event topology, dominated by events where the measured $E_{\mathrm{T}}^{\mathrm{miss}}$ is generated by mismeasurement rather than an actual invisible particle. This is the same mechanism that drives the large rate increases observed in $E_{\mathrm{T}}^{\mathrm{miss}}$ trigger in chapter 4. The same statistical procedure demonstrated there motivates the use of a template method to predict the background from QCD events, using the properties of the $E_{\mathrm{T}}^{\mathrm{miss}}/\sqrt{H_{\mathrm{T}}}$ variable. This analysis was able to extend the exclusion of gluino masses up to 1.6 TeV when looking at a set of model points shown not to have been excluded by Run 1 analyses.

Although no significant deviations from Standard Model predictions have yet been found, the LHC physics program is due to continue for many more years. During this period the detectors positioned on its ring will collect enormous datasets capable of extending our reach to as-yet untested models, improving our abilities to answer some of the most fundamental questions about our universe.

Appendices

Glossary

R-parity Multiplicative quantum number that is $+1$ for standard model particles and -1 for SUSY particles. 98, 99, 103, 137

R-parity conserving Refers to a SUSY model in which R-parity is conserved. 33, 139

R-parity violating Refers to a SUSY model in which R-parity is violated. 31, 139

beyond the standard model Theories that extend the standard model in some way. 33, 139

bino Super partner to the B boson. 102

chargino General term for a charged electroweakino . 127

electroweakino General term for a particle corresponding to a mixture of the super partners of the electroweak bosons. 99, 137

gluino The super partner of the gluon. 2, 98, 99, 102, 103, 126–128, 134

Higgsino Super partner to a Higgs boson. 102

Large Hadron Collider The world's largest and most powerful particle accelerator, situated at CERN in Geneva. 2, 139

lightest supersymmetric particle The lightest sparticle in a given SUSY model. In RPC models this will be stable. In cases where it is only weakly interacting it could be a dark matter candidate. 31, 139

local cluster weighting A calibration applied to topoclusters. 57, 139

parton distribution function A function detailing the probability to interact with a particular constituent of a hadronic object, usually a proton, in a high energy collision. 22, 139

sparticle A super partner of a standard model particle, i.e. a member of the SUSY sector in a SUSY theory. 98

supersymmetry A class of BSM theory that predicts the existence of a symmetry between fermion and boson states. 2, 139

Acronyms

BSM beyond the standard model. 33, 100, 139, *Glossary:* beyond the standard model

LCW local cluster weighting. 57, 139, *Glossary:* local cluster weighting

LHC Large Hadron Collider. 2, 94, 95, 133, 139, *Glossary:* Large Hadron Collider

LSP lightest supersymmetric particle. 31, 99, 100, 102, 103, 126, 127, 139, *Glossary:* lightest supersymmetric particle

pdf parton distribution function. 22, 139, *Glossary:* parton distribution function

RPC R-parity conserving. 33, 98, 139, *Glossary:* R-parity conserving

RPV R-parity violating. 31, 139, *Glossary:* R-parity violating

SUSY supersymmetry. 2, 25, 33, 94, 98–100, 139, *Glossary:* supersymmetry

List of Figures

List of Tables

A
Electroweak Symmetry Breaking

The Standard Model Lagrangian as presented in equation 2.1 on page 9 is not able to reproduce the results of experiments. Mass terms for the gauge and fermion fields are absent and the W^i and B fields do not have the correct properties to correspond to the $W^\pm$, Z and A fields observed in experiments. This can be resolved through spontaneous symmetry breaking.

A.1 The Higgs Mechanism

We introduce a new complex $\mathrm{SU}(2)_L \times \mathrm{U}(1)_Y$ scalar doublet

$$\Phi = \begin{pmatrix} \phi^+ \\ \phi^0 \end{pmatrix}$$

where the ϕ^+ and ϕ^0 are complex scalar fields with weak isospin I_3 of plus and minus $1/2$ respectively. The weak hypercharge of the doublet is $Y = 1$. We can then add this new field into the Lagrangian with an extra $\mathrm{SU}(3)_c \times \mathrm{SU}(2)_L \times \mathrm{U}(1)_Y$ invariant piece

$$\mathcal{L}_{\text{Higgs}} = (D^\mu \Phi)^\dagger (D_\mu \Phi) - V(\Phi), \qquad V(\Phi) = -\mu^2 \Phi^\dagger \Phi + \lambda (\Phi^\dagger \Phi)^2.$$

Note that the sign of μ^2 can be positive or negative by convention. Using the convention here $\mu^2 > 0$ corresponds to a negative mass squared $m_\Phi^2 = -\mu^2$. In this case it is clear that the minimum of the potential $V(\Phi)$ is not at $\Phi = 0$ but instead corresponds to the infinite degenerate set of states that satisfy

$$\Phi^\dagger \Phi = \frac{\mu^2}{2\lambda}. \tag{A.1}$$

The vacuum must select one of these states and it is clear that it then will no longer respect the $\mathrm{SU}(2)_L \times \mathrm{U}(1)_Y$ symmetry so we say that the symmetry is *spontaneously broken*.

Choosing the vacuum state to correspond to $\phi^0 = v = \sqrt{\frac{\mu^2}{2\lambda}}$, which is real-valued, we can rewrite the original Φ as excursions around this central point

$$\Phi = \frac{1}{\sqrt{2}} e^{i\frac{1}{2}\tau^i\theta^i(x)} \begin{pmatrix} 0 \\ v + h(x) \end{pmatrix}.$$

The four degrees of freedom in the original Φ field have been reinterpreted as 4 real fields: $\theta^{1,2,3}$ and h. The three θ fields correspond to excursions through the volume defined by equation A.1. By inspection we can see that were we to resubstitute these fields into $\mathcal{L}_{\mathrm{Higgs}}$ we would find that the θ fields no longer had a mass term - they have become massless 'Goldstone' bosons.

Rather than doing this we make a gauge transformation $\Phi \to e^{-i^1\!/_2\tau^i\theta^i(x)}\Phi$ and then substitute the remaining h field into $\mathcal{L}_{\mathrm{Higgs}}$.

$$\begin{aligned}\mathcal{L}_{\mathrm{Higgs}} =& \frac{1}{2}(\partial_\mu h)^2 + \frac{1}{8}g'^2(v+h)^2 B^\mu B_\mu + \frac{1}{8}g^2(v+h)^2(W^1_\mu W^{1\mu} + W^2_\mu W^{2\mu} + W^3_\mu W^{3\mu}) \\ &- \frac{1}{4}gg'(v+h)^2 W^3_\mu B^\mu + \mu^2(v+h)^2 - \lambda(v+h)^4. \end{aligned} \tag{A.2}$$

We note that the terms involving B_μ and W^3_μ look like they have been rotated from some other state by an angle given by $\tan\theta_W = {}^{g'}\!/_g$. We can therefore introduce two new fields that correspond to this rotation

$$\begin{pmatrix} Z_\mu \\ A_\mu \end{pmatrix} = \begin{pmatrix} \cos\theta_W & -\sin\theta_W \\ \sin\theta_W & \cos\theta_W \end{pmatrix} \begin{pmatrix} W^3_\mu \\ B_\mu \end{pmatrix}$$

where, as the notation suggests the Z_μ and A_μ fields correspond to the physical Z boson and the photon. We can also define the isospin raising and lowering fields

$W_\mu^\pm = \frac{1}{\sqrt{2}}(W_\mu^1 \pm iW_\mu^2)$ which correspond to the physical $W^\pm$ bosons. Rewriting equation A.2 using these physical fields we find

$$\begin{aligned}\mathcal{L}_{\text{Higgs}} =& \frac{1}{2}(\partial_\mu h)^2 + \frac{1}{4}g^2(v+h)^2 W_\mu^+ W^{-\mu} + \frac{1}{8\cos^2\theta_W} g^2 (v+h)^2 Z_\mu Z^\mu \\ &+ \frac{1}{4}\mu^2 v^2 - \mu^2 h^2 - \frac{\mu^2}{v} h^3 - \frac{\mu^2}{4v^2} h^4.\end{aligned}$$

So the Goldstone bosons have been absorbed by the physical $W^\pm$ and Z bosons to give them mass terms. The photon A_μ has remained massless, and indeed $\mathrm{U}(1)_{\mathrm{EM}}$ is still a symmetry of this Lagrangian. By mixing the W_μ^3 and B_μ fields we also find that the photon field A_μ appears in the gauge transformations of the $W_\mu^\pm$ fields, showing that they have acquired an electric charge[1]. These $W^\pm$ bosons are also each other's anti-particles as they carry opposite quantum numbers; the Z and photon however carry no conserved quantum numbers and so are their own antiparticles. We also predict a new physical scalar field h which has a mass $m_h = \sqrt{2}\mu$ and couples to each of the bosons proportional to their squared masses which we call the Higgs boson. We also predict masses $m_W = \frac{1}{2}vg$ and $m_Z = \frac{1}{2}v\frac{g}{\cos\theta_W}$.

By inserting the new A_μ and Z_μ fields into the covariant derivative (equation 2.2) we derive an expression for the unit electromagnetic charge

$$e = g'\cos\theta_W = g\sin\theta_W$$

and the charge for a particle

$$Q = \frac{1}{2}Y + I_3.$$

A.2 Fermion Masses and Quark Mixing

We can also use the same mechanism to introduce fermion masses by adding terms like

$$\mathcal{L}_{Y_\ell} = -\lambda_j^\ell(\bar{L}_j \Phi \ell_{Rj} + \Phi^\dagger \bar{\ell_R} L_j)$$

[1]This did not happen with the B_μ field

where the λ_{ℓ_j} are generation specific constants. After symmetry breaking this evaluates to

$$\mathcal{L}_{Y_\ell} = -\frac{\lambda_j^\ell}{\sqrt{2}}\bar{\ell}_j \ell_j (v + h)$$

which looks exactly like a fermion mass term with $m_{\ell_j} = \lambda_j^\ell v/\sqrt{2}$. This also predicts fermion couplings to the Higgs boson proportional to their masses.

The same can be done for the quarks. However in this case we must make two modifications. First we must allow for interactions with the $I_3 = 1/2$ up-type quarks. This is done by allowing terms involving the conjugate doublet $\tilde{\Psi} = i\tau^2\Psi^*$ which has $Y = -1$ and therefore correctly maintains gauge invariance[2]. Secondly, to match experimental results [17] we have to consider all three generations simultaneously. This yields a Lagrangian with terms like [147]

$$\mathcal{L}_{Y_q} = -\left(\lambda_{ij}^u \bar{u}_{R_i} \tilde{\Phi}^\dagger Q_j + \lambda_{ij}^d \bar{d}_{R_i} \Phi^\dagger Q_j + \text{h.c.}\right)$$

where h.c. indicates the hermitian conjugate of the previous expression. The upshot of this expression is that after electroweak symmetry breaking the Lagrangian will acquire quark masses. However, the 'mass' eigenstates that these masses correspond to can differ from the 'weak' eigenstates which we have consider this far.

[2]In order for a term to be gauge-invariant it must not have any net charge

B
Statistical tests used in the multijets analysis

The statistical analysis for the multijets analysis (chapter 5) is performed using the `HistFitter` [148] software package. Yields from the control regions are used to constrain the background predictions using a maximum likelihood estimation. The measured numbers of events in the signal regions are then also used to test the observed data against the Standard Model and our benchmark models. Each signal region is considered independently in concert with the control regions used to model the background contributions in that region. Each signal region is associated with three control regions, the $W+\text{jets}$ and $t\bar{t}$ control regions described in table 5.3 on page 108 and the multijet template region which has exactly the same selections as the signal region except for the $E_{\mathrm{T}}^{\mathrm{miss}}/\sqrt{H_{\mathrm{T}}}$ which is required to be less than 1.5 $\mathrm{GeV}^{1/2}$. For each controlled background a scaling factor μ is defined and allowed to vary.

B.1 Background only and model independent fits

The simplest fit performed is the background-only fit. The purpose of this fit is to determine the contribution of the measured backgrounds to the signal regions in a way that does not depend on the signal model being considered. It therefore calculates the significance of any deviations from the null hypothesis (in this case the Standard Model).

A likelihood is constructed from the predicted and measured number of events in each control region and maximised under the simultaneous variation of the three scaling factors μ_W, $\mu_{t\bar{t}}$ and μ_{multijet}. For each region the probability of measuring n events given a prediction of ν is given by a Poisson distribution,

$$\text{Pois}(n|\nu) = \frac{\nu^n e^{-\nu}}{n!}.$$

For perfectly measured events the likelihood would simply be the product of the Poisson distributions from the three control regions. However we have numerous uncertainties which must also be accounted for in the likelihood. For each source of uncertainty we consider we calculate the changes to the numbers of events passing our selections that are caused by a change relevant to the source of the uncertainty. Many of our uncertainties derive from measured parameters, such as the energy scale used in jet calibrations or the cross section for hadronic radiation in $t\bar{t}$ events. For these sources the parameter is varied by $\pm 1\sigma$ in order to derive the required change. Other cases have already been discussed, such as alternate $t\bar{t}$ generators and the template systematics.

These variations are then used to add additional factors in the likelihood calculation. These typically take the form of Gaussian constraints centred on the nominal value and with a width given by calculated variations. This way we introduce the sources of uncertainty as nuisance parameters in the fit. This allows the parameters to vary but penalises any large deviations from their nominal values. The fitting process determines the values of the μ scaling factors that maximise the likelihood and the uncertainties on those predictions (propagated from the input uncertainties).

In the absence of a significant excess it is possible to estimate the maximum number of signal events in a particular region which a model could predict and still be consistent with the observed data. This is useful as it allows the results to be reused to interpret new signal models; if any signal model predicts more than this number then it can be considered excluded by the analysis. The above fit is performed again now including the signal region. A signal model is injected into the fit which predicts 1 event in the signal region and 0 events in all control regions. An extra signal strength parameter μ_{sig} is included into the fit which then describes the normalisation of this model which best describes the data. As this parameter only affects the prediction in the signal region it does not affect the prediction from the background-only fit.

The parameter of interest is the signal strength parameter μ_{sig}. In what follows this is relabelled as μ and all other parameters, including the background normalisation factors and the nuisance parameters derived from the systematic uncertainties, are grouped into the vector θ. A test statistic called the profile log-likelihood ratio [149] is used which is derived from the profile likelihood

$$\lambda(\mu) = \frac{\mathcal{L}(\mu, \hat{\hat{\theta}}(\mu))}{\mathcal{L}(\hat{\mu}, \hat{\theta})}$$

where $\hat{\mu}$, $\hat{\theta}$ are the signal strength and the set of other parameter values which maximise the likelihood. $\hat{\hat{\theta}}(\mu)$ is the set of background parameter values which maximise the likelihood for a given signal strength and is therefore a function of μ. By construction this always falls between 0 and 1 and $\hat{\hat{\theta}}(\hat{\mu}) = \hat{\theta}$.

The profile log-likelihood ratio is defined as

$$q_\mu = \begin{cases} -2\ln\lambda(\mu) & \mu \geq \hat{\mu}; \\ 0 & s < \hat{\mu}. \end{cases}$$

We are looking for an upper limit on the signal strength μ that would be consistent with the data so we set the statistic to 0 when μ falls below the optimal value. We construct the pdf of the test statistic $f(q_\mu|\mu)$; this can either be approximated analytically when there are large numbers of observed events or using a MC technique to sample many pseudo-datasets from the constructed model PDF [150]. The probability for observing at least as many data events as were measured given a particular signal strength μ is then given by

$$p_{s+b} = \int_{q_\mu}^{\mathrm{inf}} f(q_\mu|\mu)$$

Values of μ are then scanned until p_{s+b} falls below 0.05, which signifies that a signal strength that high would be excluded at the 95% confidence level (CL_{s+b}). As the initial number of signal events used is 1 the value of μ at which this occurs corresponds to the number of events a signal model would have to predict in a particular signal region to be excluded at the 95% confidence level, written as $S^{95\%}_{\mathrm{obs}}$. This can also be interpreted as a limit on the cross-section $\langle\epsilon\sigma\rangle^{95\%}_{\mathrm{obs}} = S^{95\%}_{\mathrm{obs}}/\mathcal{L}_{\mathrm{int}}$ where ϵ is the efficiency of that signal region. The expected limit $\langle\epsilon\sigma\rangle^{95\%}_{\mathrm{exp}}$ can be calculated similarly by using the *predicted* numbers of events in the signal region rather than the measured number.

We can also consider the consistency of the data with the null hypothesis. For this the signal strength $\mu = 0$ and the test statistic is defined as

$$q_0 = \begin{cases} -2\ln\lambda(0) & \hat{\mu} \geq 0; \\ 0 & \hat{\mu} < 0. \end{cases}$$

The case $\hat{\mu} < 0$ corresponds to a measured deficit in the signal region. We set the statistic to 0 in this case as it is assumed that any potential signal would increase the event count in that region and while $\hat{\mu} < 0$ might represent evidence against the null hypothesis it is always stronger evidence against any such model. Similarly to before we define

$$p_0 = \int_{q_0}^{\mathrm{inf}} f(q_0|0).$$

We do not want to exclude signals based on a downward fluctuation in data. In such a situation it might be possible to reject the null hypothesis at the 95% CL and therefore any possible signal, even those to which the analysis should have no sensitivity! In order to protect against this ATLAS uses the conservative CL_s prescription [151] which defines the quantity

$$\mathrm{CL}_s = \frac{\mathrm{CL}_{s+b}}{\mathrm{CL}_b} = \frac{1-p_\mu}{1-p_0}.$$

This isn't a true confidence level but is always higher than CL_{s+b}. A signal strength μ is considered excluded if it has $\mathrm{CL}_s < 0.05$, providing an upper limit on μ.

B.2 Model dependent fit

In the event that no statistically significant excesses are observed the predictions from the benchmark signal models can be used to reject the hypotheses proposed by certain model points. In this case, the signal region is also included in the fit and the likelihood is constructed allowing the normalisation of the signal prediction μ_{sig} to float. By considering the contribution of the signal model to the control regions it is also possible to allow for signal contamination here, though this is typically small for the benchmark points considered in this analysis.

Again the same test statistics as above are defined and CL_s can be calculated for $\mu = 1$. A signal is considered excluded if its $\mathrm{CL}_s < 0.05$. When testing models with multiple parameters it is normal to calculate the CL_s for all points in the grid and then draw a contour at $\mathrm{CL}_s = 0.05$. The significance of an excess is defined to be

$$\mathrm{CL}_s = \int_Z^\infty \frac{e^{-1/2x^2}}{\sqrt{2\pi}} dx.$$

As with the model independent limit, the expected value of the CL_s can be calculated using the predicted number of events in the signal region as opposed to the measured data.

References

[1] Georges Aad et al. "Search for new phenomena in final states with large jet multiplicities and missing transverse momentum with ATLAS using $\sqrt{s} = 13$ TeV proton-proton collisions". In: *Phys. Lett.* B757 (2016), pp. 334–355. arXiv: 1602.06194 [hep-ex].

[2] Morad Aaboud et al. "Search for new phenomena with large jet multiplicities and missing transverse momentum using large-radius jets and flavour-tagging at ATLAS in 13 TeV *pp* collisions". In: *JHEP* 12 (2017), p. 034. arXiv: 1708.02794 [hep-ex].

[3] Morad Aaboud et al. "Performance of the ATLAS Trigger System in 2015". In: *Eur. Phys. J.* C77.5 (2017), p. 317. arXiv: 1611.09661 [hep-ex].

[4] I. J. R. Aitchison and A. J. G. Hey. *Gauge theories in particle physics: A practical introduction. Vol. 1: From relativistic quantum mechanics to QED*. Bristol, UK: CRC Press, 2012. URL: http://www-spires.fnal.gov/spires/find/books/www?cl=QC793.3.F5A34::2012.

[5] I. J. R. Aitchison and A. J. G. Hey. *Gauge theories in particle physics: A practical introduction. Vol. 2: Non-Abelian gauge theories: QCD and the electroweak theory*. Bristol, UK: CRC Press, 2012. URL: http://www-spires.fnal.gov/spires/find/books/www?cl=QC793.3.F5A34::2012:V2.

[6] Stephen P. Martin. "A Supersymmetry primer". In: (1997). [Adv. Ser. Direct. High Energy Phys.18,1(1998)], pp. 1–98. arXiv: hep-ph/9709356 [hep-ph].

[7] Sudhir K. Vempati. "Introduction to MSSM". In: (2012). arXiv: 1201.0334 [hep-ph].

[8] Richard Feynman. *Quantum mechanics and path integrals*. New York: McGraw-Hill, 1965.

[9] "The quantum theory of the emission and absorption of radiation". In: *Proceedings of the Royal Society of London A: Mathematical, Physical and Engineering Sciences* 114.767 (1927), pp. 243–265. eprint: http://rspa.royalsocietypublishing.org/content/114/767/243.full.pdf. URL: http://rspa.royalsocietypublishing.org/content/114/767/243.

[10] E. Noether. "Invariante Variationsprobleme". ger. In: *Nachrichten von der Gesellschaft der Wissenschaften zu Göttingen, Mathematisch-Physikalische Klasse* 1918 (1918), pp. 235–257. URL: http://eudml.org/doc/59024.

[11] E. Noether. "Invariant variation problems". In: *Transport Theory and Statistical Physics* 1 (Jan. 1971), pp. 186–207. eprint: physics/0503066.

[12] A. Pich. “The Standard model of electroweak interactions”. In: *2004 European School of High-Energy Physics, Sant Feliu de Guixols, Spain, 30 May - 12 June 2004*. 2005, pp. 1–48. arXiv: hep-ph/0502010 [hep-ph]. URL: http://doc.cern.ch/yellowrep/2006/2006-003/p1.pdf.

[13] J Collins. “Choosing the renormalization/factorization scale (QCD)”. In: *Journal of Physics G: Nuclear and Particle Physics* 17.10 (1991), p. 1547. URL: http://stacks.iop.org/0954-3899/17/i=10/a=009.

[14] Jorge C. Romao and Joao P. Silva. “A resource for signs and Feynman diagrams of the Standard Model”. In: *Int. J. Mod. Phys.* A27 (2012), p. 1230025. arXiv: 1209.6213 [hep-ph].

[15] M. Tabanashi et al. “Review of Particle Physics”. In: *Phys. Rev. D* 98 (2018), p. 030001.

[16] Ahmed Ali and Gustav Kramer. “Jets and QCD: A Historical Review of the Discovery of the Quark and Gluon Jets and its Impact on QCD”. In: *Eur. Phys. J.* H36 (2011), pp. 245–326. arXiv: 1012.2288 [hep-ph].

[17] Makoto Kobayashi and Toshihide Maskawa. “CP-Violation in the Renormalizable Theory of Weak Interaction”. In: *Progress of Theoretical Physics* 49.2 (1973), pp. 652–657. eprint: /oup/backfile/content_public/journal/ptp/49/2/10.1143/ptp.49.652/2/49-2-652.pdf. URL: http://dx.doi.org/10.1143/PTP.49.652.

[18] A. Quadt. “Top quark physics at hadron colliders”. In: *The European Physical Journal C - Particles and Fields* 48.3 (Dec. 2006), pp. 835–1000. URL: https://doi.org/10.1140/epjc/s2006-02631-6.

[19] T. J. Humanic. “Extracting the hadronization timescale in $\sqrt{s} = 7$ TeV proton-proton collisions from pion and kaon femtoscopy”. In: *J. Phys.* G41 (2014), p. 075105. arXiv: 1312.2303 [hep-ph].

[20] Bilas Pal. “Measurements of b hadron lifetimes and effective lifetimes at LHCb”. In: (2013). arXiv: 1309.5911 [hep-ex].

[21] Y. Fukuda et al. “Evidence for oscillation of atmospheric neutrinos”. In: *Phys. Rev. Lett.* 81 (1998), pp. 1562–1567. arXiv: hep-ex/9807003 [hep-ex].

[22] Claudio Giganti, Stéphane Lavignac, and Marco Zito. “Neutrino oscillations: the rise of the PMNS paradigm”. In: *Prog. Part. Nucl. Phys.* 98 (2018), pp. 1–54. arXiv: 1710.00715 [hep-ex].

[23] André de Gouvêa. “Neutrino Mass Models”. In: *Annual Review of Nuclear and Particle Science* 66.1 (2016), pp. 197–217. eprint: https://doi.org/10.1146/annurev-nucl-102115-044600. URL: https://doi.org/10.1146/annurev-nucl-102115-044600.

[24] Ivan Esteban et al. “Updated fit to three neutrino mixing: exploring the accelerator-reactor complementarity”. In: *JHEP* 01 (2017), p. 087. arXiv: 1611.01514 [hep-ph].

[25] Robin Devenish and Amanda Cooper-Sarkar. *Deep inelastic scattering*. Oxford University Press, 2011.

[26] Hung-Liang Lai et al. “New parton distributions for collider physics”. In: *Phys. Rev.* D82 (2010), p. 074024. arXiv: 1007.2241 [hep-ph].

[27] F. D. Aaron et al. "Combined Measurement and QCD Analysis of the Inclusive e+- p Scattering Cross Sections at HERA". In: *JHEP* 01 (2010), p. 109. arXiv: `0911.0884 [hep-ex]`.

[28] D. Acosta et al. "Measurement of the forward-backward charge asymmetry from $W \to e\nu$ production in $p\bar{p}$ collisions at $\sqrt{s} = 1.96$ TeV". In: *Phys. Rev.* D71 (2005), p. 051104. arXiv: `hep-ex/0501023 [hep-ex]`.

[29] Georges Aad et al. "Measurement of the production of a W boson in association with a charm quark in pp collisions at $\sqrt{s} = 7$ TeV with the ATLAS detector". In: *JHEP* 05 (2014), p. 068. arXiv: `1402.6263 [hep-ex]`.

[30] Georges Aad et al. "Measurement of the low-mass Drell-Yan differential cross section at $\sqrt{s} = 7$ TeV using the ATLAS detector". In: *JHEP* 06 (2014), p. 112. arXiv: `1404.1212 [hep-ex]`.

[31] S. Fukuda et al. "The Super-Kamiokande detector". In: *Nuclear Instruments and Methods in Physics Research Section A: Accelerators, Spectrometers, Detectors and Associated Equipment* 501.2 (2003), pp. 418–462. URL: `http://www.sciencedirect.com/science/article/pii/S016890020300425X`.

[32] Rafael C. Lopes de Sa. "Precise measurements of the W mass at the Tevatron and indirect constraints on the Higgs mass". In: *Proceedings, 47th Rencontres de Moriond on QCD and High Energy Interactions: La Thuile, France, March 10-17, 2012*. 2012, pp. 3–10. arXiv: `1204.3260 [hep-ex]`. URL: `http://lss.fnal.gov/cgi-bin/find_paper.pl?conf-12-103`.

[33] A. Bosma. "The distribution and kinematics of neutral hydrogen in spiral galaxies of various morphological types". PhD thesis. PhD Thesis, Groningen Univ., (1978), 1978.

[34] Richard Massey, Thomas Kitching, and Johan Richard. "The dark matter of gravitational lensing". In: *Rept. Prog. Phys.* 73 (2010), p. 086901. arXiv: `1001.1739 [astro-ph.CO]`.

[35] Debaprasad Maity and Pankaj Saha. "Connecting CMB anisotropy and cold dark matter phenomenology via reheating". In: (2018). arXiv: `1801.03059 [hep-ph]`.

[36] Farinaldo S. Queiroz. "WIMP Theory Review". In: *PoS* EPS-HEP2017 (2017), p. 080. arXiv: `1711.02463 [hep-ph]`.

[37] P. J. E. Peebles and Bharat Ratra. "The Cosmological constant and dark energy". In: *Rev. Mod. Phys.* 75 (2003). [,592(2002)], pp. 559–606. arXiv: `astro-ph/0207347 [astro-ph]`.

[38] Q. R. Ahmad et al. "Measurement of the rate of $\nu_e + d \to p + p + e^-$ interactions produced by ^8B solar neutrinos at the Sudbury Neutrino Observatory". In: *Phys. Rev. Lett.* 87 (2001), p. 071301. arXiv: `nucl-ex/0106015 [nucl-ex]`.

[39] Stefano Dell'Oro et al. "Neutrinoless double beta decay: 2015 review". In: *Adv. High Energy Phys.* 2016 (2016), p. 2162659. arXiv: `1601.07512 [hep-ph]`.

[40] Andrei D Sakharov. "Violation of CP invariance, C asymmetry, and baryon asymmetry of the universe". In: *Soviet Physics Uspekhi* 34.5 (1991), p. 392. URL: `http://stacks.iop.org/0038-5670/34/i=5/a=A08`.

[41] R. D. Peccei. "The Strong CP problem and axions". In: *Lect. Notes Phys.* 741 (2008). [,3(2006)], pp. 3–17. arXiv: `hep-ph/0607268 [hep-ph]`.

[42] Howard Georgi and S. L. Glashow. "Unity of All Elementary-Particle Forces". In: *Phys. Rev. Lett.* 32 (8 Feb. 1974), pp. 438–441. URL: https://link.aps.org/doi/10.1103/PhysRevLett.32.438.

[43] Yu. A. Golfand and E. P. Likhtman. "Extension of the Algebra of Poincare Group Generators and Violation of p Invariance". In: *JETP Lett.* 13 (1971). [Pisma Zh. Eksp. Teor. Fiz. **13** (1971) 452], p. 323.

[44] D. V. Volkov and V. P. Akulov. "Is the Neutrino a Goldstone Particle?" In: *Phys. Lett. B* 46 (1973), p. 109.

[45] J. Wess and B. Zumino. "Supergauge Transformations in Four-Dimensions". In: *Nucl. Phys. B* 70 (1974), p. 39.

[46] J. Wess and B. Zumino. "Supergauge Invariant Extension of Quantum Electrodynamics". In: *Nucl. Phys. B* 78 (1974), p. 1.

[47] S. Ferrara and B. Zumino. "Supergauge Invariant Yang-Mills Theories". In: *Nucl. Phys. B* 79 (1974), p. 413.

[48] Abdus Salam and J. A. Strathdee. "Supersymmetry and Nonabelian Gauges". In: *Phys. Lett. B* 51 (1974), p. 353.

[49] G.'t Hooft. "Naturalness, Chiral Symmetry, and Spontaneous Chiral Symmetry Breaking". In: *Recent Developments in Gauge Theories.* Ed. by G.'t Hooft et al. Boston, MA: Springer US, 1980, pp. 135–157. URL: https://doi.org/10.1007/978-1-4684-7571-5_9.

[50] Sidney Coleman and Jeffrey Mandula. "All Possible Symmetries of the S Matrix". In: *Phys. Rev.* 159 (5 July 1967), pp. 1251–1256. URL: https://link.aps.org/doi/10.1103/PhysRev.159.1251.

[51] Rudolf Haag, Jan T. Łopuszański, and Martin Sohnius. "All possible generators of supersymmetries of the S-matrix". In: *Nuclear Physics B* 88.2 (1975), pp. 257–274. URL: http://www.sciencedirect.com/science/article/pii/0550321375902795.

[52] Fernando Quevedo, Sven Krippendorf, and Oliver Schlotterer. "Cambridge Lectures on Supersymmetry and Extra Dimensions". In: (2010). arXiv: 1011.1491 [hep-th].

[53] Kfir Blum et al. "Combining K^0–$\overline{K}^0$ Mixing and D^0–$\overline{D}^0$ Mixing to Constrain the Flavor Structure of New Physics". In: *Phys. Rev. Lett.* 102 (21 May 2009), p. 211802. URL: https://link.aps.org/doi/10.1103/PhysRevLett.102.211802.

[54] S. Dimopoulos, S. Raby, and Frank Wilczek. "Supersymmetry and the scale of unification". In: *Phys. Rev. D* 24 (6 Sept. 1981), pp. 1681–1683. URL: https://link.aps.org/doi/10.1103/PhysRevD.24.1681.

[55] N. Sakai. "Naturalness in Supersymmetric Guts". In: *Z. Phys. C* 11 (1981), p. 153.

[56] S. Dimopoulos, S. Raby, and Frank Wilczek. "Supersymmetry and the Scale of Unification". In: *Phys. Rev. D* 24 (1981), p. 1681.

[57] Luis E. Ibanez and Graham G. Ross. "Low-Energy Predictions in Supersymmetric Grand Unified Theories". In: *Phys. Lett. B* 105 (1981), p. 439.

[58] Savas Dimopoulos and Howard Georgi. "Softly Broken Supersymmetry and SU(5)". In: *Nucl. Phys. B* 193 (1981), p. 150.

[59] Michael Dine and Willy Fischler. "A Phenomenological Model of Particle Physics Based on Supersymmetry". In: *Phys. Lett. B* 110 (1982), p. 227.

[60] Luis Alvarez-Gaume, Mark Claudson, and Mark B. Wise. "Low-Energy Supersymmetry". In: *Nucl. Phys. B* 207 (1982), p. 96.

[61] Chiara R. Nappi and Burt A. Ovrut. "Supersymmetric Extension of the SU(3) x SU(2) x U(1) Model". In: *Phys. Lett. B* 113 (1982), p. 175.

[62] Gian F. Giudice et al. "Gaugino mass without singlets". In: *JHEP* 12 (1998), p. 027. arXiv: `hep-ph/9810442`.

[63] Lisa Randall and Raman Sundrum. "Out of this world supersymmetry breaking". In: *Nucl. Phys. B* 557 (1999), p. 79. arXiv: `hep-th/9810155`.

[64] L. Girardello and Marcus T. Grisaru. "Soft Breaking of Supersymmetry". In: *Nucl. Phys. B* 194 (1982), p. 65.

[65] H. Nishino et al. "Search for Proton Decay via p —> e+ pi0 and p —> mu+ pi0 in a Large Water Cherenkov Detector". In: *Phys. Rev. Lett.* 102 (2009), p. 141801. arXiv: `0903.0676 [hep-ex]`.

[66] Glennys R. Farrar and Pierre Fayet. "Phenomenology of the Production, Decay, and Detection of New Hadronic States Associated with Supersymmetry". In: *Phys. Lett. B* 76 (1978), p. 575.

[67] Stephen P. Martin. "Some simple criteria for gauged R-parity". In: *Phys. Rev.* D46 (1992), R2769–R2772. arXiv: `hep-ph/9207218 [hep-ph]`.

[68] Charanjit S. Aulakh et al. "The Minimal supersymmetric grand unified theory". In: *Phys. Lett.* B588 (2004), pp. 196–202. arXiv: `hep-ph/0306242 [hep-ph]`.

[69] H. Goldberg. "Constraint on the Photino Mass from Cosmology". In: *Phys. Rev. Lett.* 50 (1983). Erratum: Phys. Rev. Lett. **103** (2009) 099905, p. 1419.

[70] John R. Ellis et al. "Supersymmetric Relics from the Big Bang". In: *Nucl. Phys. B* 238 (1984), p. 453.

[71] Toby Falk, Keith A. Olive, and Mark Srednicki. "Heavy sneutrinos as dark matter". In: *Phys. Lett.* B339 (1994), pp. 248–251. arXiv: `hep-ph/9409270 [hep-ph]`.

[72] Pierre Fayet. "Supersymmetry and Weak, Electromagnetic and Strong Interactions". In: *Phys. Lett. B* 64 (1976), p. 159.

[73] Pierre Fayet. "Spontaneously Broken Supersymmetric Theories of Weak, Electromagnetic and Strong Interactions". In: *Phys. Lett. B* 69 (1977), p. 489.

[74] Ali H. Chamseddine, Richard L. Arnowitt, and Pran Nath. "Locally Supersymmetric Grand Unification". In: *Phys. Rev. Lett.* 49 (1982), p. 970.

[75] Riccardo Barbieri, S. Ferrara, and Carlos A. Savoy. "Gauge Models with Spontaneously Broken Local Supersymmetry". In: *Phys. Lett. B* 119 (1982), p. 343.

[76] Gordon L. Kane et al. "Study of constrained minimal supersymmetry". In: *Phys. Rev. D* 49 (1994), p. 6173. arXiv: `hep-ph/9312272`.

[77] Carola F. Berger et al. "Supersymmetry Without Prejudice". In: *JHEP* 02 (2009), p. 023. arXiv: 0812.0980 [hep-ph].

[78] A. Djouadi et al. *The Minimal supersymmetric standard model: Group summary report.* 1998. arXiv: hep-ph/9901246.

[79] Georges Aad et al. "Summary of the ATLAS experiment's sensitivity to supersymmetry after LHC Run 1 — interpreted in the phenomenological MSSM". In: *JHEP* 10 (2015), p. 134. arXiv: 1508.06608 [hep-ex].

[80] Johan Alwall et al. "Searching for Directly Decaying Gluinos at the Tevatron". In: *Phys. Lett. B* 666 (2008), p. 34. arXiv: 0803.0019 [hep-ph].

[81] Johan Alwall, Philip Schuster, and Natalia Toro. "Simplified Models for a First Characterization of New Physics at the LHC". In: *Phys. Rev. D* 79 (2009), p. 075020. arXiv: 0810.3921 [hep-ph].

[82] Daniele Alves et al. "Simplified Models for LHC New Physics Searches". In: *J. Phys. G* 39 (2012), p. 105005. arXiv: 1105.2838 [hep-ph].

[83] Riccardo Barbieri and G. F. Giudice. "Upper Bounds on Supersymmetric Particle Masses". In: *Nucl. Phys. B* 306 (1988), p. 63.

[84] B. de Carlos and J. A. Casas. "One loop analysis of the electroweak breaking in supersymmetric models and the fine tuning problem". In: *Phys. Lett. B* 309 (1993), p. 320. arXiv: hep-ph/9303291.

[85] William James Fawcett and Alan Barr. "Supersymmetry searches at the LHC and their interpretations". Presented 29 Sep 2017. Feb. 2018. URL: http://cds.cern.ch/record/2305551.

[86] Christoph Borschensky et al. "Squark and gluino production cross sections in pp collisions at $\sqrt{s} = 13$, 14, 33 and 100 TeV". In: *Eur. Phys. J.* C74.12 (2014), p. 3174. arXiv: 1407.5066 [hep-ph].

[87] G. Aad et al. "The ATLAS Experiment at the CERN Large Hadron Collider". In: *JINST* 3 (2008), S08003.

[88] Lyndon Evans and Philip Bryant. "LHC Machine". In: *JINST* 3 (2008), S08001.

[89] K. Aamodt et al. "The ALICE experiment at the CERN LHC". In: *JINST* 3 (2008), S08002.

[90] S. Chatrchyan et al. "The CMS Experiment at the CERN LHC". In: *JINST* 3 (2008), S08004.

[91] A. Augusto Alves Jr. et al. "The LHCb Detector at the LHC". In: *JINST* 3 (2008), S08005.

[92] Lyndon Evans. "The Large Hadron Collider". In: *Philosophical Transactions of the Royal Society of London A: Mathematical, Physical and Engineering Sciences* 370.1961 (2012), pp. 831–858. eprint: http://rsta.royalsocietypublishing.org/content/370/1961/831.full.pdf. URL: http://rsta.royalsocietypublishing.org/content/370/1961/831.

[93] Morad Aaboud et al. "Luminosity determination in pp collisions at $\sqrt{s} = 8$ TeV using the ATLAS detector at the LHC". In: *Eur. Phys. J.* C76.12 (2016), p. 653. arXiv: 1608.03953 [hep-ex].

[94] "W.J. Stirling, private communication". In: ().

[95] M. Tylmad. "Pulse shapes for signal reconstruction in the ATLAS Tile Calorimeter". In: *2009 16th IEEE-NPSS Real Time Conference.* May 2009, pp. 543–547.

[96] G. Aad et al. "The ATLAS Inner Detector commissioning and calibration". In: *Eur. Phys. J.* C70 (2010), pp. 787–821. arXiv: `1004.5293 [physics.ins-det]`.

[97] N Ilic. "Performance of the ATLAS Liquid Argon Calorimeter after three years of LHC operation and plans for a future upgrade". In: *Journal of Instrumentation* 9.03 (2014), p. C03049. URL: `http://stacks.iop.org/1748-0221/9/i=03/a=C03049`.

[98] E. Diehl. "Calibration and Performance of the ATLAS Muon Spectrometer". In: *Particles and fields. Proceedings, Meeting of the Division of the American Physical Society, DPF 2011, Providence, USA, August 9-13, 2011.* 2011. arXiv: `1109.6933 [physics.ins-det]`.

[99] Karolos Potamianos. "The upgraded Pixel detector and the commissioning of the Inner Detector tracking of the ATLAS experiment for Run-2 at the Large Hadron Collider". In: *PoS* EPS-HEP2015 (2015), p. 261. arXiv: `1608.07850 [physics.ins-det]`.

[100] Yosuke Takubo. "ATLAS IBL operational experience". In: *PoS* Vertex2016 (2017), p. 004.

[101] C. Patrignani et al. "Review of Particle Physics". In: *Chin. Phys.* C40.10 (2016), p. 100001.

[102] Bernard Aubert et al. "Performance of the ATLAS electromagnetic calorimeter end-cap module 0". In: *Nucl. Instrum. Meth.* A500 (2003), pp. 178–201.

[103] C. Rubbia. "Measurement of the Luminosity of p anti-p Collider with a (Generalized) Van Der Meer Method". In: (1977).

[104] R. Achenbach et al. "The ATLAS level-1 calorimeter trigger". In: *JINST* 3 (2008), P03001.

[105] W. Lampl et al. "Calorimeter clustering algorithms: Description and performance". In: (2008).

[106] Georges Aad et al. "Topological cell clustering in the ATLAS calorimeters and its performance in LHC Run 1". In: *Eur. Phys. J.* C77 (2017), p. 490. arXiv: `1603.02934 [hep-ex]`.

[107] *Vertex Reconstruction Performance of the ATLAS Detector at* $\sqrt{s} = 13$ TeV. Tech. rep. ATL-PHYS-PUB-2015-026. Geneva: CERN, July 2015. URL: `http://cds.cern.ch/record/2037717`.

[108] Matteo Cacciari, Gavin P. Salam, and Gregory Soyez. "The Anti-k(t) jet clustering algorithm". In: *JHEP* 04 (2008), p. 063. arXiv: `0802.1189 [hep-ph]`.

[109] *Tagging and suppression of pileup jets with the ATLAS detector.* Tech. rep. ATLAS-CONF-2014-018. Geneva: CERN, May 2014. URL: `https://cds.cern.ch/record/1700870`.

[110] Matteo Cacciari, Gavin P. Salam, and Gregory Soyez. "The Catchment Area of Jets". In: *JHEP* 04 (2008), p. 005. arXiv: `0802.1188 [hep-ph]`.

[111] *Optimisation of the ATLAS b-tagging performance for the 2016 LHC Run.* Tech. rep. ATL-PHYS-PUB-2016-012. Geneva: CERN, June 2016. URL: http://cds.cern.ch/record/2160731.

[112] *Electron efficiency measurements with the ATLAS detector using the 2015 LHC proton-proton collision data.* Tech. rep. ATLAS-CONF-2016-024. Geneva: CERN, June 2016. URL: https://cds.cern.ch/record/2157687.

[113] Morad Aaboud et al. "Measurement of the photon identification efficiencies with the ATLAS detector using LHC Run-1 data". In: *Eur. Phys. J.* C76.12 (2016), p. 666. arXiv: 1606.01813 [hep-ex].

[114] Georges Aad et al. "Muon reconstruction performance of the ATLAS detector in proton–proton collision data at $\sqrt{s}$ =13 TeV". In: *Eur. Phys. J.* C76.5 (2016), p. 292. arXiv: 1603.05598 [hep-ex].

[115] Jean-Baptiste De Vivie De Regie et al. *ATLAS electron, photon and muon isolation in Run 2.* Tech. rep. ATL-COM-PHYS-2017-290. This note contains the Moriond 2017 recommendations. It will be updated when new recommendations become available. Geneva: CERN, Mar. 2017. URL: https://cds.cern.ch/record/2256658.

[116] *Expected performance of missing transverse momentum reconstruction for the ATLAS detector at $\sqrt{s} = 13$ TeV.* Tech. rep. ATL-PHYS-PUB-2015-023. Geneva: CERN, July 2015. URL: http://cds.cern.ch/record/2037700.

[117] N. V. Mokhov D. E. Groom and S. I. Striganov. "Muon stopping power and range tables 10-MeV to 100-TeV". In: *Atom. Data Nucl. Data Tabl* 78 (2001), pp. 183–356.

[118] The ATLAS collaboration. "Analytical description of missing transverse-momentum trigger rates in ATLAS with 7 and 8 TeV data". In: (). URL: http://cds.cern.ch/record/2292378.

[119] *Trigger monitoring and rate predictions using Enhanced Bias data from the ATLAS Detector at the LHC.* Tech. rep. ATL-DAQ-PUB-2016-002. Geneva: CERN, Oct. 2016. URL: https://cds.cern.ch/record/2223498.

[120] M. Aaboud et al. "Jet energy scale measurements and their systematic uncertainties in proton-proton collisions at $\sqrt{s} = 13$ TeV with the ATLAS detector". In: *Phys. Rev.* D96.7 (2017), p. 072002. arXiv: 1703.09665 [hep-ex].

[121] Georges Aad et al. "Search for invisible decays of a Higgs boson using vector-boson fusion in *pp* collisions at $\sqrt{s} = 8$ TeV with the ATLAS detector". In: *JHEP* 01 (2016), p. 172. arXiv: 1508.07869 [hep-ex].

[122] *The ATLAS transverse-momentum trigger performance at the LHC in 2011.* Tech. rep. ATLAS-CONF-2014-002. Geneva: CERN, Feb. 2014. URL: https://cds.cern.ch/record/1647616.

[123] Morad Aaboud et al. "Search for supersymmetry in final states with missing transverse momentum and multiple *b*-jets in proton-proton collisions at $\sqrt{s} = 13$ TeV with the ATLAS detector". In: *JHEP* 06 (2018), p. 107. arXiv: 1711.01901 [hep-ex].

[124] Morad Aaboud et al. "Search for top-squark pair production in final states with one lepton, jets, and missing transverse momentum using 36 fb^{-1} of $\sqrt{s} = 13$ TeV pp collision data with the ATLAS detector". In: *JHEP* 06 (2018), p. 108. arXiv: `1711.11520 [hep-ex]`.

[125] Morad Aaboud et al. "Search for electroweak production of supersymmetric states in scenarios with compressed mass spectra at $\sqrt{s} = 13$ TeV with the ATLAS detector". In: *Phys. Rev.* D97.5 (2018), p. 052010. arXiv: `1712.08119 [hep-ex]`.

[126] Morad Aaboud et al. "Search for pair production of up-type vector-like quarks and for four-top-quark events in final states with multiple b-jets with the ATLAS detector". In: *JHEP* 07 (2018), p. 089. arXiv: `1803.09678 [hep-ex]`.

[127] Morad Aaboud et al. "Search for High-Mass Resonances Decaying to $\tau\nu$ in pp Collisions at $\sqrt{s} = 13$ TeV with the ATLAS Detector". In: *Phys. Rev. Lett.* 120.16 (2018), p. 161802. arXiv: `1801.06992 [hep-ex]`.

[128] Morad Aaboud et al. "Search for dark matter and other new phenomena in events with an energetic jet and large missing transverse momentum using the ATLAS detector". In: *JHEP* 01 (2018), p. 126. arXiv: `1711.03301 [hep-ex]`.

[129] M. Aaboud et al. "Evidence for the $H \to b\bar{b}$ decay with the ATLAS detector". In: *JHEP* 12 (2017), p. 024. arXiv: `1708.03299 [hep-ex]`.

[130] Alan Barr and Jesse Liu. "Analysing parameter space correlations of recent 13 TeV gluino and squark searches in the pMSSM". In: *Eur. Phys. J.* C77.3 (2017), p. 202. arXiv: `1608.05379 [hep-ph]`.

[131] Andy Buckley. "PySLHA: a Pythonic interface to SUSY Les Houches Accord data". In: (). arXiv: `1305.4194 [hep-ph]`.

[132] Ulrich Langenfeld, Sven-Olaf Moch, and Torsten Pfoh. "QCD threshold corrections for gluino pair production at hadron colliders". In: *JHEP* 11 (2012), p. 070. arXiv: `1208.4281 [hep-ph]`.

[133] Georges Aad et al. "Jet energy resolution in proton-proton collisions at $\sqrt{s} = 7$ TeV recorded in 2010 with the ATLAS detector". In: *Eur. Phys. J.* C73.3 (2013), p. 2306. arXiv: `1210.6210 [hep-ex]`.

[134] Torbjorn Sjostrand, Stephen Mrenna, and Peter Z. Skands. "A Brief Introduction to PYTHIA 8.1". In: *Comput. Phys. Commun.* 178 (2008), pp. 852–867. arXiv: `0710.3820 [hep-ph]`.

[135] G. Aad et al. "The ATLAS Simulation Infrastructure". In: *Eur. Phys. J.* C70 (2010), pp. 823–874. arXiv: `1005.4568 [physics.ins-det]`.

[136] S. Agostinelli et al. GEANT4 Collaboration. "Geant4—a simulation toolkit". In: *Nuclear Instruments and Methods in Physics Research Section A: Accelerators, Spectrometers, Detectors and Associated Equipment* 506.3 (2003), pp. 250–303. URL: `http://www.sciencedirect.com/science/article/pii/S0168900203013688`.

[137] M. Bahr et al. "Herwig++ Physics and Manual". In: *Eur. Phys. J.* C58 (2008), pp. 639–707. arXiv: `0803.0883 [hep-ph]`.

[138] Simone Alioli et al. "A general framework for implementing NLO calculations in shower Monte Carlo programs: the POWHEG BOX". In: *JHEP* 06 (2010), p. 043. arXiv: `1002.2581 [hep-ph]`.

[139] Torbjorn Sjostrand, Stephen Mrenna, and Peter Z. Skands. "PYTHIA 6.4 Physics and Manual". In: *JHEP* 05 (2006), p. 026. arXiv: hep-ph/0603175 [hep-ph].

[140] T. Gleisberg et al. "Event generation with SHERPA 1.1". In: *JHEP* 02 (2009), p. 007. arXiv: 0811.4622 [hep-ph].

[141] J. Alwall et al. "The automated computation of tree-level and next-to-leading order differential cross sections, and their matching to parton shower simulations". In: *JHEP* 07 (2014), p. 079. arXiv: 1405.0301 [hep-ph].

[142] *Simulation of top quark production for the ATLAS experiment at sqrt(s) = 13 TeV*. Tech. rep. ATL-PHYS-PUB-2016-004. Geneva: CERN, Jan. 2016. URL: https://cds.cern.ch/record/2120417.

[143] *Modelling of the $t\bar{t}H$ and $t\bar{t}V$ $(V = W, Z)$ processes for $\sqrt{s} = 13$ TeV ATLAS analyses*. Tech. rep. ATL-PHYS-PUB-2016-005. Geneva: CERN, Jan. 2016. URL: https://cds.cern.ch/record/2120826.

[144] *Monte Carlo Generators for the Production of a W or Z/γ^* Boson in Association with Jets at ATLAS in Run 2*. Tech. rep. ATL-PHYS-PUB-2016-003. Geneva: CERN, Jan. 2016. URL: https://cds.cern.ch/record/2120133.

[145] *Multi-Boson Simulation for 13 TeV ATLAS Analyses*. Tech. rep. ATL-PHYS-PUB-2016-002. Geneva: CERN, Jan. 2016. URL: https://cds.cern.ch/record/2119986.

[146] ATLAS Collaboration. *Jet uncertainties twiki*. https://twiki.cern.ch/twiki/bin/view/AtlasProtected/JetUncertainties2015ICHEP2016.

[147] Heather E. Logan. "TASI 2013 lectures on Higgs physics within and beyond the Standard Model". In: (2014). arXiv: 1406.1786 [hep-ph].

[148] M. Baak et al. "HistFitter software framework for statistical data analysis". In: *Eur. Phys. J.* C75 (2015), p. 153. arXiv: 1410.1280 [hep-ex].

[149] Eilam Gross. "LHC Statistics for Pedestrians". In: (2008). URL: https://cds.cern.ch/record/1099994.

[150] Glen Cowan et al. "Asymptotic formulae for likelihood-based tests of new physics". In: *Eur. Phys. J.* C71 (2011). [Erratum: Eur. Phys. J.C73,2501(2013)], p. 1554. arXiv: 1007.1727 [physics.data-an].

[151] A L Read. "Presentation of search results: the CL s technique". In: *Journal of Physics G: Nuclear and Particle Physics* 28.10 (2002), p. 2693. URL: http://stacks.iop.org/0954-3899/28/i=10/a=313.